Dynamics of Tapered and Spherical Roller Bearings: Modelling and Analysis

Marisa Antunes de Lima

Thesis to obtain the Master of Science Degree in

Mechanical Engineering

Supervisor: Prof. Jorge Alberto Cadete Ambrósio

Examination Committee

Chairperson: Prof. Luís Manuel Varejão de Oliveira Faria
Supervisor: Prof. Jorge Alberto Cadete Ambrósio
Member of the Committee: Prof. João Paulo Flores Fernandes

November 2015

ACKNOWLEDGMENTS

To my supervisor, Prof. Jorge Ambrósio, I would like to express my profound gratitude for all the guidance and teaching that he provided throughout this work. His knowledge and enthusiasm were extremely motivating at all times and have inspired me to become a better professional.

To my colleagues, my special thanks for all the help provided when doubts emerged. Namely to Pedro Antunes for his tireless support in most computational aspects and to Hugo Magalhães for his vigorous help with visualization tools.

My special thanks to the team of tribology of the Faculty of Engineering of University of Porto, for all the help in providing the needed measurements of bearings, as well as in clarifying all our doubts related to tribology. My gratitude goes especially to Prof. Jorge Seabra, Prof. Ramiro Martins and André Gama, for the kindness and availability expressed at all times.

To my friends, for always making things look easy and for creating discussions that help ideas emerge, my kind thank you. Lastly, I want to express my gratitude to my family, for their care and encouragement at all times. Their trust in knowing one can always be better has inspired me since the beginning.

ABSTRACT

The dynamic performance of the roller bearings used in railway vehicles is the fundamental objective of project MAXBE, which motivates the work presented here. The monitoring of the bearings performance via monitoring systems uses the vibration information to infer the health of their mechanical components. The vibration output of the axleboxes is a measurable outcome of the bearing dynamic response, under operating conditions, that is characterized in this work. The main goal of this work is to develop a dynamic analysis tool, referred to as `BearDyn`, in MATLAB®, able to handle models representative of actual railway axle bearings, by using a multibody formulation to describe the mechanical elements of the bearing and their interactions. Realistic bearing geometric data is obtained by precise measurements of spherical and tapered bearings, with the support of FEUP. The interactions between the elements are described by continuous contact force models based on the Hertz elastic contact theory and modified according to experimental evidence. Tribological lubrication models are applied to describe the tangential forces in the presence of lubricant. Finally, `BearDyn` is tested for realistic railway conditions, where the inner raceway has an initial angular velocity and load applied to its center, while the outer raceway is fixed. In different conditions, the bearing dynamic response is obtained in terms of forces, kinematic quantities and different interaction measures, in the time domain as well as Fast Fourier Transforms in the frequency domain, which can be ultimately used for direct correlation with the outcome of the monitoring stations.

Keywords

Axlebox

Roller bearing

Multibody dynamics

Railway dynamics

Hertz Contact

Elastohydrodynamic lubrication

RESUMO

A resposta dinâmica de rolamentos usados em veículos ferroviários é o objetivo principal do projeto MAXBE, que motiva o trabalho aqui apresentado. A monitorização de rolamentos via sistemas adequados usam a informação em termos de vibração para avaliar a condição dos seus componentes mecânicos. O objetivo principal deste trabalho é desenvolver uma ferramenta de análise dinâmica, referida como `BearDyn`, em MATLAB®, capaz de avaliar modelos representativos de rolamentos usados em aplicações ferroviárias, através de uma formulação multi-corpo para descrever os elementos mecânicos do rolamento e as suas interações. Dados geométricos realísticos de rolamentos são obtidos através de medições precisas de rolamentos de rolos esféricos e cónicos, com o suporte da FEUP. As interações entre rolos, gaiola e caminhos são descritas por modelos de força de contacto baseadas na teoria de contacto elástico de Hertz e modificados de acordo com evidências experimentais. Modelos tribológicos de lubrificação são aplicados para descrever as forças tangenciais na presença de lubrificante. Finalmente, `BearDyn` é testado para condições ferroviárias realísticas, em quais o caminho interior é providenciado com uma velocidade angular inicial e uma carga elevada é aplicada no seu centro, enquanto o caminho exterior é fixo. Em diferentes condições, a resposta dinâmica do rolamento é obtida em termos de forças, quantidades cinemáticas e diferentes medidas de interações, tanto no domínio do tempo como no domínio da frequência, através de Transformadas de Fourier, que podem ser utilizadas posteriormente para correlações diretas com os resultados de estações de monitorização.

Palavras-chave

Caixa de eixo

Rolamento

Dinâmica multi-corpo

Dinâmica ferroviária

Contacto Hertziano

Lubrificação elastohidrodinâmica

TABLE OF CONTENTS

x

LIST OF FIGURES

LIST OF TABLES

LIST OF SYMBOLS

Convention

a, A, α	Scalar
a	Vector
A	Matrix

Overscores

$\dot{\mathbf{a}}$	First time derivative
$\ddot{\mathbf{a}}$	Second time derivative
$\tilde{\mathbf{a}}$	Skew-symmetric matrix

Superscripts

$\mathbf{a}^0$	Initial condition
$\mathbf{a}^T$	Matrix or vector transpose
$\mathbf{a}^{-1}$	Inverse
$\mathbf{a}'$	Vector expressed in the body-fixed reference frame
$\mathbf{a}^*$	Vector expressed in the $(\xi\eta)$ plane; Vector in the Euler parameter space

Subscripts

$\mathbf{a}_i$	Refers to rigid body i in a system
$\mathbf{a}_j$	Refers to rigid body j in a system
$\mathbf{a}_b$	Refers to the roller in a roller bearing system
$\mathbf{a}_c, \mathbf{a}_{cage}$	Refers to the cage in a roller bearing system
$\mathbf{a}_{inner}$	Refers to the inner raceway in a roller bearing system
$\mathbf{a}_{outer}$	Refers to the outer raceway in a roller bearing system
$\mathbf{a}_n$	Refers to normal force
$\mathbf{a}_P$	Refers to point P on body i
$\mathbf{a}_Q$	Refers to point Q on body j
$\mathbf{a}_s$	Refers to the number of the slice on a roller
$\mathbf{a}_t$	Refers to tangential force
$\mathbf{a}_{gravitational}$	Force caused by gravity
$\mathbf{a}_{contact}$	Force caused by contact
$\mathbf{a}_{gyroscopic}$	Force caused by gyroscopic forces
$\mathbf{a}_{load}$	Force caused by external load

Latin Symbols

a, b	Semi-axes of the contact ellipse, for point contact, or contact patch, for line contact
$\bar{a}, \bar{b}, n, Y$	Constants for the calculation of normal contact force, for line contact
A	Generic transformation matrix
$\mathbf{A}_{\theta 2}$	Rotation matrix
b	Binormal vector
C	Generic clearance
d, D	Generic diameter
d	Distance vector
D_{iso}	Debroah number
e_0, e_1, e_2, e_3	Euler parameters
E	Young's modulus

E'		Equivalent modulus of elasticity
E^*		Composite modulus of elasticity
f		Generic force
$\mathbf{f}$		Vector of generic forces
$\mathbf{g}$		Vector of generalized forces
G		Material parameter
h		Generic height
h_c		Lubricant film central thickness
h_{iso}		Isothermal central lubricant film thickness
h_{min}		Minimum lubricant film thickness
H		Film thickness parameter
I		Inertia
$\mathbf{J}$		Inertia tensor
K_f		Thermal conductivity
K_{pt}		Contact stiffness
l, L		Generic length
L_T		Thermal loading parameter
L_{ef}		Effective contact length, for line contact
$\mathbf{L}$		Auxiliary matrix, function of Euler parameters
m		Mass of the rigid body
$\mathbf{m}'_i$		Sum of all moments respective to body i
$\mathbf{M}$		Global mass matrix
nb		Total number of bodies in the system
nc		Total number of coordinates
n, m		Constants for calculations with norm ASTM D341
$\mathbf{n}$		Normal vector
N_{sl}		Number of slices in which the roller is divided
$\mathbf{N}$		Diagonal matrix of masses
O		Origin
p		Pressure
$\mathbf{p}$		Orientation of the rigid body built with Euler parameters
$\dot{\mathbf{p}}$		Time derivatives of Euler parameters
P		Generic point on body i
q		Normal compressive load
$\mathbf{q}$		Vector of generalized coordinates
$\dot{\mathbf{q}}$		Vector of generalized velocities
$\dot{\mathbf{q}}^*$		Vector of generalized velocities in the Euler parameter space
$\ddot{\mathbf{q}}$		Vector of generalized accelerations
Q		Generic point on body j
r, R		Generic radius
$r_{ax}, r_{ay}, r_{bx}, r_{by}$		Characteristic radii of contacting surfaces
$\mathbf{r}$		Translational position vector
$\dot{\mathbf{r}}$		Translational velocity vector
s		Slip ratio
s, t		Constants for the calculation of the starvation factor
$\mathbf{s}$		Position vector
$\bar{S}$		Mean dimensionless shear stress
t		Time
$\mathbf{t}$		Tangent vector
T		Temperature
T_0		Reference temperature
$\hat{u}$		Average velocity of the contacting surfaces
$\mathbf{u}$		Sliding velocity of the bodies in the contact point
U		Speed parameter

v	Generic linear velocity
$\mathbf{v}$	Generic linear velocity vector
W	Generic width, or load parameter for the calculation of the lubricant film thickness
x_c	Dimensionless length of the EHL contact area
x, y, z	Global coordinates
X, Y, Z	Global reference frame
$\mathbf{y}, \dot{\mathbf{y}}$	Auxiliary vectors used in the integration process

Greek Symbols

α	Tilt angle of the rollers on the spherical bearing
α_1	Pressure coefficient of viscosity
α_r	Angle of the raceway surface of the tapered bearing
α_m	Pitch angle of a roller in the pitch circle
β	Angular position of a contact point on a cage pocket top, for contact detection
$\boldsymbol{\gamma}$	Right-hand-side of acceleration equations
δ	Penetration, or interference, during contact
δ_t	Viscosity temperature index
ΔR	Characteristic radii, for line contact
η_0	Lubricant viscosity at reference conditions
η	Lubricant viscosity
θ	Angular position of a contact point on a circle of the roller, for contact detection
θ_2	Angular position of a contact point on a surface of revolution, for contact detection
$\kappa, \mathbb{F}, \mathbb{E}, \mathbb{R}$	Constants for the calculation of the contact stiffness, for point contact
$\boldsymbol{\lambda}$	Vector of Lagrange multipliers
Λ	Lubricant film parameter
μ	Equivalent friction coefficient
μ_{bd}	Boundary mode equivalent friction coefficient
μ_{fm}	Full-film mode equivalent friction coefficient
μ^*	Viscosity of the lubricant for the calculation of the full-film equivalent friction coefficient
ν	Poisson's ratio; Kinematic viscosity
σ_1, σ_2	Roughness of contacting surfaces
σ_{avg}	Mean normal stress
$\sigma_{\max}$	Maximum stress
Σ_p	Constant for the calculation of the contact patch dimensions, for line contact
Σ_{iso}	Dimensionless shear velocity of the lubricant
τ_0	Lubricant characteristic stress
ϕ	Angular position of a contact point on a raceway of the spherical bearing, for contact detection
ϕ_S	Starvation factor
ϕ_T	Thermal reduction factor
φ	Angular position of a contact point on a spherical cap
Φ	Vector of kinematic position constraints
χ	Modified factor for side-leakage
ψ	Parameter for the calculation of the full-film equivalent friction coefficient
ω	Angular velocity
$\boldsymbol{\omega}$	Angular velocity vector
$\dot{\boldsymbol{\omega}}$	Angular acceleration vector
$\mu_0^*, \alpha^*, \beta^*,$ $V_1, V_2, V_3,$ B_1, B_2, B_3	Experimental constants for the calculation of the full-film equivalent friction coefficient
ξ, η, ζ	Local, or body-fixed, reference frame

ABBREVIATIONS

MAXBE	Interoperable Monitoring, Diagnosis and Maintenance Strategies for Axle Bearings
FEUP	Faculty of Engineering of University of Porto
CAE	Computer Aided Engineering
BearDyn	Bearing Dynamic Analysis Program
FEA	Finite Element Analysis
BCF	Bearing Characteristic Frequencies
DIM	Direct Integration Method
ODE	Ordinary Differential Equation
SAGA	System Animation for Graphical Analysis
EHL	Elastohydrodynamic Lubrication

1. INTRODUCTION

Railway systems are, nowadays, a highly preferred mean of transportation by passengers, due to their comfort, speed and safety, which have further advanced technologically over the past years. The increase in competitiveness led to a constant need to guarantee their reliability and to improve their performance, justifying research and development of the condition monitoring of these systems. Among the vehicle subsystems, the axle bearing has a direct impact in the safety and economics of railway systems. This subsystem has been the object of study of a collaborative project between several European organizations, which uses the acronym MAXBE – Interoperable Monitoring, Diagnosis and Maintenance Strategies for Axle Bearings. This project appears with the objective to provide concepts and strategies for the interoperable monitoring and diagnosis of axle bearings. The work now presented is developed as part of this project, of which the dynamic performance of the roller bearings used in railway vehicles is the fundamental object.

A bearing is a machine element that allows one part to support another by constraining relative motion between the parts to a rotational or a translation about given axis while allowing for a reduced friction between moving parts. Bearings can be classified in different ways, being one of the broadest division in: contact bearings, which have mechanical contact between the elements, including sliding and rolling bearings, represented in Figure 1; and non-contact bearings, which include externally pressurized and hydrodynamic fluid-film and magnetic bearings, as in Figure 2. In the case of bearings specifically used to ensure motion of a shaft and housing, the direction of force that acts on the bearing can also be a differentiator, dividing bearings into radial and thrust bearings, as shown in Figure 3. Radial bearings support the load in a direction perpendicular to the axis of the shaft and the bearing, while thrust bearings support the load that acts along the axis of the shaft and the bearing. [1] [2]

Rolling contact bearings carry a load by placing rolling elements between two bearing rings, as seen in Figure 1(b). A bearing also usually comprises a cage, which maintains the spacing between the rolling elements and prevents contact between them. The rolling elements roll with a low rolling resistance and sliding, due to the relative motion of the bearing rings. These rolling elements can be balls or rollers, where rollers can have different geometries. Some of the most common roller bearings use cylindrical, spherical, tapered or needle rollers, as represented in Figure 4.

(a)   (b)
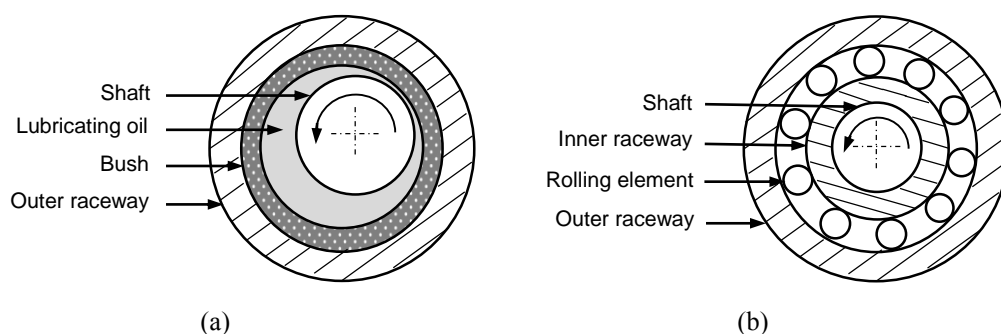
Figure 1: Representation of contact bearings (a) Sliding contact bearing; (b) Rolling contact bearing

(a)	(b)
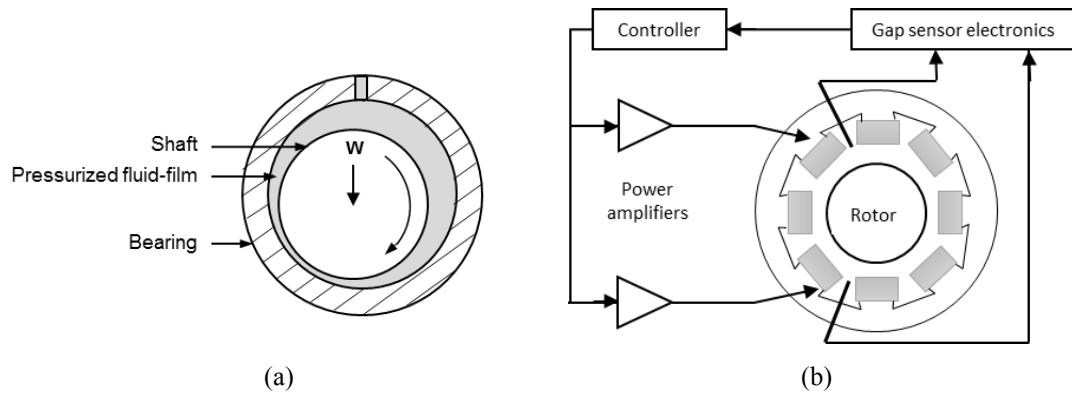
Figure 2: Representation of non-contact bearings; (a) Externally pressurized and hydrodynamic fluid film bearing; (b) Magnetic bearing.

(a)	(b)
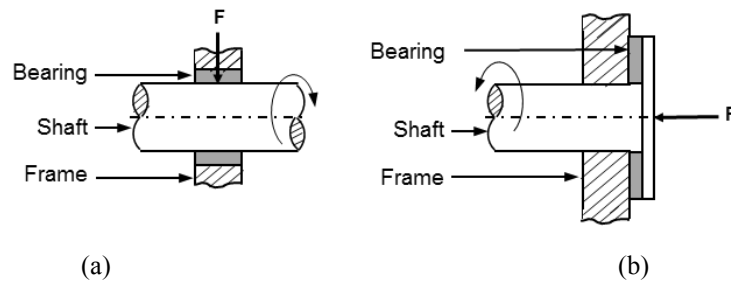
Figure 3: (a) Radial bearing; (b) Thrust bearing.

(a)	(b)	(c)	(d)	(e)
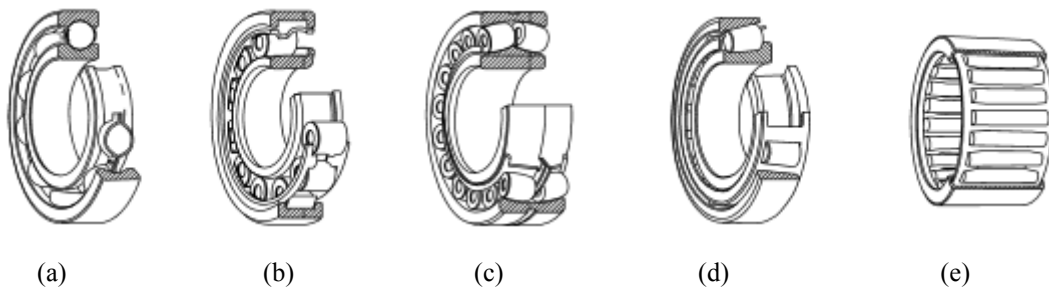
Figure 4: Types of rolling bearings (Figures from reference [3]). (a) Ball; (b) Cylindrical; (c) Spherical; (d) Tapered; (e) Needle.

Ball bearings are either used to sustain radial, axial or both loads, depending on the configuration of the balls between the raceways and the geometry of the raceways, themselves. This type of bearing has low torque, being appropriate for applications where high speed and low power loss are required. Ball bearings have lower load capacity than bearings with rollers, due to the smaller contact area between the balls and races. Cylindrical and needle roller bearings are very similar, being the main difference the ratio between length and diameter of the rollers, where needle roller bearings contain slender rollers with a length 3 to 10 times their diameter. These bearings withstand high radial loads and are suitable for high speeds. Spherical roller bearings have barrel-shaped rollers which are known for their capability for self-alignment. The spherical roller bearings have excellent radial load-carrying capacity and are suitable to be used where heavy or impact loads occur. Tapered roller bearings are capable of sustaining not only high radial loads but also axial loads. [3] [4] [5]

In the railway industry, there is a big focus on the selection, understanding and maintenance of bearings, resulting from their direct impact on train safety and inactivity periods for maintenance.

Bearings which are part of the wheelset of a train are given special attention. The essential design concept for railway wheels has remained unchanged throughout their existence, where the assembly of two railway wheels and an axle, the wheelset, has a free relative rotation and it is supported by bearings housed in an axlebox. Axleboxes are the linking element between the rotating wheelset and the frame of the boggie via the primary suspension of a railway vehicle. All forces acting between the axleboxes are transmitted via springs, dampers and guiding elements i.e., the primary suspension, to the boggie frame. An image of an axlebox mounted on a train is shown in Figure 5(a) while Figure 5(b) shows an internal arrangement of another axlebox.

The axlebox is an assembly normally comprising the axlebox housing, rolling bearings, sealing solution and proper lubricant. An example of an axlebox is seen in Figure 5(b), where a double row tapered roller bearing is visible in the interior of the axlebox. The bearings predominantly used in these applications are spherical and tapered bearings [6]. Due to the integration of the work now presented in the MAXBE project, only bearings with spherical and tapered rollers, presented in Figure 6, are considered here.

(a)	(b)
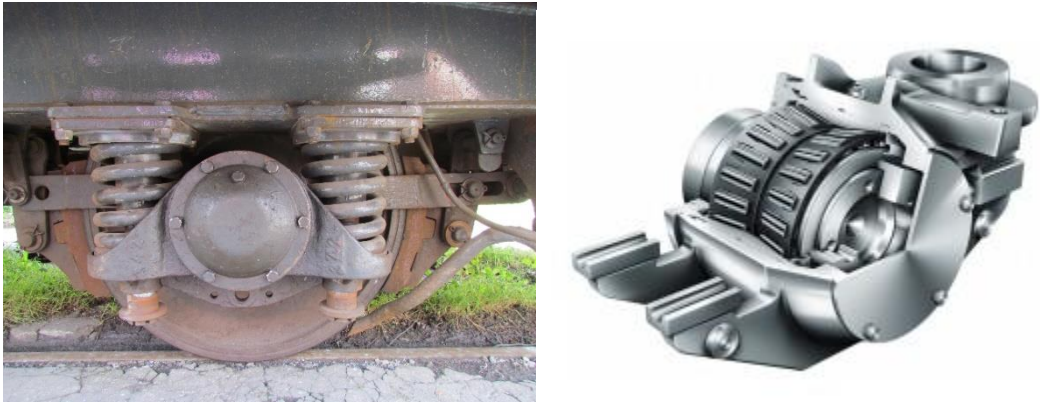
Figure 5: Axleboxes for railway application. (a) Image of a mounted axlebox; (b) Axlebox representation (Figure adapted from [7]).
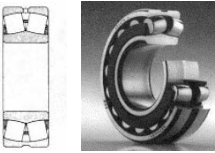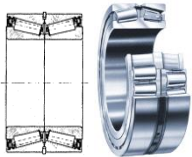
Spherical Roller Bearings

Partner: DL
Roller: 22219-S-MB-F2-C3 (FAG)
Dimensions: 95x170x43

Partner: EMEF
Roller: 22330 CCK C3 W33 (SKF)
Dimensions: 150x320x108

Tapered Roller Bearings

Partner: EMEF
Roller: BT2-7088 (SKF)
Dimensions: 130x230x160

Partner: COMSA
Roller: HM 13343690952 (TIMKEN)
Dimensions: 150x250x160

(a)	(b)

Figure 6: Axlebox roller bearings of different vehicles used in MAXBE Project. (a) Spherical bearing; (b) Tapered bearing.

Failure of a bearing often leads to total shutdown of the machine of which it is part and, therefore, it often requires long inactivity periods for its maintenance. Statistics show that industrial bearings are considered as critical mechanical components which represent between 40% and 50% of the malfunctions in rotating machinery [8]. As the failure of components in the rolling element bearing support system is one of the most significant factors in the ever-increasing mechanical safety incidents and the cost of maintenance programs, faults occurring in the bearings must be detected as early as

possible [9]. Failure of the bearing can occur for a variety of reasons, most of them avoidable. However, there is no discussion about the difficulty in identifying the causes of premature failure. Several studies are focused in identifying the most common sources of these problems, usually by experimental analysis and comparison of repeated occurrences. The existence of localized defects on a bearing are usually the most critical reason for it to fail, although there are other aspects which can also be responsible for the failure. An image of typical defects identified on an outer raceway of a tapered bearing is shown in Figure 7. Dhameliya [10] recently studied the causes of failure in railway bogies, concluding that proper bearing lubrication is one of the most important aspects to avoid accidental damage. In the process, Dhameliya [10] also concludes that the spherical roller bearings are preferred to cylindrical roller bearings, due to their self-aligning geometry. Fatigue failure is also one of the main causes for bearing failure, usually beginning with small cracks which gradually propagate to the surface of the bearing generating detectable vibrations. This situation can result from poor design of the bearing or simply from continued stressing, which is unavoidable. While these are common reasons for failure in rolling-element bearings, there are other conditions which reduce bearing life, such as external sources including contamination, corrosion, improper installation or brinelling, which is the formation of indentations in the raceways caused by static overloading or by exposition to vibrations while being stationary [11] [12]

Figure 7: Typical defects on a bearing outer raceway.

Bearings with defects can also lead to problems in other components of axleboxes, since they can cause overheating of the axle when combined with insufficient high-temperature strength of the material [13]. Also, fatigue fractures of the inner rings of the bearings can lead to failures in axles, after the dynamic strength of the bearings is exceeded, causing the rings to widen [14]. Different experimental methods have been proposed for detection and diagnosis of bearing defects which may be broadly classified such as vibration and acoustic measurements, temperature measurements, defect signatures, wear debris and lubricant analysis. Vibration measurements are the most widely used [8] [15]. Faults which typically occur in rolling element bearings caused by localized defects generate a series of impact vibrations every time a running roller passes over the surfaces of the defects. These vibrations occur at Bearing Characteristic Frequencies (BCF), which are estimated based on the running speed of the shaft, the geometry of the bearing and the location of the defect. Theoretically, the Fast Fourier Transforms spectra of BCF can be generated and observed by the machine operator to analyse the change of vibration

4

amplitude and detect the existence of faults. There are, however, difficulties in this process, since the impact vibration is usually overwhelmed by noise and vibrations generated from other components, such as the rail-wheel contact [16].

Due to the difficulties that arise from using data from experimental methods, to predict the life of a bearing, theoretical methods are seen as an advantageous alternative. The performance limitations of a mechanical system can often be determined by the dynamic response of its subsystems. In the cases of systems that include roller bearings, it is necessary to predict bearing dynamic performance as an integral part of machine design analysis, which can be done by studying the dynamic response of a bearing under load and speed [17]. Several numerical studies have been carried and published in order to allow the study of dynamic analysis of roller bearings for different geometries and applications. It is the case of Ghalamchi et al. [18], who created a simple dynamic model of a spherical roller bearing, which takes into account the influences of roller angular position on bearing contact forces to predict the transient dynamic behaviour of a rotor-spherical bearing system. Qian W. [19] carried a dynamic simulation of a cylindrical roller bearing, in the multibody code SIMPACK. Li-xin et al. [20] modelled and analysed planar multibody systems containing deep groove ball bearings with clearance, where the bearing joint is modelled by introducing a nonlinear constraint force system. From this study, the simulations of the normal contact forces on each ball element can be used for the strength checking and fatigue life prediction of the joint with deep groove ball bearing.

With the progress of computer technology, Computer Aided Engineering (CAE) becomes popular and essential to design better bearings to match user requirements with optimized performance. In this context, some dynamic bearing analysis programs were created, such as ADORE, which is a commercially available software package that allows its users to analyse the performance of roller and ball bearings by using multibody formulation to describe the elements of the bearing and their interactions [21] [22]. IBDAS [23], BRAIN [21] and BEAST [24] are some other examples of similar tools that also use this approach but that are proprietary of roller bearing manufacturers. These software allow the user to develop theoretically almost any type of roller bearing. However, in some cases, specific studies are needed to be performed which require specifications or geometries different from the ones allowed by the commercial programs enumerated. Here, simulations can be performed with commercial Finite Element Analysis (FEA) programs, where the roller bearing is easily modelled. Sakaguchi et al. developed a code based on ADAMS that can simulate real-time behaviour of a cylindrical roller bearing, as well as an optimized code which allowed analysis of a high-load capacity tapered roller bearing [25] [26]. However, even though these programs allow short simulation times and lower costs, the use of FEA commercial computational tools usually does not allow such a precise analysis of the roller bearings, since several simplifications are implied in the simulation, mainly relative to contact and friction models.

The approach used here includes the development of a dynamic analysis tool, referred to as `BearDyn` which serves as the acronym for Bearing Dynamic Analysis Program, able to handle bearing

models representative of the actual bearings used in railway operations, developed in MATLAB®. This code uses a multibody formulation to describe the elements of the bearing and their interactions. The interactions between the rollers, cage, and raceways are described by continuous contact force models based on the Hertz elastic contact theory [27] and modified according to experimental evidence. Tribological lubrication models are applied to describe the tangential forces in the presence of lubricant [28] [29]. This work constitutes the description of the dynamic analysis tool, `BearDyn`, its fundamental formulations and its application to realistic models of spherical and tapered roller bearings.

1.1.   Work description

The objectives of this work require the understanding of the performance of the axle bearings in actual operation conditions and include the development of a dynamic analysis tool able to handle bearing models representative of the actual bearings used in railway operations. The final goal of the work described in this document is to obtain a dynamic analysis tool `BearDyn` which is able to perform a study on different types of roller bearings, whose models are described by data in dedicated files. The dynamic response of the forces is to be post-processed to obtain the Frequency Response Functions (FRF), which serve as the basis for the evaluation of the bearing health. The development of the necessary methods for the dynamic analysis of the bearings is presented, being the methods for contact between elements and tribology contact models also included. The demonstration of the developed program is done by performing dynamic analysis of realistic models.

In order to allow realistic simulations and prepare the program for the purpose intended, the inputs and models used for the formulation and functioning of `BearDyn` must be as accurate as possible, preferably by being compatible with methods and models used by other partners of project MAXBE. In this sense, the work now presented includes not only the developments by the author but also background knowledge made accessible. The structure of the models and theoretical knowledge, in which the body of the work is done, is available in the work by Ambrósio [30] delivered to project MAXBE. This reference presents most of the models and methods to be implemented in `BearDyn`, namely the dynamic analysis and methods of solving equations of motion. The computer implementation of the methods in reference [30] required modification, devised and clarified by the author of this work. The chapter concerning geometric characterization of the bearings, and the kinematic initialization of its components such as positions, orientations and velocities of each body of the system, was revised by the author and described in Chapter 3. Chapter 4 describes the general formulations for rolling contact detection, based on the work reported in reference [30]. The implementation of the methods initially proposed by Ambrósio are further enhanced and the algorithms are debugged and revised in this chapter. The evaluation of the normal and tangential forces, when applied to roller bearing mechanical components, have several accurate models available in the literature, which are found in references by other authors who describe the forces developed in rolling bodies when accounting for high loads and

specific geometries. The necessary study and gathering of these models carried in reference [30] was further enhanced and corrected in some aspects in this work and described in Chapter 5.

The dynamic analysis of realistic models requires accurate data. The geometries of the bearing mechanical elements, which are inputs of `BearDyn`, had to be identified as precisely as possible, otherwise the coherence and representability of results could be compromised. Due to the lack of availability of the full necessary geometrical data of common roller bearings, or even of roller bearings used for other studies of project MAXBE, physical measurements were made to obtain the detailed geometries. A campaign of measurements of the spherical and tapered roller bearing components geometry was carried at the Faculty of Engineering of University of Porto (FEUP) with the support and involvement of the research group in tribology. The author of this work identified the geometrical features to be measured while the actual measurements were carried by members of the tribology research group of FEUP. The data obtained is included in Chapter 3 and Appendix A - Input Data for Bearing Model.

The computational methods used to create `BearDyn` and to verify its performance are detailed in Chapter 6. The preliminary results of the dynamic analysis program `BearDyn` in a realistic operational scenario are presented in Chapter 7. The numerical results are complemented by sequences of time frames from computer animations of the roller bearings that help the reader to visualize the roller bearing kinematics. Finally a set of conclusions is highlighted in Chapter 8 and a list of recommendations for future work is presented.

2. DYNAMIC ANALYSIS

This chapter presents the formulation of the general equations of motion to the spatial dynamic analysis of multibody systems. In this work only the formulations related to roller bearings are described. Note that in a more general implementation the roller bearings can be included as sub-systems of more general multibody systems. The methodology presented can be implemented in any general purpose multibody code, being implemented in particular in the computer program `BearDyn`.

2.1. Kinematics of a rigid body

Due to its simplicity and computational easiness, Cartesian coordinates and Newton-Euler's method are used to formulate the equations of motion of the spatial multibody systems [31].
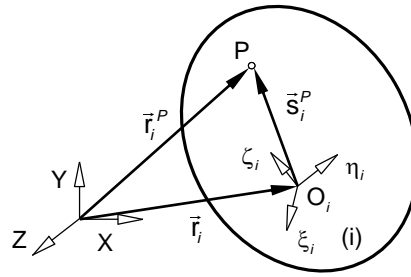
Figure 8: Cartesian coordinates for a rigid body

Let Figure 8 represent a rigid body i to which a body-fixed coordinate system $(\xi\eta\zeta)_i$ is attached at its centre of mass. When Cartesian coordinates are used, the position and orientation of the rigid body must be defined by a set of translational and rotational coordinates. The position of the body with respect to global coordinate system XYZ is defined by the coordinate vector $\mathbf{r}_i = [x \quad y \quad z]_i^T$ that represents the location of the local reference frame $(\xi\eta\zeta)_i$. The orientation of the body is described by the rotational coordinate's vector $\mathbf{p}_i = [e_0 \quad e_1 \quad e_2 \quad e_3]_i^T$, which is built with the Euler parameters for the rigid body [31]. Therefore, the vector of coordinates that describes completely the rigid body i is,

$$\mathbf{q}_i = [\mathbf{r}_i^T \quad \mathbf{p}_i^T]_i^T \tag{2.1}$$

A spatial multibody system with nb bodies is described by a set of coordinates $\mathbf{q}$ in the form,

$$\mathbf{q} = [\mathbf{q}_1^T, \mathbf{q}_2^T, ..., \mathbf{q}_{nb}^T]^T \tag{2.2}$$

The location of point P on body i can be defined by position vector $\mathbf{s}_i^P$ with respect to the body-fixed reference frame $(\xi\eta\zeta)_i$ and by the global position vector $\mathbf{r}_i$, that is,

$$\mathbf{r}_i^P = \mathbf{r}_i + \mathbf{s}_i^P = \mathbf{r}_i + \mathbf{A}_i \mathbf{s}_i'^P \tag{2.3}$$

where $\mathbf{A}_i$ is the transformation matrix for body i that defines the orientation of the referential $(\xi\eta\zeta)_i$ with respect to the referential frame XYZ. The transformation matrix is expressed as function of the four Euler parameters as [31],

$$\mathbf{A}_i = 2 \cdot \begin{bmatrix} e_0^2 + e_1^2 - \frac{1}{2} & e_1 e_2 - e_0 e_3 & e_1 e_3 + e_0 e_2 \\ e_1 e_2 + e_0 e_3 & e_0^2 + e_2^2 - \frac{1}{2} & e_2 e_3 - e_0 e_1 \\ e_1 e_3 - e_0 e_2 & e_2 e_3 + e_0 e_1 & e_0^2 + e_3^2 - \frac{1}{2} \end{bmatrix} \tag{2.4}$$

Notice that the vector $\mathbf{s}_i^P$ is expressed in global coordinates whereas the vector $\mathbf{s}_i'^P$ is defined in the body i fixed coordinate system.

The velocities and accelerations of body i use the angular velocities $\boldsymbol{\omega}_i'$ and accelerations $\dot{\boldsymbol{\omega}}_i'$ instead of the time derivatives of the Euler parameters, which simplifies the mathematical formulation and do not require the use of a mathematical constraint for Euler parameters. This is, the relation between the Euler parameters $\dot{e}_0 + \dot{e}_1 + \dot{e}_2 + \dot{e}_3 = 0$ is implied in the angular velocity and, therefore, does not be used explicitly [32]. When Euler parameters are employed as rotational coordinates, the relation between their time derivatives and the angular velocities is expressed by [31],

$$\dot{\mathbf{p}}_i = \tfrac{1}{2} \mathbf{L}^\mathrm{T} \boldsymbol{\omega}_i' \tag{2.5}$$

where the auxiliary 3×4 matrix $\mathbf{L}$ is function of Euler parameters,

$$\mathbf{L}_i = \begin{bmatrix} -e_1 & e_0 & e_3 & -e_2 \\ -e_2 & -e_3 & e_0 & e_1 \\ -e_3 & e_2 & -e_1 & e_0 \end{bmatrix}_i \tag{2.6}$$

The velocities and accelerations of body i are given by vectors,

$$\dot{\mathbf{q}}_i = [\dot{\mathbf{r}}_i^T \quad \boldsymbol{\omega}_i'^T]_i^T$$
$$\ddot{\mathbf{q}}_i = [\ddot{\mathbf{r}}_i^T \quad \dot{\boldsymbol{\omega}}_i'^T]_i^T \tag{2.7}$$

The knowledge of the system response includes the evaluation of the position, orientation, velocity and acceleration of all the components of the system. For this purpose, the equations of motion of the system must be established and their solution evaluated and integrated in time.

2.2. Dynamics of a multibody system

In terms of Cartesian coordinates, the equations of motion of an unconstrained multibody mechanical system are written as,

$$\mathbf{M}\ddot{\mathbf{q}} = \mathbf{g} \tag{2.8}$$

where $\mathbf{M}$ is the global mass matrix, containing the mass and moment of inertia of all bodies and $\mathbf{g}$ is a force vector that contains the external and internal forces acting on the bodies of the system.

For a constrained multibody system, the kinematical joints are described by a set of holonomic algebraic constraints denoted as,

$$\boldsymbol{\Phi}(\mathbf{q}, t) = \mathbf{0} \tag{2.9}$$

Using the Lagrange multipliers technique the constraints are added to the equations of motion. These are written together with the second time derivative of the constraint equations. Thus, the set of equations that describe the motion of the multibody system is,

$$\begin{bmatrix} \mathbf{M} & \mathbf{\Phi}_q^T \\ \mathbf{\Phi}_q & \mathbf{0} \end{bmatrix} \begin{Bmatrix} \ddot{\mathbf{q}} \\ \boldsymbol{\lambda} \end{Bmatrix} = \begin{Bmatrix} \mathbf{g} \\ \boldsymbol{\gamma} \end{Bmatrix} \qquad (2.10)$$

where $\boldsymbol{\lambda}$ is the vector of Lagrange multipliers and $\boldsymbol{\gamma}$ is the vector that groups all the terms of the acceleration constraint equations that depend on the velocities only, that is,

$$\boldsymbol{\gamma} = -(\mathbf{\Phi}_q \dot{\mathbf{q}})_q \dot{\mathbf{q}} - \mathbf{\Phi}_{tt} - 2\mathbf{\Phi}_{qt} \dot{\mathbf{q}} \qquad (2.11)$$

The Lagrange multipliers, associated with the kinematic constraints, are physically related to the reaction forces and moments generated between the bodies interconnected by kinematic joints. This system of equations is solved for $\ddot{\mathbf{q}}$ and $\boldsymbol{\lambda}$. Then, in each integration time step, the accelerations vector, $\ddot{\mathbf{q}}$, together with velocities vector, $\dot{\mathbf{q}}$, are integrated in order to obtain the system velocities and positions for the next time step.

In the computational tool `BearDyn` developed for this project, kinematic constraints were not introduced as its range of application includes isolated roller bearings only. Consequently, the system is defined as a system of unconstrained bodies, where the equations of motion are used in a simplified form to avoid calculations with matrices with an unnecessary number of null entries. In a system of unconstrained bodies, as represented in Figure 9(a), it is assumed that there are *nb* bodies connected by various force elements. All bodies are considered as unconstrained, where their motion is confined by contact and by fixation of the outer raceway in space. A free-body diagram representative of a generic body from the system is shown in Figure 9(b).

(a)   (b)
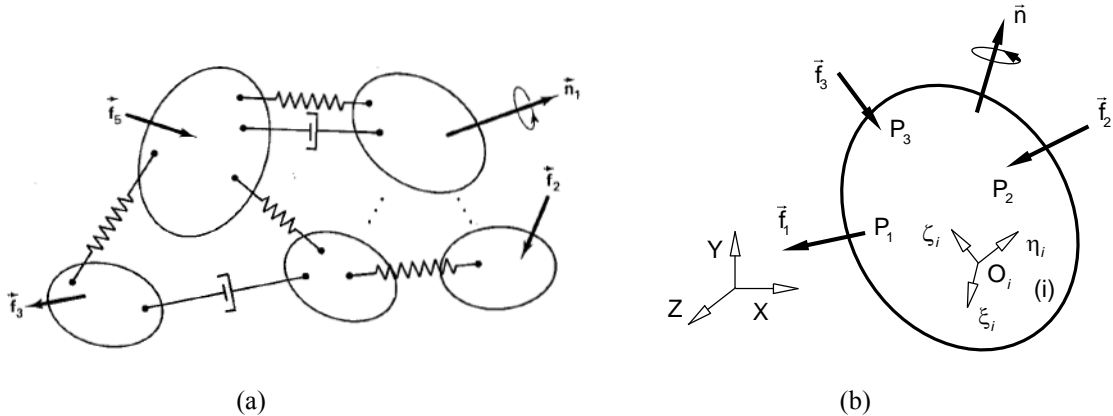
Figure 9: (a) Representation of a system of unconstrained bodies (figure adapted from [31]); (b) Free-body diagram of an unconstrained body.

The equations of motion of the *i*th unconstrained body can then be expressed as [31],

$$\mathbf{M}_i \ddot{\mathbf{q}}_i = \mathbf{g}_i \qquad (2.12)$$

where,

$$\mathbf{M}_i = \begin{bmatrix} \mathbf{N} & \mathbf{0} \\ \mathbf{0} & \mathbf{J}' \end{bmatrix}_i ; \quad \ddot{\mathbf{q}}_i = \begin{bmatrix} \ddot{\mathbf{r}} \\ \dot{\boldsymbol{\omega}}' \end{bmatrix}_i ; \quad \mathbf{g}_i = \begin{bmatrix} \mathbf{f} \\ \mathbf{m}' \end{bmatrix}_i \qquad (2.13)$$

in which the sum of all forces acting on the body is $\mathbf{f}_i$, the sum of all moments denoted by $\mathbf{m}'_i$, $\mathbf{J}'_i$ the inertia tensor for the body, and $\mathbf{N}_i$ is,

10

$$\mathbf{N}_i = \mathrm{diag}\left[m, m, m\right]_i \tag{2.14}$$

where m is the mass of the body.

In summary, at each time step it is necessary to evaluate the vector of forces $\mathbf{g}$, which is used to obtain the system accelerations $\ddot{\mathbf{q}}$, by solving Eq.(2.8) by applying any method suitable for the solution of linear algebraic equations. The system accelerations, $\ddot{\mathbf{q}}$, together with the velocities $\dot{\mathbf{q}}^*$, are integrated to obtain the new velocities $\dot{\mathbf{q}}$ and positions $\mathbf{q}$ for the next time step. This process is repeated until the complete description of the system motion is obtained for a selected time interval. It is important to note that, in vector $\dot{\mathbf{q}}^*$, the angular velocities are substituted by the time derivatives of the Euler parameters using Eq.(2.5).

2.3.   External and internal forces

Of particular interest in the application of the multibody dynamics formulation to the representation and solution of railway vehicle and bearing rolling element dynamics is the construction of the force vector $\mathbf{g}$. Realistically, this vector includes all the external and internal applied forces in the system, namely, the springs, dampers and actuator forces, the gravitational forces, the wheel-rail contact forces, the normal, hydrodynamic, elastohydrodynamic and friction forces between bearing rolling elements and the gyroscopic forces of the rigid bodies. Among these, the wheel-rail contact forces and the internal roller bearing forces are of importance for this work and are introduced in force vector $\mathbf{g}$. At each integration time step it is calculated by,

$$\mathbf{g} = \mathbf{f}_{gravitational} + \mathbf{f}_{contact} + \mathbf{f}_{gyroscopic} + \mathbf{f}_{load} \tag{2.15}$$

where $\mathbf{f}_{gravitational}$ is the vector of gravitational forces acting on the system, constant over each integration; gravitational forces are applied in each body's centre of gravity, which coincides with its geometrical centre, in the negative vertical direction with a magnitude of 9.81 times the body's mass. $\mathbf{f}_{contact}$ is a vector containing the forces resulting from contact between bearing rolling elements, including normal, elastohydrodynamic and friction forces; the calculation of these forces is detailed in Section 5. The gyroscopic forces of the rigid bodies are introduced in vector $\mathbf{f}_{gyroscopic}$ and are calculated at each time step by [31],

$$\mathbf{f}_{gyroscopic} = -\tilde{\boldsymbol{\omega}}_i' \mathbf{J}_i' \boldsymbol{\omega}_i' \tag{2.16}$$

where $\mathbf{J}_i'$ is the moment of inertia matrix of the correspondent body. The wheel-rail contact forces are not evaluated by `BearDyn` in the present stage of this work. The `BearDyn` code is, yet, prepared to receive a table of forces resulting from wheel-rail contact over time and apply them in the correspondent body with proper magnitude and direction in each time step due to interpolation of the given table. The given forces are introduced in vector $\mathbf{f}_{load}$.

2.4. Direct integration method of the equations of motion

In this section, the main numerical aspects related to the standard integration of the equations of motion of a multibody system are reviewed. The standard integration of the equations of motion, here called Direct Integration Method (DIM), converts the *nc* second-order differential equations of motion into *2nc* first-order differential equations. Then, a numerical scheme, such as the Runge-Kutta method, is employed to solve the initial-value problem [33].

The *2nc* differential equations of motion are solved, without considering integration numerical errors that can occur and, consequently, during the simulation the propagation of these kinds of errors results in constraint violations, if kinematic constraints are used in the multibody model. The two error sources that lead to constraint violations for any numerical integration step are truncation and round-off errors. Truncation or discretization errors are caused by the nature of the techniques employed to approximate values of a function, $\mathbf{y}$. Round-off errors are due to the limited numbers of significant digits that can be retained by a computer. The commonly used numerical integration algorithms are useful in solving first-order differential equations that take the form [33],

$$\dot{\mathbf{y}} = f(\mathbf{y}, t) \tag{2.17}$$

Thus, if there are *nc* second-order differential equations, they are converted to *2nc* first-order equations by defining the $\mathbf{y}$ and $\dot{\mathbf{y}}$ vectors, which contains, respectively, the system positions and velocities and the system velocities and accelerations, as follows,

$$\mathbf{y} = \begin{Bmatrix} \mathbf{q} \\ \dot{\mathbf{q}} \end{Bmatrix} \quad \text{and} \quad \dot{\mathbf{y}} = \begin{Bmatrix} \dot{\mathbf{q}} \\ \ddot{\mathbf{q}} \end{Bmatrix} \tag{2.18}$$

The reason for introducing the new vectors $\mathbf{y}$ and $\dot{\mathbf{y}}$ is that most numerical integration algorithms deal with first-order differential equations [34]. The following diagram can interpret the process of numerical integration at instant of time *t*,

$$\dot{\mathbf{y}}(t) \xrightarrow{\text{Integration}} \mathbf{y}(t + \Delta t) \tag{2.19}$$

In other words, velocities and accelerations at instant *t*, after integration process, yield positions and velocities at next time step, $t=t+\Delta t$.

Figure 10 presents a flowchart that shows the algorithm of Direct Integration Method of the Eqs. of motion for the methodology approached in this work. At $t=t^0$, the initial conditions on $\mathbf{q}^0$ and $\dot{\mathbf{q}}^0$ are required to start the integration process. The direct integration algorithm shown in Figure 10 can be summarized by the following steps,

1. Start at time t^0 with given initial conditions for positions $\mathbf{q}^0$ and velocities $\dot{\mathbf{q}}^0$.

2. Assemble the global mass matrix $\mathbf{M}$ and calculate the force vector $\mathbf{g}$.

3. Solve the linear equation (2.8) in order to obtain the accelerations $\ddot{\mathbf{q}}$ at time *t*.

4. Assemble the vector $\dot{\mathbf{y}}$ containing the generalized velocities $\dot{\mathbf{q}}$ and accelerations $\ddot{\mathbf{q}}$ for instant of time *t*.

12

5. Integrate numerically the $\dot{\mathbf{q}}$ and $\ddot{\mathbf{q}}$ for time step $t+\Delta t$ and obtain the new positions and velocities.

6. Update the time variable, go to step 2 and proceed with the process for a new time step, until the final time of analysis is reached.
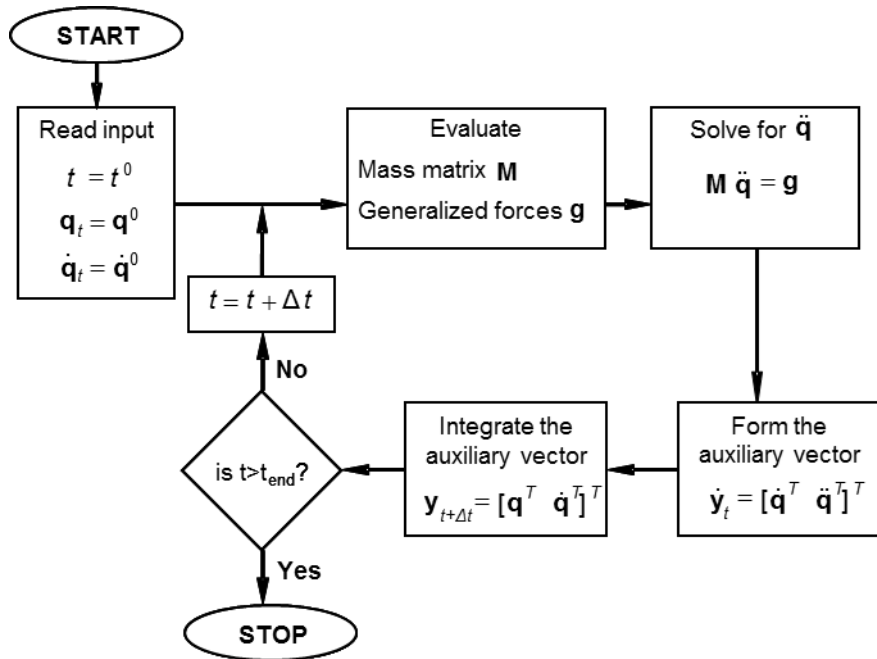
Figure 10: Flowchart of computational procedure for dynamic analysis followed in `BearDyn`.

3. INITIALIZATION OF THE BEARING ROLLING ELEMENTS

The dynamic analysis of the roller bearings, or of the systems containing the roller bearings, requires that the positions and velocities of each component of the bearing is known and properly initialized. Typically each bearing includes an outer raceway, an inner raceway, a cage and a defined number of rollers. An example of a 2 row tapered bearing model is illustrated in Figure 11. Due to the precision with which the bearings are mounted, with tight tolerances, and the complexity of the geometries it is necessary to build a pre-processor that, based on a limited set of data is able to evaluate the position, orientation and the velocities of all rolling elements of the bearing.

(a)   (b)
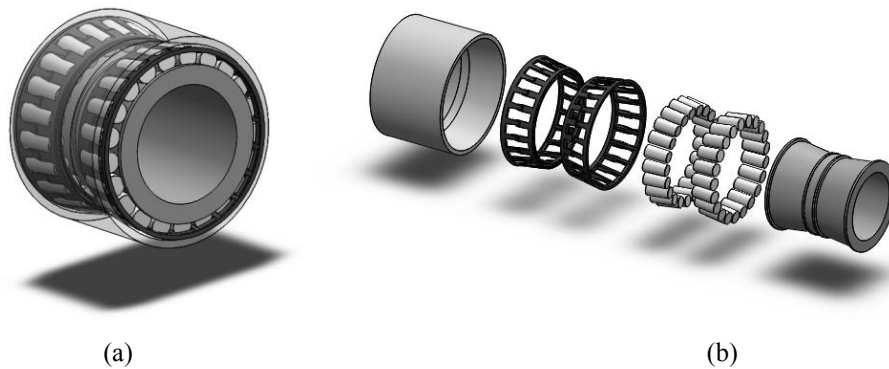
Figure 11: Typical tapered rolling bearing elements. (a) Assembled roller bearing, with a semi-transparent outer raceway; (b) Individual elements of the rolling bearing, from left to right: outer raceway, cages, rollers and inner raceway.

Common to all bearings possible to be modelled and analysed in the bearing analysis program, the data listed in Table 1 is required.

Bearing type reference	*1*	Spherical
	2	Tapered
Number of rollers in the bearing	*nb*	
Outer diameter of the bearing	d_o	
Inner diameter of the bearing	d_i	
Pitch diameter of the bearing	d_m	
Bearing width	*L*	

Table 1: Information required for the general dimensioning of a roller bearing

The dimensions listed in Table 1 are described for the geometrical features shown in Figure 12. The data necessary is provided to `BearDyn` by the user as an input text file with a defined format. For more information on this data, refer to the `BearDyn` user manual, presented here in Appendix A - Input Data for Bearing Model.

Because the roller bearings used in the axleboxes considered in the project are spherical and tapered roller bearings, only the initialization of these types of bearings is considered in this work. At this point it is assumed that the bearings are in full functional conditions and that they have no defects. At a later stage of the project, not considered in this work, a selected number and type of defects in the roller bearings must be considered and models for such defected bearings developed. At that point, the program `BearDyn` can be upgraded to allow the simulation of bearings with defects.

(a)   (b)   (c)
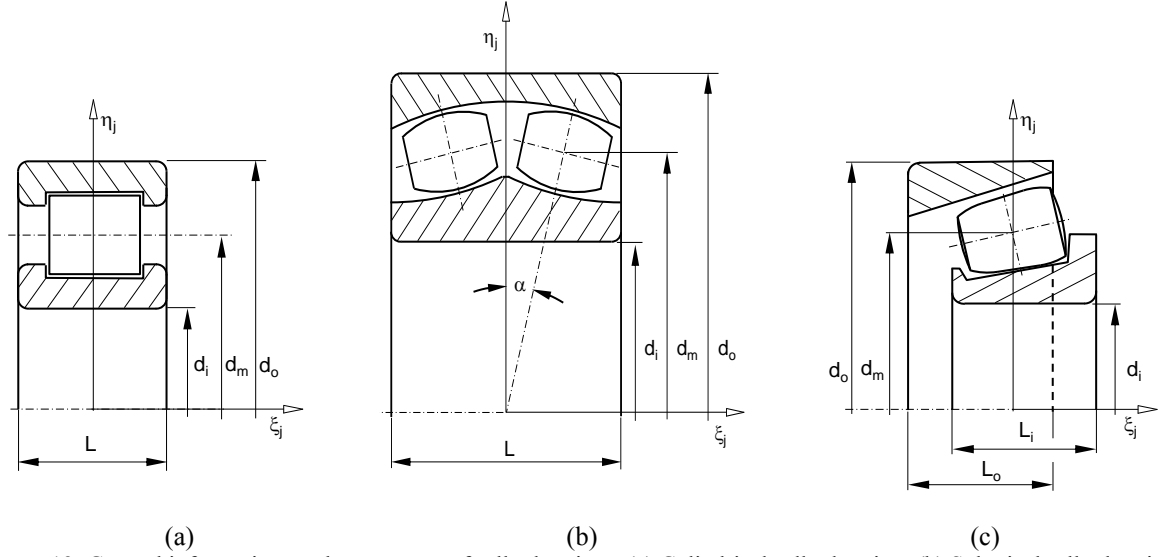
Figure 12: General information on the geometry of roller bearings. (a) Cylindrical roller bearing; (b) Spherical roller bearing; (c) Tapered roller bearing.

3.1.   Spherical roller bearing elements initialization

The geometric details required for the construction of the multibody model of the spherical roller bearing includes the information contained in Table 2. Notice that the data is structured equally in the case of single and double row bearings.

Roller diameter	D_b
Roller lenght	L_b
Roller crown radius	R_{cr}
Roller corner radius on the left side	R_{coL}
Roller corner radius on the right side	R_{coR}
Inner race radius	R_{ir}
Outer race radius	R_{or}
Race clearance	t_c
Inner race lenght	L_{il}
Tilt	α

Table 2: Information required for the general dimensioning of a spherical roller bearing

The geometry of the spherical roller bearing is depicted in Figure 13 where the description of the data necessary to the geometric features of the bearing are identified. Based only on the information contained in Table 2 it is possible to define the complete initialization of the position of the rolling elements in the spherical roller bearing. The body fixed coordinate systems of the outer and inner raceways and the cage of the spherical bearing are assumed to be initially coincident with the inertia frame being all the axis equally oriented, i.e., the frames $(\xi,\eta,\zeta)_i \equiv (X,Y,Z)$. The initial positions and orientations of the elements of the spherical bearing, with the exception of the rollers are,

$$\mathbf{r}^0_{inner} = \mathbf{r}^0_{outer} = \mathbf{r}^0_{cage} = \begin{Bmatrix} 0 \\ 0 \\ 0 \end{Bmatrix} \tag{3.1}$$

$$\mathbf{p}^0_{inner} = \mathbf{p}^0_{outer} = \mathbf{p}^0_{cage} = \begin{Bmatrix} 1 \\ 0 \\ 0 \\ 0 \end{Bmatrix} \tag{3.2}$$

15

(a)   (b)   (c)
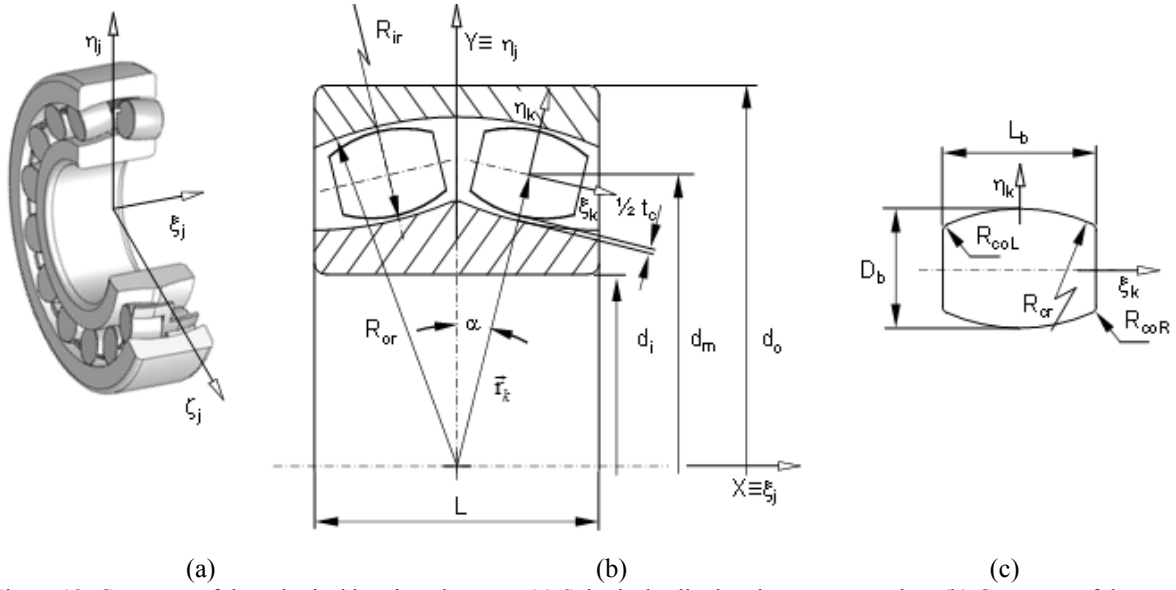
Figure 13: Geometry of the spherical bearing elements. (a) Spherical roller bearing representation; (b) Geometry of the cross-section of the roller bearing; (c) Geometry of the roller.

The positions and orientations of the rollers are dependent on the bearing having one or two rows. The tilt angle α is used to define the existence of a second row of rollers, in case it is not null. In any case, the rollers are positioned on the pitch circle as implied in Figure 14. The rollers are numbered as $b=1,2,\ldots,nb$, starting with the first roller positioned on the intersection between the pitch circle and the Y axis.

(a)   (b)
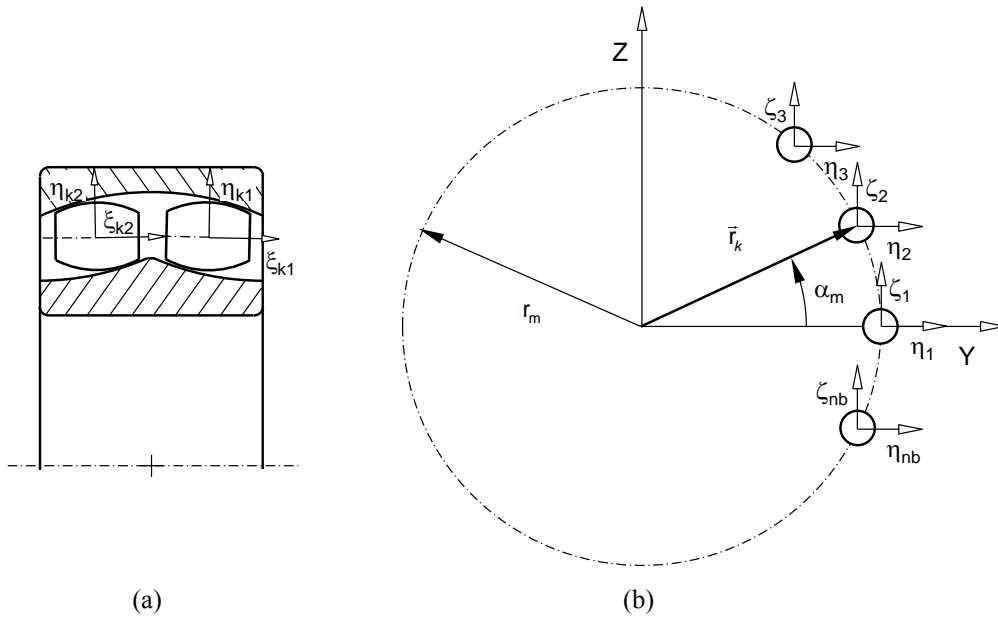
Figure 14: Position of the rollers in the pitch circle: (a) Orientation of the rollers in the cross-section of the bearing; (b) Position of each roller in the pitch circle.

The pitch angle α_m and the length of vector $\mathbf{r}_k$, shown in Figure 14, are obtained from the pitch diameter and tilt angle by,

$$\alpha_m = \frac{2\pi}{nb} \tag{3.3}$$

$$\|\mathbf{r}_k\| = \frac{1}{2}\frac{d_m}{\cos\alpha} \tag{3.4}$$

For a single row spherical bearing, $\alpha=0$ and the positions and orientations of the rollers are straight forward,

$$\mathbf{r}_b^0 = r_m \begin{Bmatrix} 0 \\ \cos\left[(b-1)\alpha_m\right] \\ \sin\left[(b-1)\alpha_m\right] \end{Bmatrix} \quad b=1,2,...,nb \tag{3.5}$$

$$\mathbf{p}_b^0 = \begin{Bmatrix} 1 \\ 0 \\ 0 \\ 0 \end{Bmatrix} \quad b=1,2,...,nb \tag{3.6}$$

in which $r_m=\frac{1}{2}d_m$ is the pitch radius. The orientation of the rollers is such that the body fixed referential $(\xi,\eta,\zeta)_b$ associated to each one of them remains parallel to the inertia frame (X,Y,Z). For a roller bearing with two rows, the development of the positions and orientations of the rollers is detailed in Appendix B – Two Row Spherical Bearing Initializations.

Besides the initial position and orientations of the rolling elements it is also necessary to define the initial velocities of the elements in order to establish the initial conditions for the dynamic analysis. It is assumed that the roller bearing has all its elements rotating about its local ξ. For a spherical roller with one row all the elements of the roller bearing are always in the plane YZ, as depicted in Figure 15. For a two row spherical bearing and for tapered bearings, presented in the next chapter, the rollers rotate in a different plane. Note that at a later stage when assembling the bearing to the shaft of the wheelset and to the axel box the positioning and initial velocities have to be transformed from the initial ones. Such transformation will be addressed in the framework of the complete multibody system.
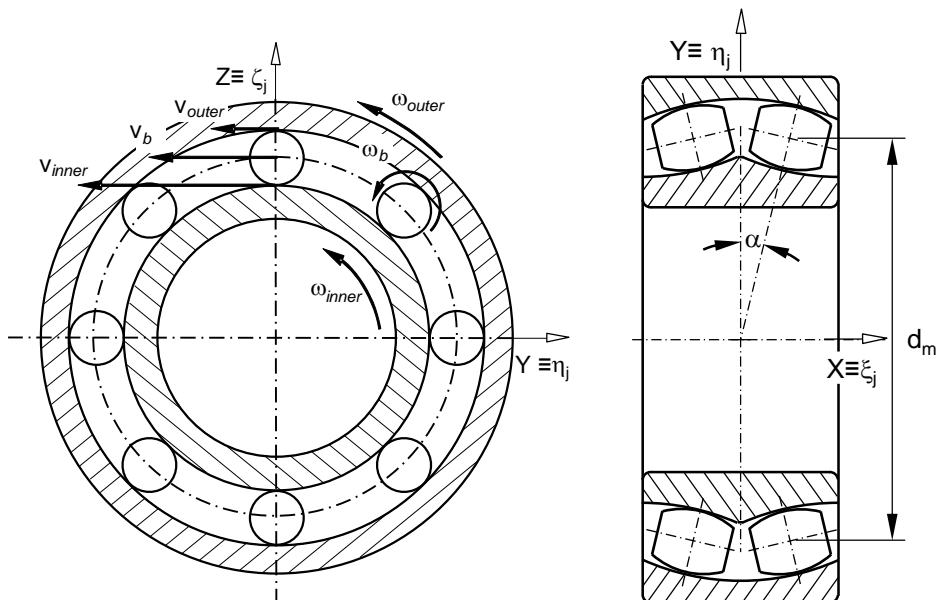
Figure 15: Angular and translation velocity of the bearing rolling elements.

17

With reference to Figure 15, it is assumed that initially there is no roller or cage slip, meaning that all components are rotating with consistent angular velocities with neglecting clearances. Based on the kinematics of the bodies and knowing that the velocity of a general point can be given as,

$$\mathbf{v}_i^P = \omega_i \mathbf{s}_i^{'P} \tag{3.7}$$

the roller velocities are calculated as functions of the inner and outer raceways angular velocities and shown as,

$$\omega_b^{'0} = \frac{\omega_{outer}^{'0} R_o - \omega_{inner}^{'0} R_i}{D_b} \tag{3.8}$$

$$v_b = -\tfrac{1}{2}\left(\omega_{inner}^{'0} R_i + \omega_{outer}^{'0} R_o\right) \tag{3.9}$$

where the angular velocities of the inner and outer raceways about their local ξ axis are shown as ω'_{inner} and ω'_{outer}. It is important to note that the variables are measures in the plane YZ, where R_i and R_o are the radius of circumferences passing by the points of contact between the rollers and the inner and outer raceways, respectively. For a spherical bearing with one row, $R_i = r_m - \tfrac{1}{2}D_b$ and $R_o = r_m + \tfrac{1}{2}D_b$. For a two row spherical roller bearing, the tilt of the rollers has to be accounted for, becoming $R_i = r_m - \tfrac{1}{2}D_b\cos\alpha$ and $R_o = r_m + \tfrac{1}{2}D_b\cos\alpha$.

The angular velocity of the cage is such that the velocity of its pockets equals, in average, the rollers velocity. Assuming that the points of contact between cage and rollers are close to the pitch radius, the angular velocity of the cage is,

$$\omega_{cage}^{'0} = -\frac{v_b}{r_m} \tag{3.10}$$

Therefore, the initial velocities of the bodies in the spherical bearing are described by,

$$\dot{\mathbf{r}}_{inner}^0 = \dot{\mathbf{r}}_{outer}^0 = \dot{\mathbf{r}}_{cage}^0 = \begin{Bmatrix} 0 \\ 0 \\ 0 \end{Bmatrix} \tag{3.11}$$

$$\boldsymbol{\omega}_{inner}^{'0} = \begin{Bmatrix} \omega_{inner}^{'0} \\ 0 \\ 0 \end{Bmatrix}; \quad \boldsymbol{\omega}_{outer}^{'0} = \begin{Bmatrix} \omega_{outer}^{'0} \\ 0 \\ 0 \end{Bmatrix} \quad \boldsymbol{\omega}_{cage}^{'0} = \begin{Bmatrix} \omega_{cage}^{'0} \\ 0 \\ 0 \end{Bmatrix} \tag{3.12}$$

$$\dot{\mathbf{r}}_b^0 = v_b \begin{Bmatrix} 0 \\ \sin\left[(b-1)\alpha_m\right] \\ -\cos\left[(b-1)\alpha_m\right] \end{Bmatrix} \quad b = 1, 2, ..., nb \tag{3.13}$$

$$\boldsymbol{\omega}_b^{'0} = \begin{Bmatrix} \omega_b^{'0} \\ 0 \\ 0 \end{Bmatrix} \quad b = 1, 2, ..., nb \tag{3.14}$$

Note that the initial conditions derived in this section ensure that the analysis starts with consistent velocities between all rolling elements and that there is no interference between the bodies at the start of the analysis. It is only during the evolution of the system that contact may develop and, eventually, sliding between elements.

18

3.2. Tapered roller bearing elements initialization

The geometric details required for the construction of the multibody model of the tapered roller bearing includes the information contained in Table 3. As in the case of spherical bearings, the data is structured equally in the case of single and double row bearings.

Roller diameter in the large end	D_l
Roller diameter in the small end	D_s
Roller lenght	L_b
Roller land lenght	L_c
Roller crown radius	R_{cr}
Roller end radius in the large end	R_{erR}
Roller end radius in the small end	R_{erL}
Outer race semi-cone angle	α_o
Inner race semi-cone angle	α_i
Outer race land lenght	l_o
Inner race land lenght	l_i
Outer race width	L_o
Inner race width	L_i
Inner race land start	e_i
Endplay	e_p
Number of rows	N_{row}
Inter race spacing	S_i

Table 3: Information required for the general dimensioning of a tapered roller bearing

The geometry of the tapered roller bearing is depicted in Figure 16 where the description of the data necessary to the geometric characterization of the bearing is presented. Based on the information contained in Table 3 it is possible to define the complete initialization of the position of the rolling elements in the roller bearing.

(a) (b) (c)
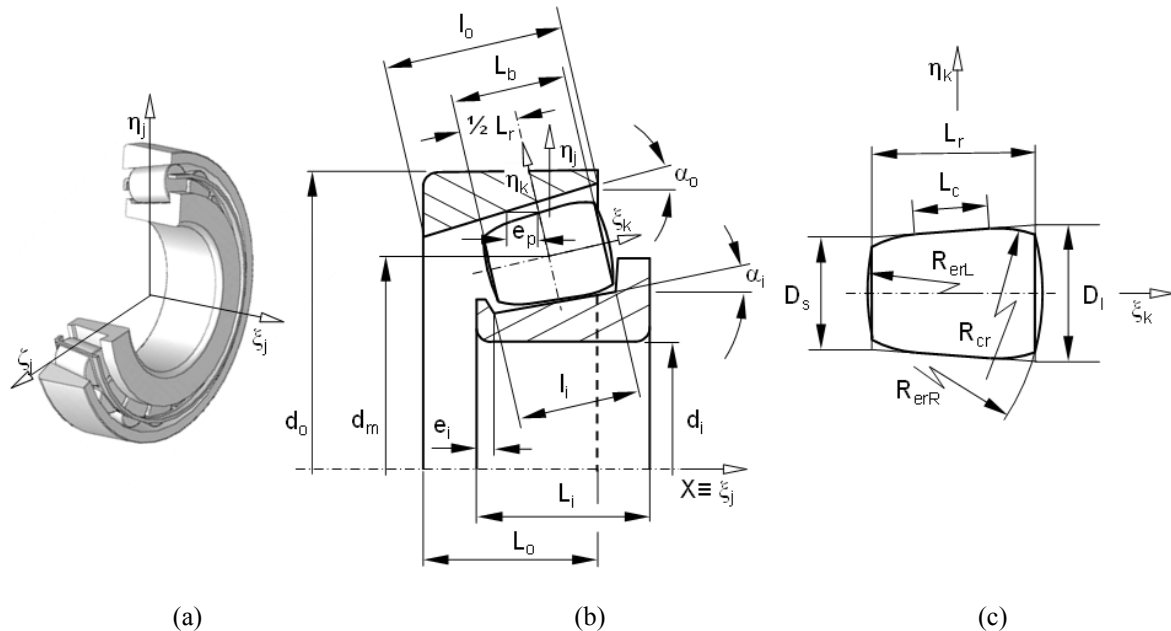
Figure 16: Geometry of the tapered bearing elements. (a) Tapered bearing representation; (b) Geometry of the cross-section of the roller bearing; (c) Geometry of the tapered roller.

The tapered roller bearing characterization generally uses a terminology different from that of other roller bearings. In particular, the outer raceway is designated by cup and the inner raceway by the

cone [35]. Here, this terminology is not used, hence inner and outer raceways are used to be similar to the terms used for spherical bearing. Another particular characteristic of the tapered bearing is that the projection lines of the raceways and of the ξ axis of each roller meet at a common point on the bearing axis to provide true rolling and low friction [36].

In order to position the rolling elements of the tapered roller bearing, with a single row of rollers, let the center of each roller be defined as the point of their ξ axis that lays on its cross-section coincident with its average diameter D_b, as depicted in Figure 17. Furthermore, it is assumed that the rollers central cross-section seats in the inner raceway halfway in the surface width l_i, seen in Figure 16. It is also assumed that the locations of the centers of mass of each raceway are coincident with their central cross-section, i.e., $L_i/2$ for the inner raceway and $L_o/2$ for the outer raceway. The pitch diameter, $d_m=2r_m$, locates the position of the rollers average radius, as seen in Figure 16 and Figure 17.
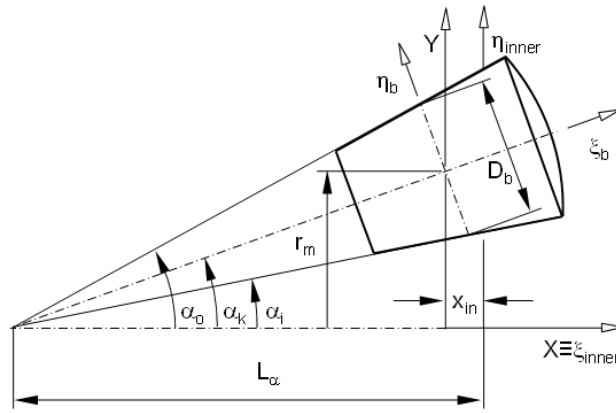
Figure 17: Basic dimensions defining the roller geometry and position.

With reference to Figure 17 let the basic dimensions of the bearing required to position the raceways and rollers at the start of the analysis be defined as,

$$D_b = \tfrac{1}{2}\left(D_s + D_l\right) \tag{3.15}$$

$$\alpha_k = \tfrac{1}{2}\left(\alpha_i + \alpha_o\right) \tag{3.16}$$

$$L_\alpha = r_m \frac{\cos\alpha_k}{\sin\alpha_k} \tag{3.17}$$

$$x_{in} = R_b \sin\alpha_k \tag{3.18}$$

in which D_b is the roller average diameter, α_k is the roller axis semi-cone angle, L_α is the position of the apex of the roller cone in the X axis, x_{in} is the position of the inner raceway η_{inner} axis with respect to Y and $R_b = \tfrac{1}{2}D_b$. The position and orientation of the inner raceway are,

$$\mathbf{r}_{inner}^0 = \left\{\begin{matrix} x_{in} \\ 0 \\ 0 \end{matrix}\right\} \tag{3.19}$$

$$\mathbf{p}_{inner}^0 = \left\{\begin{matrix} 1 \\ 0 \\ 0 \\ 0 \end{matrix}\right\} \tag{3.20}$$

The initial position and orientation of the outer raceway are obtained as,

$$\mathbf{r}_{outer}^0 = \left\{ \begin{array}{c} -\left(e_p + x_{in}\right) \\ 0 \\ 0 \end{array} \right\} \tag{3.21}$$

$$\mathbf{p}_{outer}^0 = \left\{ \begin{array}{c} 1 \\ 0 \\ 0 \\ 0 \end{array} \right\} \tag{3.22}$$

To establish the initial position and orientation of the cage it is assumed that, if guided, it is guided by the inner raceway and that its average diameter is similar, not necessarily equal, to the pitch diameter. Under these conditions the cage initial position and orientation are,

$$\mathbf{r}_{cage}^0 = \left\{ \begin{array}{c} 0 \\ 0 \\ 0 \end{array} \right\} \tag{3.23}$$

$$\mathbf{p}_{cage}^0 = \left\{ \begin{array}{c} 1 \\ 0 \\ 0 \\ 0 \end{array} \right\} \tag{3.24}$$

The position and orientation of the rollers in the tapered roller bearing follows the same procedure used for the spherical rollers, and depicted by Figure 14, except for the orientation of the rollers, which follows the same procedure as for the orientation of the rollers in a two row spherical bearing, detailed in Appendix B – Two Row Spherical Bearing Initializations. Therefore these initial positions and orientations are rewritten here as,

$$\mathbf{r}_b^0 = r_m \left\{ \begin{array}{c} 0 \\ \cos\left[(b-1)\alpha_m\right] \\ \sin\left[(b-1)\alpha_m\right] \end{array} \right\} \qquad b = 1,2,...,nb \tag{3.25}$$

$$\mathbf{p}_b^0 = \left\{ \begin{array}{c} \cos\dfrac{\alpha_k}{2} \\ 0 \\ -\sin\dfrac{\alpha_k}{2}\sin\left[(b-1)\alpha_m\right] \\ \sin\dfrac{\alpha_k}{2}\cos\left[(b-1)\alpha_m\right] \end{array} \right\} \qquad b = 1,2,...,nb \tag{3.26}$$

Another particular characteristic of the tapered bearing is that it can be mounted with endplay or with some preloading. Tapered bearings are more commonly assembled in pairs, i.e., as double row bearings, as shown in Figure 18. In this case they can be mounted back to back, also known as double cup assembly, or face to face, alternatively defined as double cone assemblies [37]. For double row tapered roller bearings the initial position and orientation of the bodies are presented in Appendix C – Two Row Tapered Bearing Initializations.

21
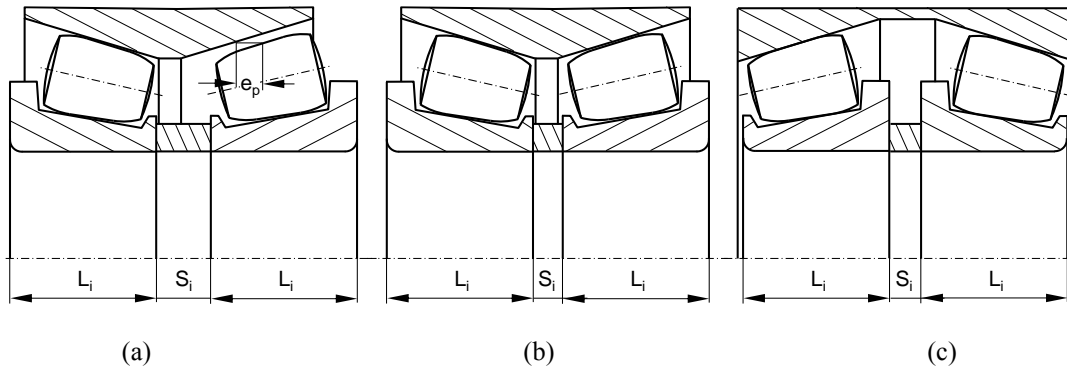
Figure 18: Tapered roller bearing with two rows: (a) Back to back (double cup assembly) mounting with play; (b) Back to back (double cup assembly) mounting with preloading; (c) Front to front (double cone assembly) mounting.

The initialization of the tapered roller bearings requires that the initial velocities of all rolling elements are defined. The initial velocities for this type of bearing are directly analogous to those of the spherical bearing, by Equations (3.11) to (3.14), with the difference that the tilt angle from the spherical bearings, α, is here replaced by the semi-cone angle of the tapered roller, α_k.

3.3. Model identification

When constructing the computational tool, the requirement for a realistic identification of the bearing geometric characteristics, to be given as input, is of fundamental importance. Even though some roller bearing manufacturers offer several catalogues with different roller bearing dimensions and characteristics, the necessary data required for the construction of the multibody models detailed in sections 3.1 and 3.2, is not publicly available. The acquisition of the necessary information to fulfil the input data tables relative to spherical and roller bearings, was achieved by the tribology group at FEUP, also partner in the MAXBE project. Since the partners from University of Porto were responsible for laboratory testing, to measure the properties of lubricants used with also spherical and tapered roller bearings, bearing prototypes were available. The geometric data was obtained by using a Surface Roughness Tester, available to the identification of geometries and roughness with maximum definition. For the largest dimensions, such as some raceway and cage dimensions, a calliper rule was used. It is important to notice that, since the roller bearings were already used in railway applications, some parts used for measurements had imperfections and signs of wear. This feature eventually led to dimensional deviations from that of new roller bearings. However, since the data requested to manufacturers was not made available for new bearings, the acquired dimensional features constitute the best approach.

The geometric data, acquired experimentally, was further post-processed for consistency. Among other geometric features it was noticed that the values obtained from the physical measurements for the raceway angles α_0 and α_i of the tapered bearing were not adequate since it is required that both are centered at the same point. For this reason, the raceway angles were calculated analytically based on the measured geometry of the roller, by knowing the internal angle formed by its sides. The resulting data for both spherical and tapered bearing models, obtained by physical testing, is presented in Appendix A - Input Data for Bearing Model.

22

4. GENERAL FORMULATION OF THE ROLLER CONTACT DETECTION

The formulation of the contact between the bearing rollers and the raceway and cage is structured as a two stage problem. In the first stage the positions and geometries of the roller, raceways and cage are evaluated to identify the points of proximity and the eventual existence of contact. The second stage consists in the evaluation of the contact forces that develop between the surfaces in actual contact and in the calculation of the friction and other shear forces that develop, eventually involving lubrication. In the first evaluation stage only the kinematics of the bearing mechanical components and their geometry play a role while in the second stage the constitutive equations, relating the interference between components with contact forces, are used. The evaluation of the forces that act over each mechanical element of the bearing sets the ground for the formulation of the equilibrium equations of each body, which have to be solved, being the resulting accelerations integrated afterwards. Here the only focus is on the calculation of the forces that act over each component of the bearing. In this chapter the first stage i.e., the contact detection, is described by detailing the necessary equations and procedures to be followed to evaluate the existence of contact.

4.1. Roller bearing contacts

When observing a functioning roller bearing it is visible that over time several different contacts develop over each of its bodies. In order to create a realistic model of a roller bearing, all of these contacts should be considered, otherwise the behaviour of the bearing becomes inaccurate. The most important roller contacts, in any type of roller bearing, take place between each roller side and the raceway or flange surfaces and between rollers and cage pockets. Other areas of contact can also be found in a roller bearing, depending on its geometry and characteristics, such as contact between the back parts of each cage, when the bearing has two separate cages, between the cage guidance and raceways or even between a ring and the back of each inner or outer raceways, in the case where the bearing has two rows with one of its raceways divided in two and spaced by a ring that fills the inter race spacing. Particular cases of breakage of the cage can also be considered, where contact between rollers can occur. In this work, these other contacts are not considered, since they are likely to happen only in exceptional occasions and in the event of defects or failure. Therefore, in this work, only the most common and important roller contacts are considered, reason why contact is studied only between the rollers and each of the bodies directly surrounding them and not between rollers or between cage and raceways.

The contacts considered in this work, illustrated as in Figure 19, are mainly listed as:

- Contact between roller and raceways;
  - Contact between roller and inner raceway (Inner);
  - Contact between roller and outer raceway (Outer);
- Contact between roller and flanges;
  - Contact between roller and right flange (FR);
  - Contact between roller and left flange (FL);

- Contact between roller and cage;
  - o Contact between roller and cage pocket tops ($C_{2.1}$, $C_{2.2}$, $C_{4.1}$, $C_{4.2}$);
  - o Contact between roller and cage pocket sides ($C_{3.1}$, $C_{3.2}$).

(a)   (b)
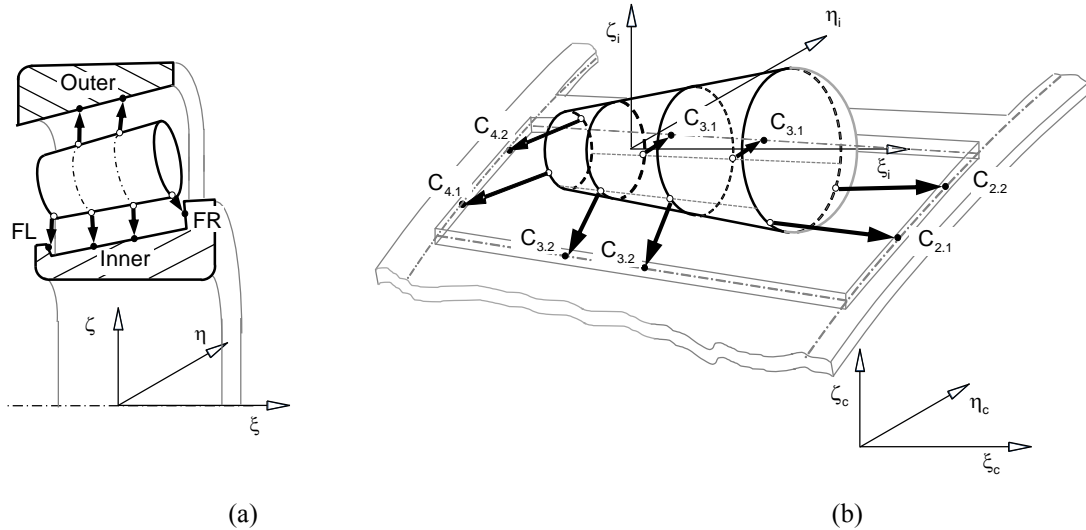
Figure 19: Contacts considered on the roller bearing. (a) Contacts on roller with raceways and flanges; (b) Contacts between roller and cage.

4.2. Contact search

When evaluating existence of contact, it is necessary to study every pair of contact points individually, since the value of force developed in each point can be different depending on the geometry and kinematics of the body. Also, the mechanical system is studied over time and these points can, and usually do, develop in different positions. With this in mind, every contact point has a persistent method which is solved to calculate its position in each body. This method consists in finding the two closest points between each body in a certain area where contact is prone to develop and identifying the pseudo-interference, or local deformation, between the contacting surfaces.

4.2.1. Search of contact between two generic surfaces

Let it be assumed that a body in motion approaches another. These bodies can be described as generic surfaces, which can be numerically represented, as shown in Figure 20. When these bodies are in motion, there are always two points which are closest to each other and where contact is more likely to occur when their trajectory leads them to approach enough. Over time the position of each point may change, but its local position for any instance can be evaluated when the geometry of each surface is known. The search for contact between the two surfaces requires the identification of two parameters of each surface, associated to the location of the points that are either in contact or in closer proximity. This is illustrated in Figure 20, in which the points in closer proximity are depicted as P and Q, each belonging to a generic surface on body i and j, respectively. Furthermore, the surfaces are defined in the referentials $(\xi\eta\zeta)_i$ and $(\xi\eta\zeta)_j$ fixed to the centres of mass of bodies i and j, respectively. Vector $\mathbf{d}$ represents the distance between them, given by $\mathbf{d} = \mathbf{r}_P - \mathbf{r}_Q$.
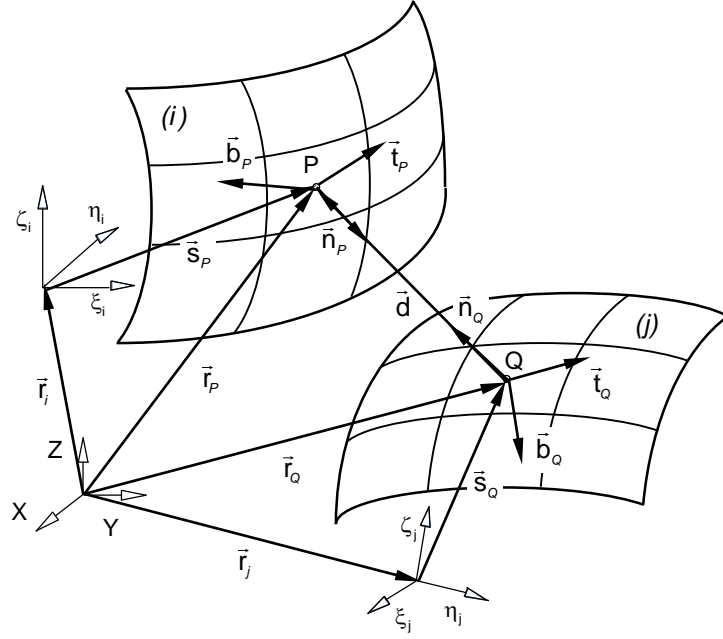
Figure 20: Candidates to contact points between two parametric surfaces. Point *P* belongs to a surface on body *i* and point *Q* to a surface on body *j*.

With reference to Figure 20, the position of point *P* on body *i* is defined by the sum of vectors $\mathbf{r}_i$, which is the position of the roller center of mass with respect to the inertial frame (XYZ), and vector $\mathbf{s}_P$ representing the position of point *P* with respect to the body *i* fixed frame. The position of point *Q* is analogous to point *P*. Points *P* and *Q* positions can be written as,

$$\begin{aligned}\mathbf{r}_P &= \mathbf{r}_i + \mathbf{A}_i\mathbf{s'}_P \\ \mathbf{r}_Q &= \mathbf{r}_j + \mathbf{A}_j\mathbf{s'}_Q\end{aligned}$$

(4.1)

where $\mathbf{A}_i$ and $\mathbf{A}_j$ are the transformation matrices from the local referential attached to bodies *i* and *j*, respectively. The coordinates of points *P* and *Q*, expressed in body *i* and *j* reference frames and defined as $\mathbf{s}'_P$ and $\mathbf{s}'_Q$, respectively, depend on the parametric description of each surface, reason why such procedures are described individually in further topics.

Still with reference to Figure 20, on point *P* in body *i* the vector normal to the surface is $\mathbf{n}_P$ while $\mathbf{t}_P$ and $\mathbf{b}_P$ are the tangent and binormal vectors to the surface, respectively, forming an orthogonal basis. The same theory applies to $\mathbf{n}_Q$, $\mathbf{t}_Q$ and $\mathbf{b}_Q$, which are the vectors on point *Q*. The relation between the components of the different vectors defined in each body and the parameters used to define the surface depends on the specific geometry of the contacting surface. Such relations are also developed in detail in forthcoming sections. At this point, it is assumed that these expressions exist in close forms.

The conditions for minimal distance between the two surfaces are that points *P* and *Q* are generically described by,

$$\begin{cases}\mathbf{d}^T\,\mathbf{t}_Q = 0 \\ \mathbf{d}^T\,\mathbf{b}_Q = 0\end{cases} \quad ; \quad \begin{cases}\mathbf{d}^T\,\mathbf{t}_P = 0 \\ \mathbf{d}^T\,\mathbf{b}_P = 0\end{cases}$$

(4.2)

which means that not only the normal to each surface must be collinear with the vector that connects the two points in closer proximity but also perpendicular to the tangent and binormal vectors on each point. Effective contact occurs if, besides the fulfilment of Eq.(4.2), penetration also exists, which is expressed by,

$$\delta = \mathbf{d}^T \ \mathbf{n}_Q \leq 0 \tag{4.3}$$

otherwise, the points are of close proximity, but not in contact.

4.2.2. Search of contact between circle and surface

When applying the procedure outlined in Section 4.2.1 to the case of a roller approaching a generic surface, as represented in Figure 21(a), let it be assumed that in the course of its motion the roller actually contacts the surface. The situation is numerically perceived as contact and is illustrated in Figure 21(b), being the shaded volume a representation of the penetration of the roller in the surface, i.e., the interference between the two bodies. Note that in penalty contact force models, foreseen for application in this work, the contact force is related with the quantification of the interference, designated hereafter as penetration.

(a)   (b)
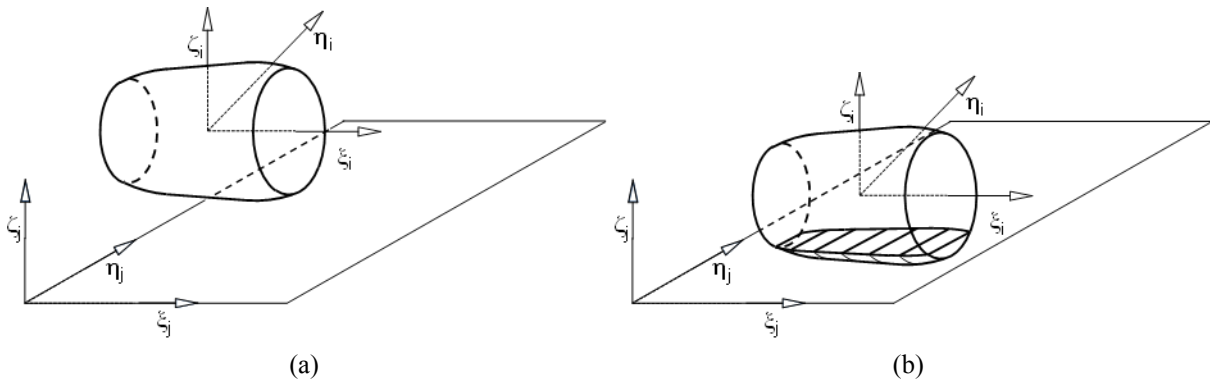
Figure 21: Contact between a roller and a surface. (a) Approach phase in which the minimum distance is calculated; (b) Contact phase in which the actual penetration, shaded volume, is evaluated.

The shape of the rollers in standard bearings is not perfectly cylindrical or conical, in the case of tapered rollers. They also include a crowned region and a corner radius in order to avoid edge loading, thus reducing fatigue on the contacting elements. Furthermore, the geometry of the surfaces of the raceways may not be cylindrical or conical and/or the axis of the rollers may be misaligned with the axis of the raceways resulting in skewing between the two rolling elements. Any of the conditions mentioned lead to a penetration depth between the roller and the contacting surface that varies along the roller axis. Consequently, instead of defining a common penetration depth for the complete roller, the penetration can only be defined for each particular cross-section of the roller.

Let a roller with the shape represented in Figure 22(a) represent any generic roller, i.e., cylindrical, spherical, toroidal, tapered or spherical tapered roller. Consider now that the roller is divided in a user defined N_{sl} number of strips, i.e., cylindrical segments, which act as rigid bodies without any relative motion between them, as perceived in Figure 22(b). Now the contact problem of the complete roller can be described as N_{sl} independent contact problems of thin cylinders, being one of those

highlighted in Figure 22(c), in which the contacting penetration depth is constant throughout the slice, or strip [38]. Therefore, each one of the contact problems, required to represent the roller to surface contact, is described by the contact of the central cross-section of the slice, as represented in Figure 23.

(a)   (b)   (c)
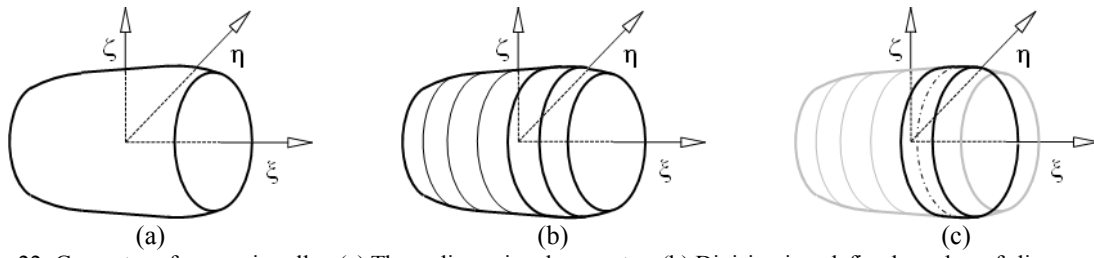
Figure 22: Geometry of a generic roller. (a) Three-dimensional geometry; (b) Division in a defined number of slices, or strips; (c) Individual strip with the representation of its central cross-section.

(a)   (b)
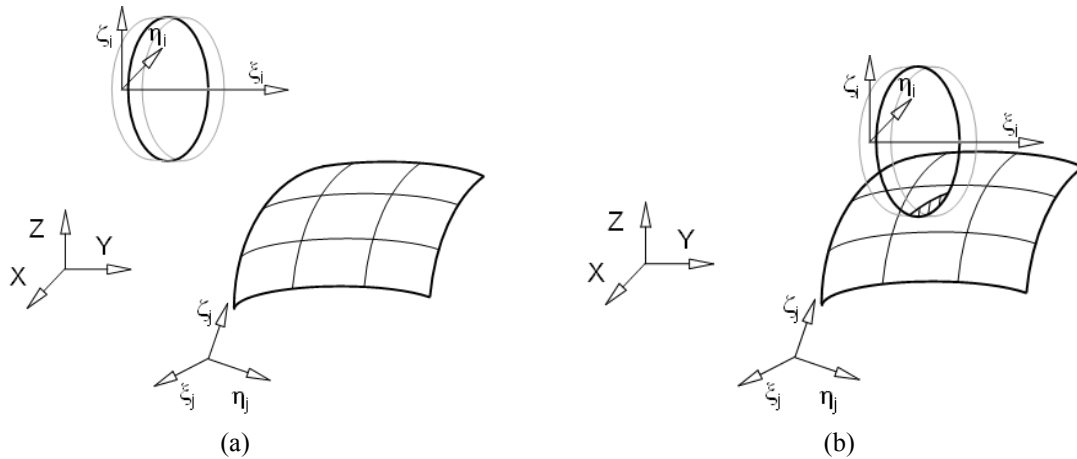
Figure 23: Interaction between a circle and a surface. (a) Approach between the geometric figures; (b) Contact with the interference represented as a shaded area.

As a result of the approach followed here, the search for contact of the rollers with any potential contacting surface is reduced to the identification of the minimum distance between the central cross-section of each slice and the surface. By identifying the proper interaction conditions it is possible to verify if such distance corresponds to separation or to effective contact. In what follows the central cross-section of the slice is designated by circular cross-section or simply by circle. The representation of the two contacting points between a circle of the roller and a surface can be seen in Figure 24.
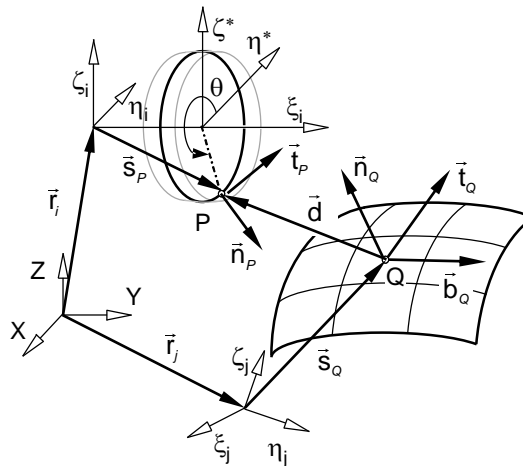
Figure 24: Geometric relations between a point P in a circumference and a point Q in a generic surface.

Due to the fact that only one parameter is required to define a circle, one of the required parameters used in Eq. (4.2) to find the point of contact on the roller is now a constant. So, only one parameter is needed to identify the point of contact on the roller circle and two parameters continue to be required for the surface. This results in one of the equations of Eq. (4.2) to be no longer needed, so the conditions for minimal distance between the circle and a surface are now described by,

$$\begin{cases} \mathbf{d}^T \ \mathbf{t}_P = 0 \\ \mathbf{d}^T \ \mathbf{t}_Q = 0 \\ \mathbf{d}^T \ \mathbf{b}_Q = 0 \end{cases} \tag{4.4}$$

Effective contact occurs between the circle and the surface if both Eq. (4.4) and Eq. (4.3) are fulfilled.

4.2.3. Search of contact between circle and line

In some cases of contact in a roller bearing, such as the contact between a roller and one of the cage's pocket tops for example, the surface that the roller contacts has a small height-length ratio, meaning that the surface can be approximated to a line in order to simplify the contact detection. The representation of the two contacting points between a circle of the roller and a line can be seen in Figure 25.
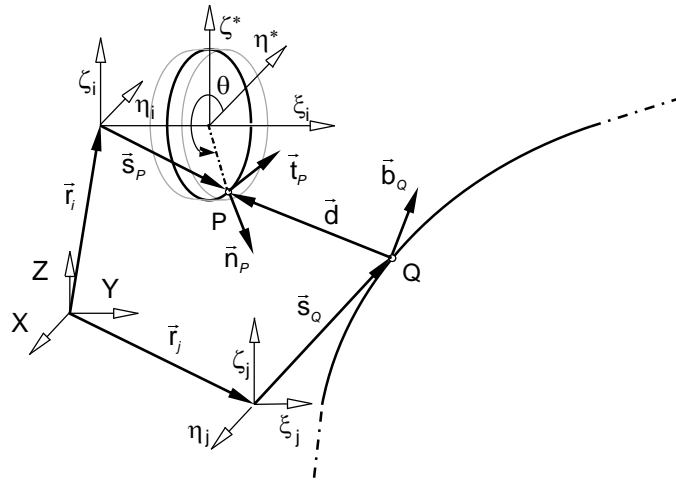
Figure 25: Geometric relations between a point *P* in a circumference and a point *Q* in a generic line.

The number of parameters that need to be identified decreases to two: one parameter for the point on the circle and other for the point on the line. In this case, the equations to be fulfilled in order to find the closest points for contact are given as,

$$\begin{cases} \mathbf{d}^T \ \mathbf{b}_Q = 0 \\ \mathbf{d}^T \ \mathbf{t}_P = 0 \end{cases} \tag{4.5}$$

Effective contact occurs between the circle and the line if both Eq. (4.5) and Eq. (4.3) are satisfied.

4.3. Roller contacts

The contact point on a roller, for each pair of contacting points considered in this work, enumerated in Section 4.1, always belongs to a circumference representing the central cross-section of a slice. The point on the roller is indicated as point *P*, whose position in the inertial frame (XYZ) is already expressed

in Eq. (4.1). Since point *P* always belongs to a circumference, the description of the surface is simplified to the description of a circumference, so the point only depends on one parameter to be described. In this case, the parameter is an angle, defined as θ. With reference to Figure 24 and Figure 25, the coordinates of point *P,* belonging to the circumference, and the normal and tangent vectors to the circle, are expressed in the body *i* reference frame as,

$$\mathbf{s}'_P = \begin{Bmatrix} \xi_P \\ R_s \cos\theta \\ R_s \sin\theta \end{Bmatrix} \;; \; \mathbf{n}'_P = \begin{Bmatrix} 0 \\ \cos\theta \\ \sin\theta \end{Bmatrix} \;; \; \mathbf{t}'_P = \begin{Bmatrix} 0 \\ -\sin\theta \\ \cos\theta \end{Bmatrix} \tag{4.6}$$

in which angle θ is measured in a plane $(\xi\eta)^*$ parallel to plane $(\xi\eta)$, R_s is the radius of the circumference and ξ_P is the circumference's ξ coordinate. It should be noted that the relation between the body fixed and inertial coordinates of the vectors that define the tangent to the contact surfaces is written as,

$$\begin{aligned} \mathbf{n}_P &= \mathbf{A}_i \mathbf{n}'_P \\ \mathbf{t}_P &= \mathbf{A}_i \mathbf{t}'_P \\ \mathbf{b}_P &= \mathbf{A}_i \mathbf{b}'_P \end{aligned} \tag{4.7}$$

The transformation matrix $\mathbf{A}_i$ is that of the body in which the geometrical feature, circle, is defined.

4.4. Surface contacts

All contacts between each slice of the roller and the raceways or with the flanges are approached as contacts between a circle and a surface, as presented in Section 4.2.2. In this section, the necessary vectors are defined for each surface to be used in Eq. (4.4) to calculate the points of closer proximity. This means that the position of the surface points, $\mathbf{r}_Q$, and the normal, tangential and binormal vectors, $\mathbf{n}_Q$, $\mathbf{t}_Q$ and $\mathbf{b}_Q$, to the contacting point of the surface, for the surfaces encountered in typical raceways and flanges of roller bearings, are identified here.

All bearing raceways are surfaces of revolution, i.e., they are obtained by sweeping a plane line about an axis of revolution, as illustrated in Figure 26. Therefore, the coordinates of any point in the surface can be expressed in terms of the parameters that define the planar line and the sweep angle. For instance, in Figure 26 the line is described as a function of ξ_j, defined as $R(\xi_j)$ and the sweep angle is θ_2.
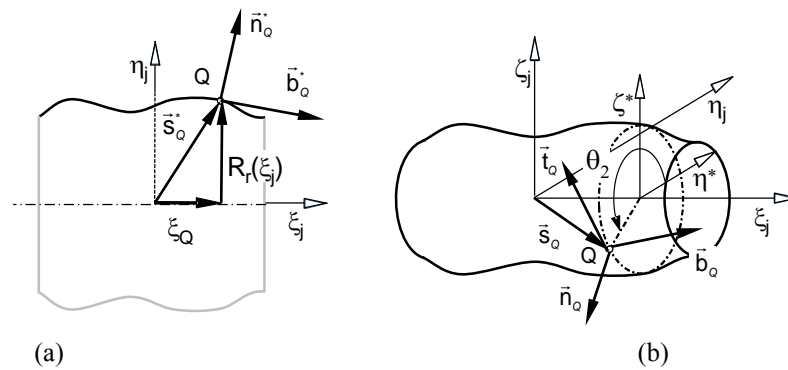
Figure 26: Axisymmetric surface obtained as the sweep of a line about an axis: (a) Parametric representation of the line and its tangential and normal vectors in point *Q*; (b) Surface of revolution, with the sweep angle θ_2 and the surface defining vectors at point *Q*.

In the $(\xi\eta)_j$ plane the position of point Q is a function of a single parameter, which in the case illustrated in Figure 26 is the coordinate ξ_Q, and is written as,

$$\mathbf{s}^*_Q = \left\{ \begin{array}{c} \xi_Q \\ R(\xi_Q) \\ 0 \end{array} \right\} \tag{4.8}$$

The normal and tangent vectors to point Q in the line, shown in Figure 26(a), have components that are also functions of the parameter defining the line. These vectors are expressed as,

$$\mathbf{n}^*_Q = \left\{ \begin{array}{c} n^*_{\xi_Q}(\xi_Q) \\ n^*_{\eta_Q}(\xi_Q) \\ 0 \end{array} \right\} \quad ; \quad \mathbf{b}^*_Q = \left\{ \begin{array}{c} b^*_{\xi_Q}(\xi_Q) \\ b^*_{\eta_Q}(\xi_Q) \\ 0 \end{array} \right\} \tag{4.9}$$

The surface of revolution is obtained by sweeping the line around the axis of revolution, i.e., around ξ_j. This operation can be represented as a transformation of coordinates in which any point on the line, with coordinates given by Eq.(4.8), and any vector associated to such point, such as the normal and binormal vectors described in Eq.(4.9), are rotated as,

$$\begin{aligned} \mathbf{s}'_Q &= \mathbf{A}_{\theta_2} \mathbf{s}^*_Q \\ \mathbf{n}'_Q &= \mathbf{A}_{\theta_2} \mathbf{n}^*_Q \\ \mathbf{b}'_Q &= \mathbf{A}_{\theta_2} \mathbf{b}^*_Q \end{aligned} \tag{4.10}$$

in which the rotation matrix $\mathbf{A}_{\theta 2}$ is obtained by,

$$\mathbf{A}_{\theta_2} = \begin{bmatrix} 1 & 0 & 0 \\ 0 & \cos\theta_2 & -\sin\theta_2 \\ 0 & \sin\theta_2 & \cos\theta_2 \end{bmatrix} \tag{4.11}$$

By substituting Eqs.(4.8), (4.9) and (4.11) into Eq.(4.10), and rearranging, the components of the position, normal and tangent vector to the surface, in point Q, are,

$$\mathbf{s}'_Q = \left\{ \begin{array}{c} \xi_Q \\ R\cos\theta_2 \\ R\sin\theta_2 \end{array} \right\} \; ; \; \mathbf{n}'_Q = \left\{ \begin{array}{c} n^*_{\xi_Q} \\ n^*_{\eta_Q}\cos\theta_2 \\ n^*_{\eta_Q}\sin\theta_2 \end{array} \right\} \; ; \; \mathbf{b}'_Q = \left\{ \begin{array}{c} b^*_{\xi_Q} \\ b^*_{\eta_Q}\cos\theta_2 \\ b^*_{\eta_Q}\sin\theta_2 \end{array} \right\} \; ; \; \mathbf{t}'_Q = \left\{ \begin{array}{c} 0 \\ -\sin\theta_2 \\ \cos\theta_2 \end{array} \right\} \tag{4.12}$$

in which $R=R(\xi_Q)$ and the components of $\mathbf{n}^*_Q = \mathbf{n}^*_Q(\xi_Q)$ and $\mathbf{b}^*_Q = \mathbf{b}^*_Q(\xi_Q)$ continue to be function of the parameter defining the sweep line, generically defined as ξ_Q.

The relation between the body fixed and inertial coordinates of the vectors that define the normal and binormal to the contact surfaces is written as,

$$\begin{aligned} \mathbf{n}_Q &= \mathbf{A}_j \mathbf{n}'_Q \\ \mathbf{b}_Q &= \mathbf{A}_j \mathbf{b}'_Q \end{aligned} \tag{4.13}$$

The tangent to the surface on point Q, $\mathbf{t}_Q$, is perpendicular to both $\mathbf{n}_Q$ and $\mathbf{b}_Q$, and is calculated by the cross product between both vectors. The problem is now reduced to finding the parametric definitions of the lines that define the contour of the raceways in spherical and tapered bearings.

4.4.1. Raceway contacts

4.4.1.1.   Tapered bearing raceway contact

Raceways of tapered bearings are, typically, conical geometries with which the rollers contact, as implied in Figure 27. In the inner raceway the contact takes place with an external conical surface while for the outer raceway the contact is with an internal conical surface.
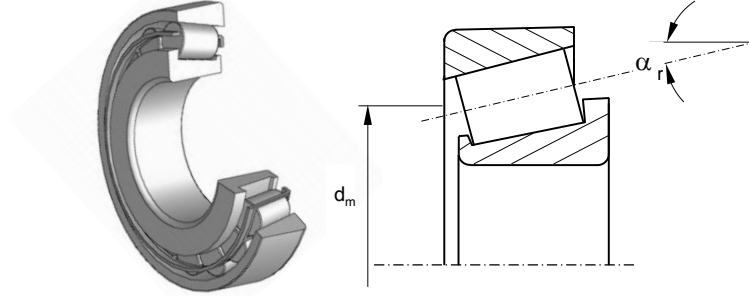
Figure 27: Typical tapered roller bearing with a highlighted cross section (note that the details of the roller geometry, namely its crowning and the end radius, as well as the flanges of the raceways are not detailed).

As in Figure 28(a), the η coordinate of point Q in the sweep line is related with the apex position L_α and α_r is the raceway angle. The η coordinate of a point in the sweep line is a function of ξ_j given by,

$$R_r = \left(L_\alpha + \xi_j\right)tg\,\alpha_r \tag{4.14}$$

At point Q, the position of a point in the sweep line that defines the contact cross-section of the conical surface and the normal and tangent vectors, in the body fixed coordinate system, are written as,

$$\mathbf{s}_Q^* = \left\{\begin{array}{c} \xi_j \\ \left(L_\alpha + \xi_j\right)tg\,\alpha_r \\ 0 \end{array}\right\} \ ; \ \mathbf{n}_Q^* = \left\{\begin{array}{c} -\sin\alpha_r \\ \cos\alpha_r \\ 0 \end{array}\right\} \ ; \ \mathbf{b}_Q^* = \left\{\begin{array}{c} \cos\alpha_r \\ \sin\alpha_r \\ 0 \end{array}\right\} \tag{4.15}$$

The definition of the normal vector is for the inner raceway, named as cone in standard bearing terminology. For the outer raceway, defined as cup, the contact is interior to the conical surface and the negative of the normal vector must be used. No limits are defined here for the axial coordinate of the bearing not only because tapered bearings are usually mounted in pairs but also because, depending in specific designs, one or more of the raceways have flanges that limit the relative travel of the rollers.

(a)   (b)   (c)
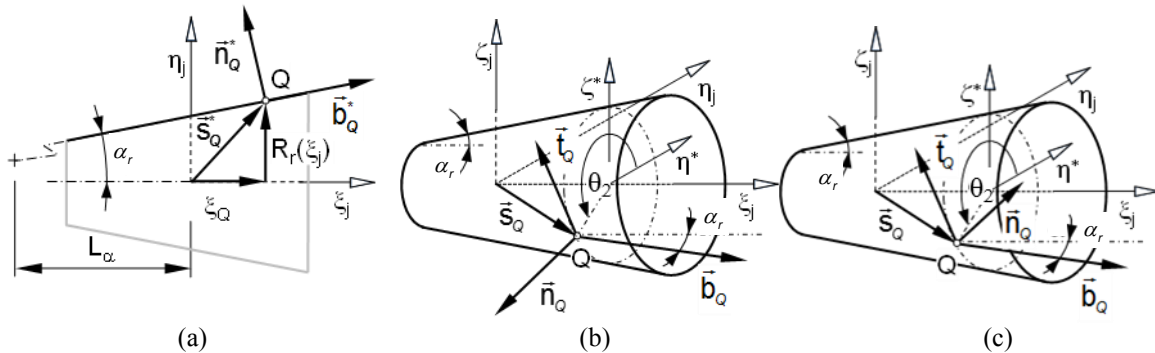
Figure 28: Contact point Q and surface normal and tangent vectors in a conical surface for: (a) Contact point in the body fixed $\xi\eta$ plane; (b) External contact, as in the inner raceway; (c) Internal contact, as in the outer raceway.

4.4.1.2. Spherical bearing raceway contact

Raceways of spherical bearings are, typically, toroidal geometries which the rollers contact, as implied in Figure 29. In the inner raceway the contact takes place with an external inverted toroidal surface while for the outer one the contact is with an internal toroidal surface.
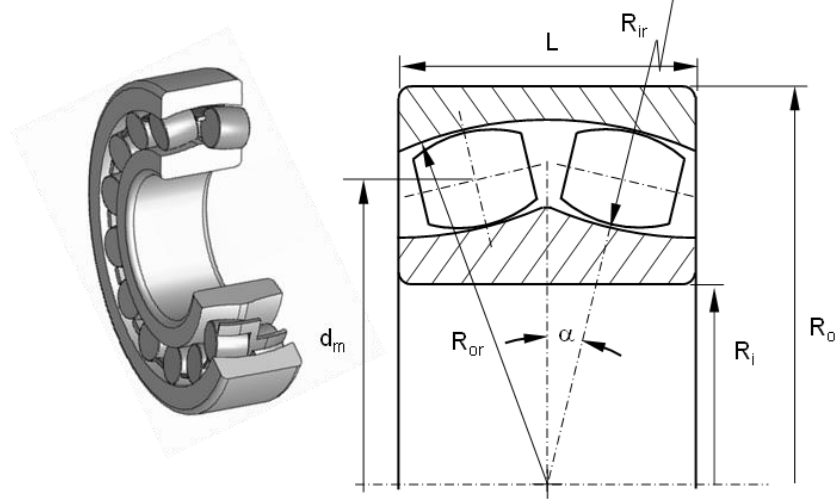
Figure 29: Typical spherical roller bearing with a highlighted cross section (note that the details of the roller geometry, namely its end radius and the flanges of the raceways, are not detailed).

Most of the spherical bearings have two rows of rollers with the inner raceway geometry a more complex geometric description than the outer raceway geometry. As a result the description of the sweep line for the outer raceway is different from that used for the inner raceway. With reference to Figure 30(a), the coordinates of the center of the arc of circumference that defines the left side of the inner raceway is,

$$\mathbf{s}'_O = \left[R_{ir} + R_{or} - 2\left(R_b + t_c \right) \right] \begin{Bmatrix} -\sin\alpha \\ \cos\alpha \\ 0 \end{Bmatrix} \tag{4.16}$$

where the inner and outer raceway radius are depicted by R_{ir} and R_{or}, respectively, R_b is the roller radius and t_c the clearance between the roller and raceway. Angle α is defined in Figure 29. The position of any point in the sweep line of the left inner raceway is obtained as a function of an angle ϕ about the ζ_j axis, as shown in Figure 30.

$$\mathbf{s}^*_Q = \mathbf{s}'_O + R_{ir} \begin{Bmatrix} \sin\phi \\ -\cos\phi \\ 0 \end{Bmatrix} \tag{4.17}$$

The normal and tangent vectors to the sweep line, at point Q, in the body fixed coordinate system, are written as,

$$\mathbf{n}^*_Q = \begin{Bmatrix} -\sin\phi \\ \cos\phi \\ 0 \end{Bmatrix} \quad ; \quad \mathbf{b}^*_Q = \begin{Bmatrix} \cos\phi \\ \sin\phi \\ 0 \end{Bmatrix} \tag{4.18}$$

For the right side of the inner raceway, of a double row spherical bearing, according to Figure 30(b), the position of the center of the sweep line is,

$$\mathbf{s}'_O = \left[R_{ir} + R_{or} - 2\left(R_b + t_c \right) \right] \begin{Bmatrix} \sin\alpha \\ \cos\alpha \\ 0 \end{Bmatrix} \qquad (4.19)$$

With reference to Figure 30(b), the position of any point in the sweep circle and the coordinates of the normal and tangent vectors are written as,

$$\mathbf{s}^*_Q = \mathbf{s}'_O + R_{ir} \begin{Bmatrix} -\sin\phi \\ -\cos\phi \\ 0 \end{Bmatrix} \quad ; \quad \mathbf{n}^*_Q = \begin{Bmatrix} \sin\phi \\ \cos\phi \\ 0 \end{Bmatrix} \quad ; \quad \mathbf{b}^*_Q = \begin{Bmatrix} \cos\phi \\ -\sin\phi \\ 0 \end{Bmatrix} \qquad (4.20)$$

in which angle ϕ, for the right side of the inner raceway is taken as positive when measured as in Figure 30(b).

The outer raceway sweeping curve is an arc of circle with a radius R_{or} centered in the negative η_j axis, as depicted by Figure 31(a). The roller contact takes place in the interior of the surface of revolution resulting from the revolution of the arc circle about the ξ_j axis.

(a)   (b)   (c)
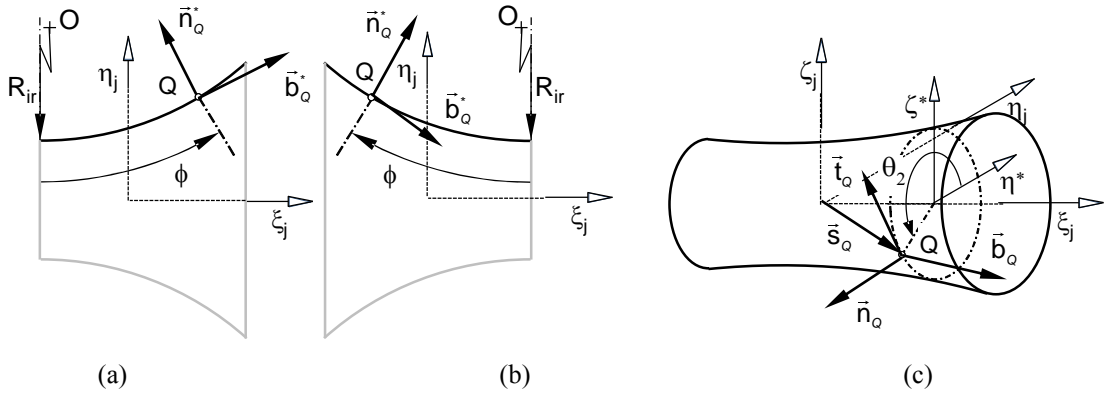
Figure 30: Geometry of an inner raceway of a spherical roller bearing: (a) Contact point in the body fixed $\xi\eta$ plane in the left side; (b) Contact point in the body fixed $\xi\eta$ plane in the right side; (c) Spatial representation.

(a)   (b)
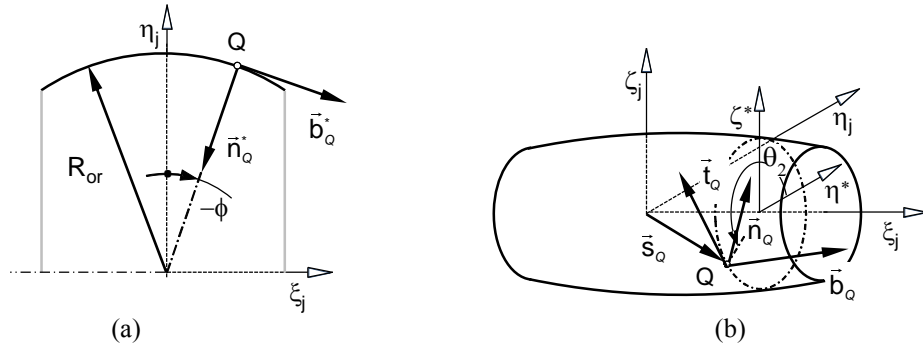
Figure 31: Geometry of an outer raceway of a spherical roller bearing: (a) Contact point in the body fixed $\xi\eta$ plane; (b) Contact point and surface vectors in the inner raceway.

Still with reference to Figure 31, the arc of circle that constitutes the sweep line of the outer raceway is centered in the origin of the body fixed coordinate frame, which in turn seats in the axis or rotation of the raceway. Using the angle ϕ, positive in the counter-clockwise direction, the position of a point Q in the arc of circle and the coordinates of the normal and tangent vectors are,

$$\mathbf{s}^*_Q = \begin{Bmatrix} -R_{or}\sin\phi \\ R_{or}\cos\phi \\ 0 \end{Bmatrix} \quad ; \quad \mathbf{n}^*_Q = \begin{Bmatrix} \sin\phi \\ -\cos\phi \\ 0 \end{Bmatrix} \quad ; \quad \mathbf{b}^*_Q = \begin{Bmatrix} \cos\phi \\ \sin\phi \\ 0 \end{Bmatrix} \qquad (4.21)$$

The position of point Q with respect to the body fixed coordinate frame and the normal, tangent and binormal vectors associated to the surface tangent to the point are depicted in Figure 31(b).

4.4.2. Flange contacts

In bearings the normal dynamics of the rollers leads to occasional contacts between the roller tops and the flanges that limit the land length of the roller. Due to the roller end diameters, in the case of the small end of a tapered roller, the contact with the flange is achieved with the circular landmark that limits the roller, as seen in Figure 32(a). Due to its spherical shape, at least the large end but eventually the small end also, in the case of the tapered roller the contact with the flange is between a spherical surface and a conical solid, as depicted by Figure 32(b). However, since the radius of the spherical surface is of such a high value (larger than 1 meter), the geometry of the large top of the roller is considered flat. The curvature of the surface is neglected and the contact search between the large top and the flange, as well as with the top of the cage, is achieved by considering the large top of the roller as a circle, just as the small top. The contact with flanges on a spherical roller bearing follows the same procedure as described here.

(a)   (b)
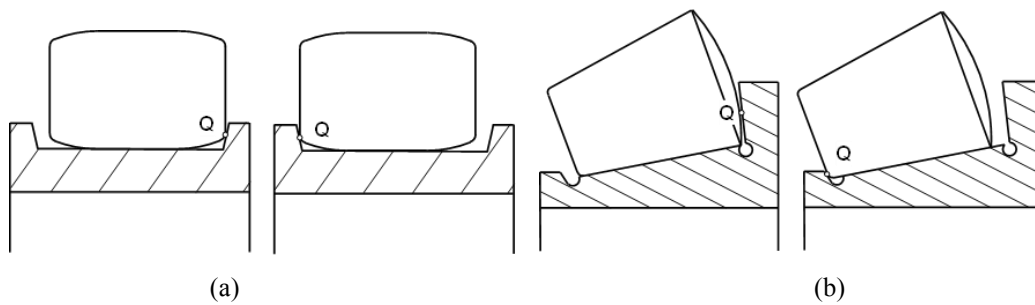
Figure 32: Contact geometry between rollers and flanges. Point Q refers to the contact point for a tapered roller.

The detailed geometry of the tapered roller bearing inner raceways, with flanges, is represented in Figure 33. The raceway land geometry is provided by the user, together with the flange angles and heights, while all other features are obtained from the rollers and general bearing user data. Note that in the case of tapered roller bearings the outer raceways have no flanges. However, in the case of any particular bearing design, for which flanges in the outer races would be used, their geometric definition would follow the basic steps outlined in what follows, with the corresponding adjustments.
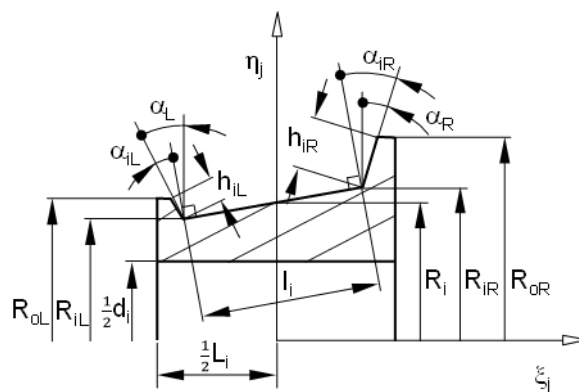
Figure 33: Detailed geometry of the flanges for tapered roller bearings inner raceway

The flanges contact surface results from sweeping a line segment about the axis of the roller. In order to characterize such segment let the radius of the raceway flanges shown in Figure 33 be defined as,

$$R_i = \frac{1}{2}\left(d_m - D_b / \cos\alpha_k\right) \tag{4.22}$$

being the remaining geometrical features defined in Figure 17. The flange angles, in the definition of the sweeping surface obtained from the revolution of the line segments about the axis of the raceway, are referred to the orientation of η_j. The intermediate angles necessary to define such flanges are,

$$\alpha_R = \alpha_{iR} - \alpha_i \quad ; \quad \alpha_L = \alpha_{iL} + \alpha_i \tag{4.23}$$

By the same token the intermediate radius necessary to define the tapered roller bearing inner flanges are,

$$R_{iR} = R_i + \frac{l_i}{2}\sin\alpha_i \quad ; \quad R_{iL} = R_i - \frac{l_i}{2}\sin\alpha_i \tag{4.24}$$

$$R_{oR} = R_{iR} + h_{iR}\cos\alpha_R \quad ; \quad R_{oL} = R_{iL} + h_{iL}\cos\alpha_L \tag{4.25}$$

For the right inner flange, the point of contact position and the vectors are written as,

$$\mathbf{s}_Q^* = \left\{ \begin{array}{c} \frac{1}{2}l_i\cos\alpha_R + \left(\eta_j - R_{iR}\right)\dfrac{\sin\alpha_R}{\cos\alpha_R} \\ \eta_j \\ 0 \end{array} \right\} \quad ; \quad \mathbf{n}_Q^* = \left\{ \begin{array}{c} -\cos\alpha_R \\ \sin\alpha_R \\ 0 \end{array} \right\} \quad ; \quad \mathbf{b}_Q^* = \left\{ \begin{array}{c} \sin\alpha_R \\ \cos\alpha_R \\ 0 \end{array} \right\} \tag{4.26}$$

Here, contact can only occur for a parametrical range $R_{iR} \leq \eta_j \leq R_{oR}$. For the left inner flange the position of the contact point and the normal and tangent vectors are defined as,

$$\mathbf{s}_Q^* = \left\{ \begin{array}{c} -\frac{1}{2}l_i\cos\alpha_L - \left(\eta_j - R_{iL}\right)\dfrac{\sin\alpha_L}{\cos\alpha_L} \\ \eta_j \\ 0 \end{array} \right\} \quad ; \quad \mathbf{n}_Q^* = \left\{ \begin{array}{c} \cos\alpha_L \\ \sin\alpha_L \\ 0 \end{array} \right\} \quad ; \quad \mathbf{b}_Q^* = \left\{ \begin{array}{c} \sin\alpha_L \\ -\cos\alpha_L \\ 0 \end{array} \right\} \tag{4.27}$$

Just as for the right flange, also for the left inner raceway flange the contact can only occur for a parametrical range $R_{iL} \leq \eta_j \leq R_{oL}$.

4.5. Cage contacts

4.5.1. Tapered cage contacts

In the tapered bearing model considered here, the contacts between each slice of the roller and the sides of the cage or between the tops of the roller and the tops of the cage, are approached as contacts between a circle and a line, as presented in Section 4.2.3. In all that follows, the relation between the body fixed and inertial coordinates of the vector that defines the binormal vector to the contact surfaces is written as,

$$\mathbf{b}_Q = \mathbf{A}_j \mathbf{b}_Q' \tag{4.28}$$

where vector $\mathbf{b}_Q'$ defines a vector tangent to the contact surface in body fixed coordinates.

4.5.1.1. Pocket top contact

Contacts between roller tops and lines, or very narrow rectangular patches, describe well the contact between the tops of tapered rollers and the roller pocket of the cage, as depicted in Figure 34. In what follows it is assumed that the thickness of the cage is small enough to assume that the pocket shapes at the cage mid-thickness are lines that represent well the potential contact surfaces. The top of the roller is assumed as flat, reason why its contact can be detected as between a circle and a line, with the circumference located at each end of the roller. Each end of the roller can contact each top of the cage pocket either in one point or in a line along the end as shown in Figure 34 (a) and (c). Therefore, the possibility of having two points of contact by the roller flat end(s) has to be accounted for.

(a)   (b)   (c)
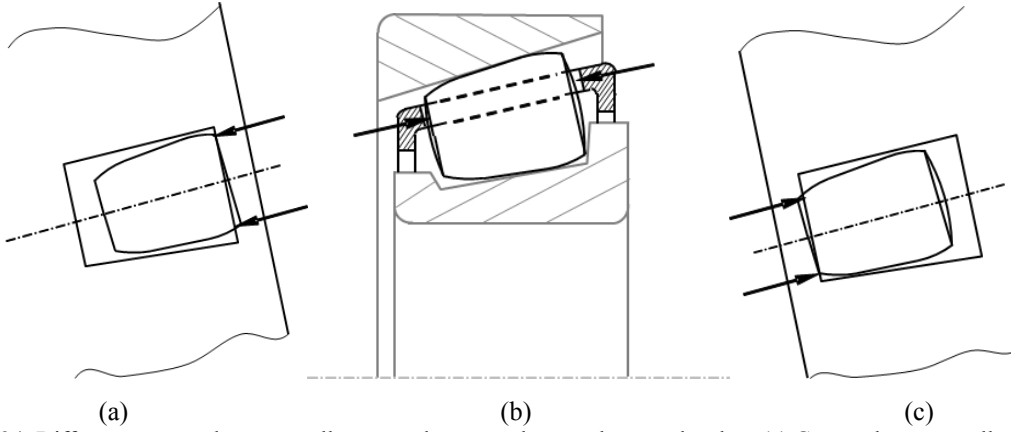
Figure 34: Different contacts between roller top and cage pocket top that can develop. (a) Contact between roller large top and cage pocket top; (b) Tops where contact can develop; (c) Contact between roller small top and cage pocket top.

The potential contact configuration between the tapered roller large flat end and the top of the cage pocket is depicted in Figure 35, where the circle corresponding to the end section of the roller approaches the line representing the mid-thickness of the top of the pocket. Two potential points of contact, Q_1 and Q_2, may develop. In order to develop the cage pocket configuration it is assumed that the center of mass of the cage, to which the body fixed coordinate frame $(\xi\eta\zeta)_c$ is attached, is located in its geometrical center. With reference to Figure 35, ξ_{0c} is half of the pocket long side dimension, R_c is the mid-thickness radius at the level of the pocket top and β_{Q1} and β_{Q2} are the angular positions of the contact points on the pocket top, Q_1 and Q_2 respectively, with respect to the body fixed direction η_c.

In order to define the contact conditions, the positions of the potential contact points in the line that defines the pocket top and the tangent vectors at such points are written as,

$$\mathbf{s}'_{Q1} = \left\{ \begin{array}{c} \xi_{0c} \\ R_c \cos\left(\beta_{Q1}\right) \\ R_c \sin\left(\beta_{Q1}\right) \end{array} \right\} \;\; ; \;\; \mathbf{b}'_{Q1} = \left\{ \begin{array}{c} 0 \\ -\sin\left(\beta_{Q1}\right) \\ \cos\left(\beta_{Q1}\right) \end{array} \right\} \tag{4.29}$$

$$\mathbf{s}'_{Q2} = \left\{ \begin{array}{c} \xi_{0c} \\ R_c \cos\left(\beta_{Q2}\right) \\ R_c \sin\left(\beta_{Q2}\right) \end{array} \right\} \;\; ; \;\; \mathbf{b}'_{Q2} = \left\{ \begin{array}{c} 0 \\ -\sin\left(\beta_{Q2}\right) \\ \cos\left(\beta_{Q2}\right) \end{array} \right\} \tag{4.30}$$

Figure 35: Contact detection between a circle and a line, representing the contact of the roller large flat end with the top of the cage pocket.

The contact situation between the roller small flat end and the top of the pocket is shown in Figure 36. The situation is similar to the contact with the large top of the roller.
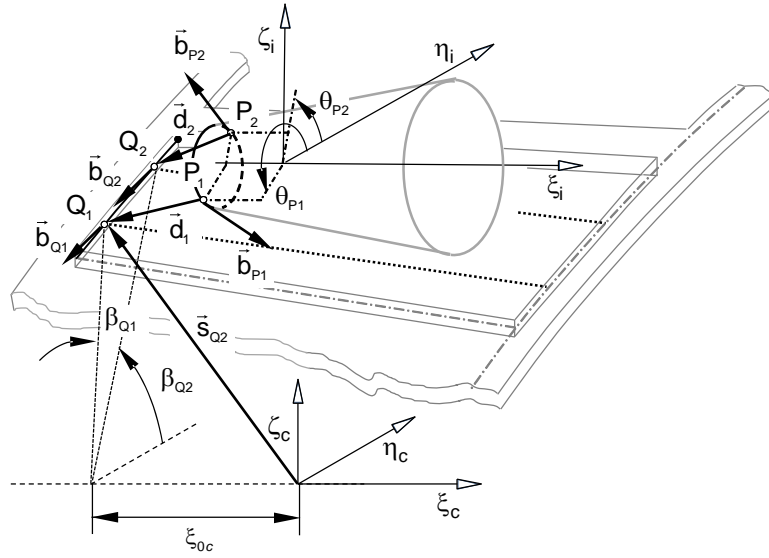
Figure 36: Contact detection between a circle and a line, representing the contact of the roller small flat end with the bottom side of the cage pocket.

The coordinates and tangent vectors of the points of contact with the cage in this situation are obtained by expressions similar to those of contact with the large end of the roller, with the required modifications. These expressions are given by,

$$
\mathbf{s}'_{Q1} = \begin{Bmatrix} -\xi_{0c} \\ R_{cb}\cos\left(\beta_{Q1}\right) \\ R_{cb}\sin\left(\beta_{Q1}\right) \end{Bmatrix} \quad ; \quad \mathbf{b}'_{Q1} = \begin{Bmatrix} 0 \\ -\sin\left(\beta_{Q1}\right) \\ \cos\left(\beta_{Q1}\right) \end{Bmatrix} \tag{4.31}
$$

$$
\mathbf{s}'_{Q2} = \begin{Bmatrix} -\xi_{0c} \\ R_{cb}\cos\left(\beta_{Q2}\right) \\ R_{cb}\sin\left(\beta_{Q2}\right) \end{Bmatrix} \quad ; \quad \mathbf{b}'_{Q2} = \begin{Bmatrix} 0 \\ -\sin\left(\beta_{Q2}\right) \\ \cos\left(\beta_{Q2}\right) \end{Bmatrix} \tag{4.32}
$$

37

where radius R_{cb} is opposite to R_c in Figure 35, i.e., the radius of the pocket top mid-thickness that corresponds to the small end of the tapered roller. In the evaluation of Eqs.(4.31) and (4.32) the parameters that define the position of the points in the top circle of the roller must be kept inside the ranges $+90°<\theta_{P1}\leq+270°$ and $-90°<\theta_{P2}\leq+90°$ in order to guarantee their separation. Contact is detected for each or for both pairs of contact between the roller small flat end and bottom of the cage pocket and/or between the roller large flat end and the top of the cage pocket.

4.5.1.2. Pocket side contact

The circle to line contact evaluation is required when checking for the collisions between the roller, represented by slices as described in Figure 22, and the side of the cage pocket. In this case, the circle, representing the slice, contacts with the pocket long side, which is represented by the line of its mid-thickness. The situation is illustrated in Figure 37 for a tapered roller cage and roller, being the orientation and position of the pocket in the cage described as in Section 4.5.1.1.
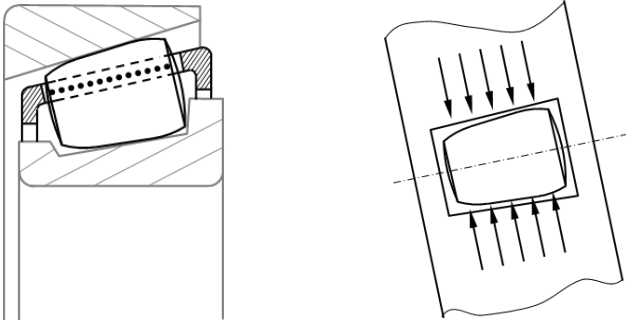
Figure 37: Contact between circle and a line, as in the contact between the roller and the side of the pocket of the cage.

The contact situation between the roller and the side of the pocket is depicted in Figure 38, where the circle corresponding to the central section of the roller slice approaches the line representing the mid-thickness of the side pocket. Note that in Figure 38 only the pair of contact between the right side of the cage pocket and the roller is fully represented.
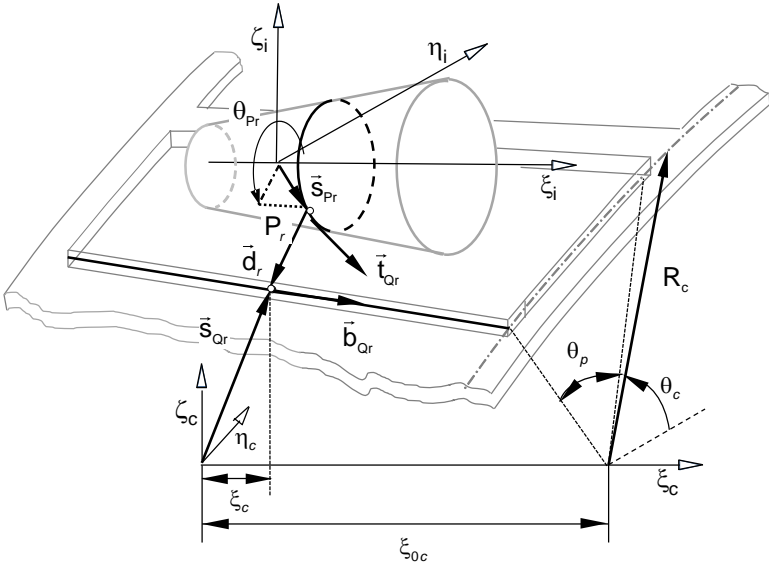
Figure 38: Contact detection between a circle and a line, representing the contact of the roller with the right side of the cage pocket.

With reference to the quantities depicted in Figure 38, the position of the contact point along the line that represents the left side of the cage pocket and its tangent vector are given as a function of the parameter ξ_c, which is also the coordinate of the point in the body fixed coordinate frame,

$$\mathbf{s}'_{Ql} = \left\{ \begin{array}{c} \xi_c \\ \left[R_c - \left(\tfrac{1}{2} W_i - \xi_c \right) \operatorname{tg} \alpha_c \right] \cos \theta_c \\ \left[R_c - \left(\tfrac{1}{2} W_i - \xi_c \right) \operatorname{tg} \alpha_c \right] \sin \theta_c \end{array} \right\} \quad ; \quad \mathbf{b}'_{Ql} = \left\{ \begin{array}{c} \cos \alpha_c \\ \sin \alpha_c \cos \theta_c \\ \sin \alpha_c \sin \theta_c \end{array} \right\} \tag{4.33}$$

where the quantities R_c, W_i, α_c and θ_c are either given as features of the roller bearing cage or calculated during the initialization of the problem.

The contact detection with the right side of the cage pocket is similar to that described by Eq. (4.33), being only the angle θ_c substituted by $\theta_c + \theta_p$, which includes the angle of the pocket itself. Therefore, the position of a point in the line of the right side of the pocket is,

$$\mathbf{s}'_{Qr} = \left\{ \begin{array}{c} \xi_c \\ \left[R_c - \left(\tfrac{1}{2} W_i - \xi_c \right) \operatorname{tg} \alpha_c \right] \cos \left(\theta_c + \theta_p \right) \\ \left[R_c - \left(\tfrac{1}{2} W_i - \xi_c \right) \operatorname{tg} \alpha_c \right] \sin \left(\theta_c + \theta_p \right) \end{array} \right\} \quad ; \quad \mathbf{b}'_{Qr} = \left\{ \begin{array}{c} \cos \alpha_c \\ \sin \alpha_c \cos \left(\theta_c + \theta_p \right) \\ \sin \alpha_c \sin \left(\theta_c + \theta_p \right) \end{array} \right\} \tag{4.34}$$

Effective contact occurs if both Eq.(4.5) and Eq.(4.3) are fulfilled. The contacts with the left and right side of the cage pocket must be checked independently. In any case, if a particular roller slice is in contact with one side of the cage it is unlikely that it also contacts with the other side, unless the width of the pocket is smaller than the roller diameter and the whole cage position is shifted such a way that it is 'compressing' the roller.

4.5.2. Spherical cage contacts

The necessary equations to detect contact with the spherical cage have not been formulated in the development reported in this work. However, due to the geometry of the spherical roller bearing cage, the contact with the rollers is closer to circle to surface contact than that of the tapered roller bearing cage.

4.6. Other contacts

4.6.1. Contact between spherical cap and conical surface

Over the description of contact detection between the tapered roller top and flanges or cage tops, it has been assumed that the top of the roller is flat, reducing the identification of the proximity point on its surface to the search on a circle. However, the tapered roller large end is, in fact, a spherical surface, with a small curvature. The first approach to detect contact between the large end of the roller and the cage top requires the solution of the correspondent system of nonlinear equations, which has shown to be prone to convergence errors due to the large value of the curvature radius of the roller large top. In future developments this aspect must be considered to obtain more accurate results with the dynamic analysis tool, provided that further investigation is done to identify solutions for the convergence errors.

A convenient parameterization of the spherical cap geometry, with reference to the data used to define the tapered roller, is proposed here. The contact between the tapered roller large end, with, as an example, the inner raceway flange, is represented as a contact between a spherical cap and a conical surface, as depicted by Figure 39. The parameterized conical geometry is described in Section 4.4.2.
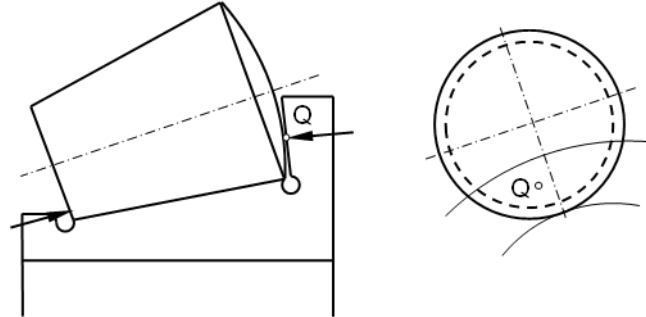
Figure 39: Typical contact between spherical cap and conical surface, as in the contact between the tapered roller large end top and the flange of the inner raceway.

The geometry of the spherical cap is obtained as the surface resulting from sweeping the arc of circumference, depicted in Figure 40, about the roller axis. In this case the surface of the spherical cap is defined by two parameters, the angle φ, represented in Figure 40, and the angle θ_2.

(a)   (b)
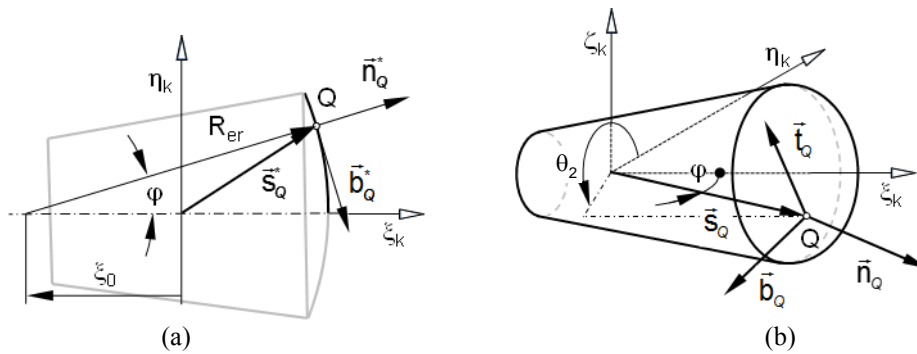
Figure 40: Contact point, surface normal and tangent vectors for the spherical cap of the tapered roller bearing end: (a) Contact point in the local plane: (b) Spatial geometry of the spherical cap.

The position of any point in the arc of circle, and the corresponding normal and tangent vectors, are written as,

$$\mathbf{s}_Q^* = \begin{Bmatrix} \xi_0 + R_{er} \cos \varphi \\ R_{er} \sin \varphi \\ 0 \end{Bmatrix} \quad ; \quad \mathbf{n}_Q^* = \begin{Bmatrix} \cos \varphi \\ \sin \varphi \\ 0 \end{Bmatrix} \quad ; \quad \mathbf{b}_Q^* = \begin{Bmatrix} \sin \varphi \\ -\cos \varphi \\ 0 \end{Bmatrix} \tag{4.35}$$

Contact can only occur for a parametrical range of $0 \le \varphi \le \varphi_{\max}$, where φ_{max} is fixed by the definition of the roller geometry.

4.7. Solution of the nonlinear system of equations

It has been seen that the identification of the closest points between the geometrical features of two bodies must fulfil several conditions, namely Equations (4.2), (4.4) or (4.5) depending on the case in study. These equations define sets of equations that involve the inner product between vectors that depend on the geometry and kinematics of each interacting body. These vectors involve the distance vector between the two points candidate to contact and other vectors that are either the normal or tangent

to the surface or line. Over time, the location of the nearest points can change, reason why the location and normal and tangent vectors in each point of the potential contact pair depend on specific parameters. The parameters are usually linear dimensions or angles. The challenge, in each time step and each contact pair, consists in the identification of two points whose coordinates satisfy the specific equations for minimum distance, which is achieved by solving a system of nonlinear equations for each pair of contact.

4.7.1.1. Newton-Raphson's method

In order to solve the equations for minimum distance, a numerical method for finding roots of functions is the most appropriate, since it needs to be incorporated into the computational program and should be fast and accurate. When studying the available methods, the Newton-Raphson method appears as the most appealing, for its simplicity, computational easiness and for being a powerful method that generally has a quadratic convergence, resulting in fast and accurate results. Newton's method uses an initial estimation of the parameters to progress with an iterative procedure until the values of these parameters that satisfy the given equations are identified. The initial estimation values are calculated by the `BearDyn` code before calling the integration method and are based on the geometry data provided by the user. These values are delivered to the integration method to be used in the contact detection in the beginning of the analysis and are updated for every successful time-step with the values calculated in the previous time step. The Newton's method is formulated as,

$$\mathbf{x}_{n+1} = \mathbf{x}_n - \frac{f(\mathbf{x}_n)}{f'(\mathbf{x}_n)} \tag{4.36}$$

where the counter n refers to the iteration number, $\mathbf{x}$ is a vector containing the desired variables, $f(\mathbf{x}_n)$ is the function to be evaluated, either based on Equation (4.2), Equation (4.4) or Equation (4.5) for each contact pair, and $f'(\mathbf{x}_n)$ is the Jacobian matrix. Newton's method is solved for each pair of contact points, until a solution is found, i.e., when the fraction between the function vector and the Jacobian is smaller than a tolerance specified by the user.

4.7.1.2. "fsolve" solver

The Newton-Raphson's method does not ensure universal convergence, being the lack of convergence characterized by reading the maximum number of iterations specified by the user. In order to avoid problems that can arise from using different values or to avoid the extra computational effort resulting from the use of an extremely high maximum number of iterations, another method for the solution of a nonlinear system of equations is used when the Newton Raphson method fails. The MATLAB® solver *fsolve* is chosen and implemented to calculate the potential contact points for the case of failure of convergence from Newton's method. *fsolve* is used to solve systems of nonlinear equations based on given initial values, using an algorithm based on a trust-region dogleg method, which is specially designed to solve nonlinear equations. Although *fsolve* is slower that the Newton-Raphson's method, it

does not require that the Jacobian matrix is provided. To understand the trust-region approach, consider the unconstrained minimization problem, *min f(x)*, where the function takes vector arguments and returns scalars. Supposing a starting point *x* in *n*-space, it is required to move to a point that leads to a lower function value. The basic idea is to approximate *f* with a simpler function *q*, which reasonably reflects the behaviour of function *f* in a neighbourhood *N* around the point *x*. This neighbourhood is the trust region. A trial step *s* is computed by minimizing, or approximately minimizing, over *N*. For additional understanding on this method, the reader is directed to references [39] [40].

The use of *fsolve* has shown to solve the problem with the lack of convergence of solutions, since this solver has more stopping criteria than the implemented Newton-Raphson method, which simply assumes convergence when the error between consequent results is smaller than a specified tolerance. *fsolve* here accepts a result as correct when the different possibilities, specified in Table 4, occur.

Function converged to a solution *x*.
Change in *x* was smaller than the specified tolerance.
Change in the residual was smaller than the specified tolerance.
Magnitude of search direction was smaller than the specified tolerance.

Table 4: Possible reasons for convergence of the *fsolve* method

This solution procedure solves the problem of convergence, but introduces a slight increase in the total computational effort required by the dynamic analysis tool when these cases occur. However, this increase in integration time caused by the use of *fsolve* is necessary to obtain the required accuracy in results.

5. FORMULATION OF CONTACT FORCES

During the contact detection it is possible to identify the location of the points in contact with the surfaces of the rolling elements, the relative indentation and orientation between the contacting surfaces. These are the kinematic variables required by the models of the normal contact forces and the friction and hydrodynamic forces. These last also use the relative velocities which are introduced here. The loading of the rollers, raceways and cage is evaluated in two stages: first, the normal contact forces are evaluated using Hertzian contact models; second, the tangential contact forces are evaluated using friction and tribological models, recognizing the lubrication mode present in each contact.

Once contact is detected using the methodology presented in Chapter 4, the contact forces are applied in each pair of contacting points P and Q. The contact force vectors, applied in bodies i and j, are related to each correspondent normal vectors by,

$$\mathbf{f}_P = -f_n \ \mathbf{n}_P$$
$$\mathbf{f}_Q = -f_n \ \mathbf{n}_Q$$

(5.1)

where f_n is the normal contact force developed during contact, which is a value proportional to the indentation developed between the two bodies, δ, calculated by Eq.(4.3).

Besides the normal forces that develop during contact, also tangential forces due to friction or to the lubrication fluid develop between the contacting bodies. The tangential forces are also applied in each pair of contacting points P and Q and their value is proportional to the normal force developed during contact. For the evaluation of tangential, or creep, forces it is necessary to calculate the relative velocity between the bodies, namely its projection on the surface tangent to the contacting bodies on the points of contact. The velocities of the contact points P and Q are obtained by taking the time derivative of the position vectors, $\mathbf{r}_P$ and $\mathbf{r}_Q$, written as,

$$\dot{\mathbf{r}}_P = \dot{\mathbf{r}}_i + \mathbf{A}_i \tilde{\boldsymbol{\omega}}_i' \mathbf{s}_P'$$
$$\dot{\mathbf{r}}_Q = \dot{\mathbf{r}}_j + \mathbf{A}_j \tilde{\boldsymbol{\omega}}_j' \mathbf{s}_Q'$$

(5.2)

where $\dot{\mathbf{r}}_i$ and $\dot{\mathbf{r}}_j$ are the velocities of the origin of the body fixed referential and $\tilde{\boldsymbol{\omega}}_i'$ and $\tilde{\boldsymbol{\omega}}_j'$ the skew-symmetric matrices associated to the angular velocities of body i and j, respectively, expressed in the body fixed coordinate systems. The relative velocity between bodies i and j in the point of contact is obtained as,

$$\dot{\mathbf{r}}_{PQ} = \dot{\mathbf{r}}_P - \dot{\mathbf{r}}_Q$$

(5.3)

The sliding velocity of the bodies in the contact point is just the projection of the relative velocity vector $\dot{\mathbf{r}}_{PQ}$ in the tangent plane to the contacting surfaces in the contact point, as,

$$\mathbf{u} = \dot{\mathbf{r}}_{PQ} - \left(\dot{\mathbf{r}}_{PQ}^T \mathbf{n}_Q \right) \mathbf{n}_Q$$

(5.4)

Figure 41 illustrates the plane tangent to the contacting surface and circumference that passes by the contact point, as well as the sliding velocity calculated by Eq. (5.2).
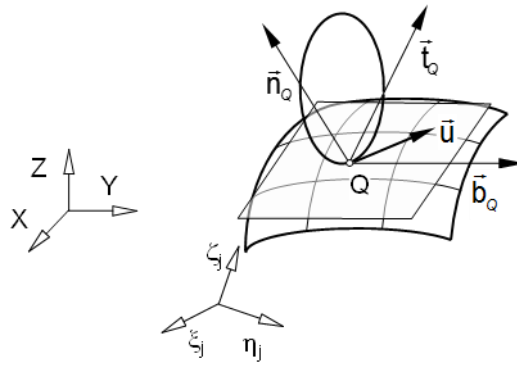
Figure 41: Tangent plane, to both surface and circumference, passing by the contact point and sliding velocity vector.

In all normal contact force, friction force or lubrication force models used for the contact of the rolling elements in the bearings the kinematic quantities required, i.e., contact point positions, penetrations, normal vectors to the surfaces and relative sliding velocities are calculated using the equations introduced from Chapter 4 up until this point.

5.1. Normal contact forces

The normal contact forces developed during the contact between the rolling elements, although large, are distributed over a small area when compared with the dimensions of the contacting surfaces. Typical examples of contact between rolling elements are described in Figure 42 for cases of wheel-rail contact and rolling bearings.

(a)   (b)

(c)   (d)
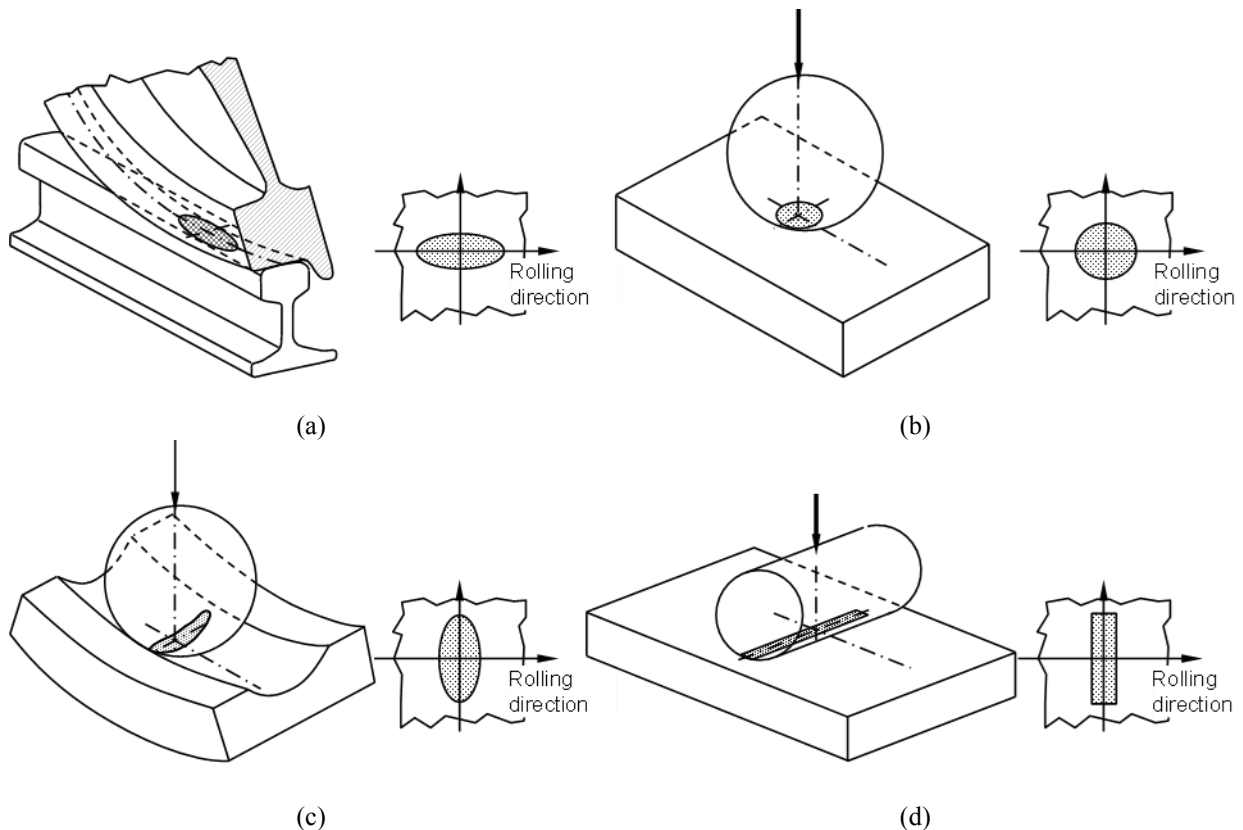
Figure 42: Contact patches for cases of Hertzian contact force models: (a) Elliptical contact; (b) Point contact; (c) Elliptical contact; (d) Line contact.

44

The stress distribution over the contact area, or contact patch, is described by Hertz elastic contact theory if some conditions are met [27]. In order for the Hertz elastic contact theory to be valid it is required that:

- All deformations must be within the linear elastic limits, i.e., the strains are small and the body stresses can be described by a linear elastic constitutive relation;

- All shear stresses are neglected, i.e., the loading is assumed normal to the contacting surfaces and, therefore, the contact is frictionless;

- The dimensions of the contact patch are small when compared to the dimensions of the surfaces in contact, i.e., the contact area is much smaller than the characteristic radii that define the surfaces curvatures, implying in turn that the surfaces are continuous and non-conforming.

Typically point contacts, described by elliptical contact patches as those described in Figure 43, and line contacts, described by the rectangular contact patch shown in Figure 44, are of importance in the contact of rolling elements, and are used extensively in the rolling bearing dynamics. It is not the objective of this work to provide thorough presentation of the Hertz elastic contact theory but simply to register its main findings that are of importance to the representation of the normal contact forces between rolling elements of bearings.

5.1.1. Point contact

The point contact between two solids leads to elliptical contact patches with the geometry depicted in Figure 43, in which it is assumed that the rolling direction is along the X axis. In roller bearings the contact between the rollers ends and the raceway flanges or the cage tops are characterized as point contacts.

(a)   (b)
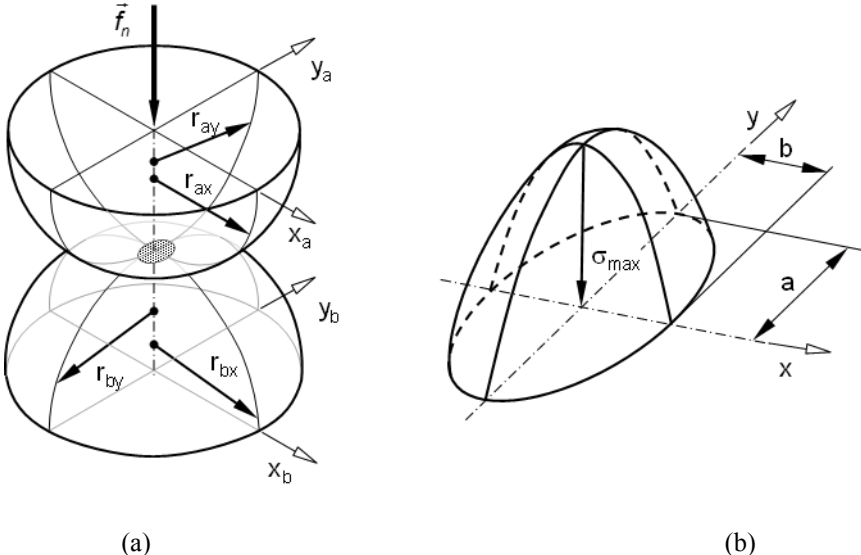
Figure 43: Elliptical contact: (a) Geometric definitions; (b) Stress distribution and contact patch geometry.

Let the interference, or compression, between two surfaces be described by δ, which is found using Eq.(4.3). The normal contact force, in the case of point contact is,

$$f_n = K_{pt} \delta^{3/2} \tag{5.5}$$

where proportionality factor K_{pt}, or contact stiffness, is given by [41],

$$K_{pt} = \pi \kappa E' \left(\frac{\mathbb{R}\mathbb{E}}{4.5\mathbb{F}^3} \right)^{1/2} \tag{5.6}$$

being the characteristic radii of the contacting surfaces described in Figure 43, $\kappa = a/b$, with a and b being the semi-axis of the contact ellipse and $\mathbb{E}$, $\mathbb{F}$ are complete elliptical integrals of first and second kind [42]. Using a least-square relation, Brew and Hamrock [43] find an approximate expression for the elliptical integrals and for κ as,

$$\kappa = 1.0339 \left(\frac{R_y}{R_x} \right)^{0.636}$$

$$\mathbb{F} = 1.5277 + 0.6023 \ln \left(\frac{R_y}{R_x} \right) \tag{5.7}$$

$$\mathbb{E} = 1.0003 + 0.5968 \left(\frac{R_x}{R_y} \right)$$

where,

$$R_x = \left(\frac{1}{r_{ax}} + \frac{1}{r_{bx}} \right)^{-1} \quad ; \quad R_y = \left(\frac{1}{r_{ay}} + \frac{1}{r_{by}} \right)^{-1} \tag{5.8}$$

and,

$$\mathbb{R} = \frac{R_x}{R_y} \tag{5.9}$$

The equivalent modulus E' is given as,

$$E' = 2 \left(\frac{1-\nu_1^2}{E_1} + \frac{1-\nu_2^2}{E_2} \right)^{-1} \tag{5.10}$$

where E_1, ν_1 and E_2, ν_2 are the Young's modulus and Poisson's ratio of the material of each body in contact, respectively.

The evaluation of the maximum stress developed during contact is also of interest since it is used in the evaluation of tangential forces caused by lubricated rolling contact. For a point contact the maximum stress in the contact patch, shown in Figure 43, is written as [44],

$$\sigma_{\max} = \frac{3f_n}{2\pi ab} \tag{5.11}$$

with the dimensions of the semi-axis of the elliptical contact patch found as [41],

$$a = \left(\frac{6\kappa^2 \mathbb{E}\mathbb{F}\mathbb{R}}{\pi E'} \right)^{1/3}$$

$$b = \left(\frac{6\mathbb{E}\mathbb{F}\mathbb{R}}{\pi \kappa E'} \right)^{1/3} \tag{5.12}$$

where a is referred to as the semimajor and b the semiminor axes of the contact ellipse developed.

5.1.2. Line contact

The ideal line contact, illustrated in Figure 44, can be understood simply as a case in which the ratio $\kappa \rightarrow \infty$ due to the fact that $a \gg b$. However, the relation between indentation and normal force becomes, in this case, a nonlinear relation that requires an iterative procedure to obtain the normal force when the indentation is known. Several elastic contact models for cylinders with parallel axis based on the Hertz elastic contact theory have been proposed. The Johnson model, used by the ESDU-78035 Tribology Series [45], is given by,

$$\delta = \frac{f_n L_{ef}}{\pi E^*}\left[\ln\left(\frac{4\pi E^* \Delta R}{f_n L_{ef}} \right) - 1 \right] \tag{5.13}$$

where L_{ef} represents the effective contact length, generally equal to the length of the shorter cylinder and where the composite modulus E^* and the characteristic radii ΔR are given by,

$$E^* = \left(\frac{1-v_1^2}{E_1} + \frac{1-v_2^2}{E_2} \right)^{-1}$$

$$\Delta R = \begin{cases} r_{ax} - r_{bx} & \text{internal contact} \\ r_{ax} + r_{bx} & \text{external contact} \end{cases} \tag{5.14}$$

<center>(a)   (b)</center>
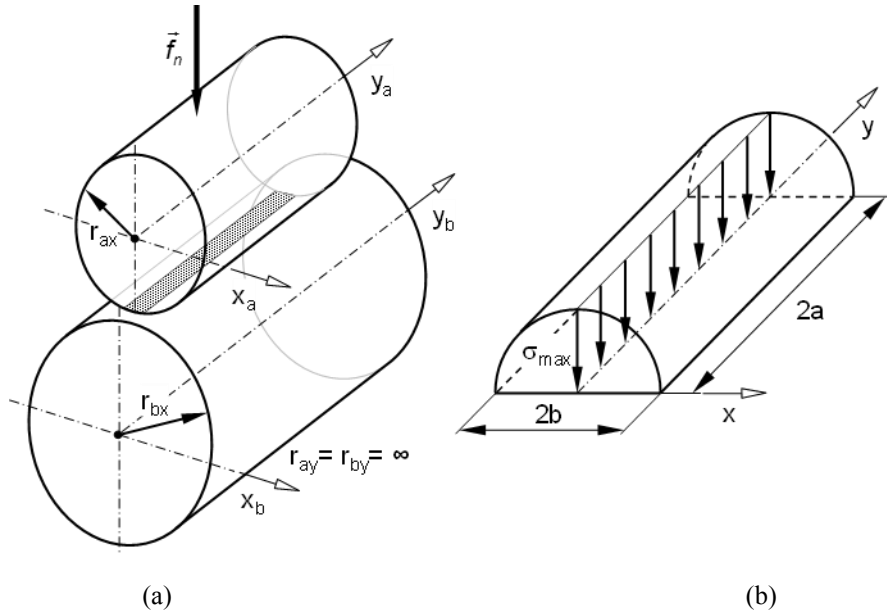
Figure 44: Line contact: (a) Geometric definitions; (b) Stress distribution and contact patch geometry

Different other solutions for the relation between the indentation and the normal force on the contact between cylinders with parallel axis have been proposed in the literature. In formulas for stress and strain, by Roark [46], the expression first proposed by Radzimovsky [47] is presented as,

$$\delta = \frac{f_n L_{ef}}{\pi E^*}\left[\frac{2}{3} + \ln\left(\frac{4r_{ax}}{b} \right) + \ln\left(\frac{4r_{bx}}{b} \right) \right] \tag{5.15}$$

where the parameter b is,

$$b = 2.15\sqrt{\frac{f_n R}{E}} \tag{5.16}$$

with $R = (r_{ax} r_{bx} / \Delta R)$, being ΔR given by Eq. (5.14). In Eq. (5.16) it is assumed that the materials used in the contacting surfaces have identical material properties. By substituting the relations of Eq. (5.16) into Eq. (5.15) leads to,

$$\delta = \frac{f_n L_{ef}}{\pi E^*} \left[\frac{2}{3} + \ln \left(\frac{8 E \, \Delta R}{2.15^2 f_n L_{ef}} \right) \right] \tag{5.17}$$

Another cylindrical contact model has been proposed by Goldsmith and expressed as [48],

$$\delta = \frac{f_n L_{ef}}{\pi E^*} \left[1 + \ln \left(\frac{\pi E^*}{f_n L_{ef} R} \right) \right] \tag{5.18}$$

When used in the framework of computational dynamics, in which the normal contact force needs to be calculated based on a known indentation, resulting for the known positions of the contacting bodies, the line contact models considered so far are computationally inefficient. The iterative procedure required to calculate the contact force for a given indentation, required by the use of Eqs. (5.13), (5.17) or (5.18) not only is costly when a very large number of contacts have to be calculated, as in the case of roller bearing dynamics, but is also prone to convergence difficulties. Furthermore, the different line contact models discussed so far have limitations in their range of applications, as discussed by Pereira et al. [49]

To overcome the numerical difficulties and the physical limitations on the use of the Hertz based contact models by Johnson, Radzimovsky or Goldsmith, Pereira et al. proposed a cylindrical contact model that does not require an iterative procedure to calculate the normal contact force [49], written as,

$$f_n = \frac{\left(\bar{a} \, \Delta R + \bar{b} \right) L_{ef} E^*}{\Delta R} \delta^n \tag{5.19}$$

in which,

$$\bar{a} = \begin{cases} 0.49 & \text{internal contact} \\ 0.39 & \text{external contact} \end{cases} \tag{5.20}$$

$$\bar{b} = \begin{cases} 0.10 & \text{internal contact} \\ 0.85 & \text{external contact} \end{cases} \tag{5.21}$$

$$n = \begin{cases} Y \Delta R^{-0.005} & \text{internal contact} \\ 1.094 & \text{external contact} \end{cases} \tag{5.22}$$

In Eq. (5.22) the constant Y reflects the fact that for internal contact it is not possible to find a single expression to obtain a fit with good correlation between the Johnson and exponential fit function for the complete range of clearances ΔR. The best fit is obtained with the constant Y given by,

$$Y = \begin{cases} 1.56 \left[\ln \left(1000 \, \Delta R \right) \right]^{-0.192} & \text{if } \Delta R \in [0.005, 0.750[\, mm \\ 0.0028 \, \Delta R + 1.083 & \text{if } \Delta R \in [0.750, 10.00[\, mm \end{cases} \tag{5.23}$$

This cylindrical contact model matches in precision Johnson model in its range of validity and extends the range of application of current models due to the extensive use of finite element models for cylindrical contact, which are not prone to the Hertz elastic contact limitations.

For any of the normal contact force models presented, the maximum contact stress in the rectangular patch is given by,

$$\sigma_{max} = \frac{2 f_n}{\pi L_{ef} b} \tag{5.24}$$

with the dimensions of the dimension b of the contact patch found as,

$$b = 0.00335 \left(\frac{f_n}{L_{ef} \Sigma_p} \right)^{\frac{1}{2}} \tag{5.25}$$

where,

$$\Sigma_P = \frac{1}{r_{ax}} + \frac{1}{r_{ay}} + \frac{1}{r_{bx}} + \frac{1}{r_{by}} \tag{5.26}$$

All cylindrical contact models presented assume ideal line contact, i.e., the geometry of the cylinders is perfect and contact takes place in the full extension of the shorter cylinder. In roller bearings the rollers are crowned and the contact models presented do not represent correctly the relation between indentation and normal force. Based on laboratory testing, Palmgren [50] developed a relation, which is the basis of current contact models in roller bearing line contact, written as,

$$\delta = 3.81 \left[\frac{2\left(1 - v^2\right)}{\pi E} \right]^{\frac{9}{10}} \frac{f_n^{\%_{10}}}{L_{ef}^{\%_{10}}} \tag{5.27}$$

which rearranged and having the normal force written as a function of the indentation, or relative elastic approach, is,

$$f_n = 0.71069 E^* L_{ef}^{\%_9} \delta^{\%_9} \tag{5.28}$$

In order to apply the normal contact force model for line contact to the roller contact with the inner and outer raceways and with the sides of the cage pocket, the roller is discretized in N_{sl} strips, as implied by Figure 22.

The contact search for each strip is evaluated using the procedure described in section 4 and for the contact force is evaluated based on the strip indentation. The normal contact force of a strip of the roller is given by Palmgren's simplified equation [25],

$$f_{ns} = 0.356 E' N_{sl}^{-\frac{1}{9}} L_{ef}^{\%_9} \delta_s^{\%_9} \qquad s = 1,...,N_{sl} \tag{5.29}$$

where the counter s refers to the number of the slice in each of the rollers.

5.2. Tangential contact forces

Surfaces in rolling contact, subjected to normal contact loads are also subject to tangential forces due to friction, in the case of dry contact such as for rail-wheel interaction, or due to the lubricant, in the case of lubricated contact as in normal roller bearing applications. Regardless of the type of contact, the relation between the tangential forces and the normal contact forces is given by,

$$f_t = \mu f_n \tag{5.30}$$

where μ is the equivalent friction coefficient. For the sake of brevity the subscripts *t* and *n* are used instead of *ts* and *ns* used in Eq.(5.29). Note also that the tangential force is applied in the opposite direction of the relative velocity between the contacting surfaces, obtained by Eq. (5.4).

The simple form of Eq. (5.30) hides the complexity of the calculation of μ for many important tangential forces, as in the case of lubricated contact. In the case of lubrication between the contacting surfaces, depending on the lubricant film thickness and on the roughness of the contacting surfaces the type of contact is different and the equivalent friction coefficient has to be evaluated differently. Figure 45 shows the different contact modes, from dry contact through full fluid film lubricated mode.

(a)   (b)

(c)   (d)
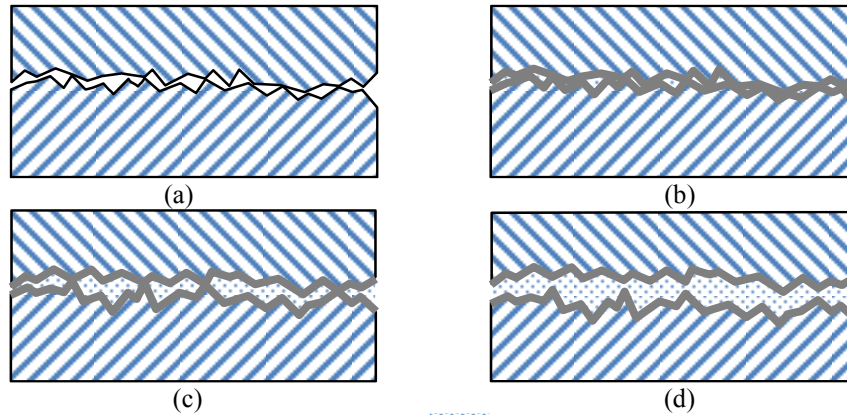
Figure 45: Types of contact (━━━ Boundary lubricant layer, ▨ Lubricant): (a) Dry contact; (b) Boundary mode; (c) Mixed mode; (d) Full fluid mode.

For lubricated contact, the relation between the fluid film thickness and the roughness of the contacting surfaces defines the type of contact mode that is taking place. Let the lubricant film parameter be defined as,

$$\Lambda = \frac{h_c}{\sqrt{\sigma_1^2 + \sigma_2^2}} \tag{5.31}$$

where h_c is the lubricant film central thickness and σ_1 and σ_2 the roughness of the contacting surfaces. Assuming for each lubrication mode a different equivalent friction coefficient, the relation between μ, in Eq. (5.30), such lubrication mode equivalent friction coefficients is written as [38],

$$\mu = \begin{cases} \mu_{bd} & \Lambda \leq \Lambda_{bd} \\ \dfrac{\mu_{bd} - \mu_{fm}}{\left(\Lambda_{bd} - \Lambda_{fm}\right)^6}\left(\Lambda - \Lambda_{fm}\right)^6 + \mu_{fm} & \Lambda_{bd} \leq \Lambda < \Lambda_{fm} \\ \mu_{fm} & \Lambda > \Lambda_{fm} \end{cases} \tag{5.32}$$

The typical values for the lubricant film parameter used to define he transitions between the different lubrication modes are Λ_{bd}=0.01 and Λ_{fm}=1.5 [38]. The evaluation of the equivalent friction coefficient required the prior evaluation of the lubricant film parameter, which in turn imply the calculation of the lubricant film thickness, and the equivalent friction coefficients for each mode of lubrication, μ_{bd} and μ_{fm}.

A sequence of the steps to be taken to theoretically calculate the equivalent friction coefficient can be resumed as:

1. Calculate lubricant film thickness, h_c
   a. Calculate adimensional parameters H, U, W and G;
   b. Calculate isothermal central lubricant fluid thickness, h_{iso};
   c. Calculate thermal reduction factor, ϕ_T;
   d. Calculate starvation factor, ϕ_S.
2. Calculate equivalent friction coefficients
   a. Calculate boundary mode equivalent friction coefficient, μ_{bd};
   b. Calculate full-film mode equivalent friction coefficient, μ_{fm}.

The prominence of each step and the determination of the enumerated parameters is described in Appendix D – Equivalent Friction Coefficient Calculation. These are not introduced in this chapter, since the theoretical calculation of the full-film mode equivalent coefficient of friction is described as a complex procedure and its applicability was not required for the conditions tested by the dynamic analysis tool developed. In any case, the values resulting from its calculation are not in the range $0<\mu_{fm}<\mu_{bd}$, while the calculation of the boundary mode equivalent friction coefficient has been confirmed, as well as the former models used to calculate the lubricant film thickness. In order to avoid the use of incorrect values as the full-film mode equivalent friction coefficient, two solutions are identified in order to still allow the simulation of roller bearings in the computational tool `BearDyn` considering lubrication:

1. The use of experimental values for μ_{fm} and μ_{bd}. In the context of this work, the partners of MAXBE at FEUP will, in the future, measure the values of the equivalent coefficient values for the lubricants used in project MAXBE.
2. The use of a constant, pre-defined, value for the equivalent friction coefficient, μ. This is the ultimate adequate solution in order to allow performing dynamic analysis with `BearDyn` for chosen roller bearings, while considering the application of tangential forces. A constant value of μ=0.1 was chosen, which corresponds to the maximum possible value of the equivalent friction coefficient.

In the future, additional studies must be done in this area in order to allow the numerical calculation of the full film mode equivalent coefficient and, then, of the friction coefficient to be used to calculate the forces resulting from tangential contact.

6. COMPUTATIONAL IMPLEMENTATION

The initialization of the positions and velocities of each body of the roller bearing system and the evaluation of all forces acting on the bodies are possible to be computed and the general knowledge about the dynamics of a multibody system is described in the previous chapters. With this information, the dynamic analysis tool is created to allow the description of each element and their interactions over time, with the acronym `BearDyn`. The computational tool `BearDyn`, entirely developed in MATLAB®, includes the implementation of all functions used except for the time integrators and *fsolve*, for the solution of the nonlinear system of equations. The program was developed by steps, where each problem was only approached after the previous was resolved; for example, contact detection with the cage was only implemented after contact with raceways was functioning properly. As mentioned earlier, the integrator used was an ordinary differential equation solver from MATLAB® library of functions, which code was not modified. Its behaviour was, yet, controlled resorting to an integration argument called *options*, as detailed in Section 6.2.

The `BearDyn` program is quite complex due to the number of functions involved in the detection of contacts at each time step, but in a general way follows a fairly simple structure. The core of the program is the integration process, which evaluates a number of functions to obtain the vector $\dot{\mathbf{y}}$ to be integrated at each time step, as described in Chapter 2. A scheme of the program's main structure can be seen in Figure 46, where the functions are presented in boxes highlighted with a double outline, with their original names.
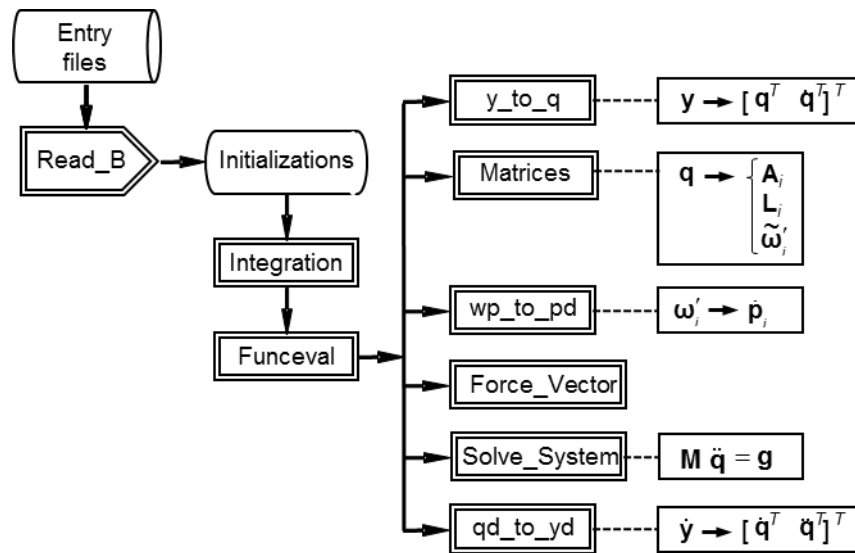
Figure 46: Scheme of `BearDyn` code main structure.

The program `BearDyn` uses text files as inputs, referred to as "Entry files" in Figure 46, which give information about the geometry of the bearing, integration parameters, material properties, lubricant parameters, as well as the forces resulting from wheel-rail contact to be applied on the inner raceway over time. The necessary entry files to be used in program `BearDyn` are detailed in Appendix E – BearDyn User Manual. With the information given, the initial conditions are settled, such as the

52

initial positions, orientations and velocities of the bodies, the initial estimations of contacting points, the initial mass matrix, as well as other values, vectors and matrices needed for various aspects of the code. These initializations are used as the starting conditions for the integration, which calls function *Funceval*, shown in Figure 46, successively over each time step of the total integration time defined. *Funceval* is the core of the program, where the necessary functions are called to obtain the $\dot{y}$ vector, which is then integrated by the time integrator, delivering the resulting vector **y** . This vector is then used to define the positions and velocities of the bodies on the next integration step, by calling *Funceval* again, and the process is repeated for each time step.

At each time step, the process which requires most computational effort is the calculation of the force vector, particularly the vector resulting from contact forces. This is explained by the significant number of contacts considered on each body, which need to be detected independently, by solving large number of systems of nonlinear equations. This procedure is done in a function with the name *Contact_Detection*, as shown in Figure 47. In Figure 47 is a diagram representing the structure of the functions which allow calculation of the force vector.
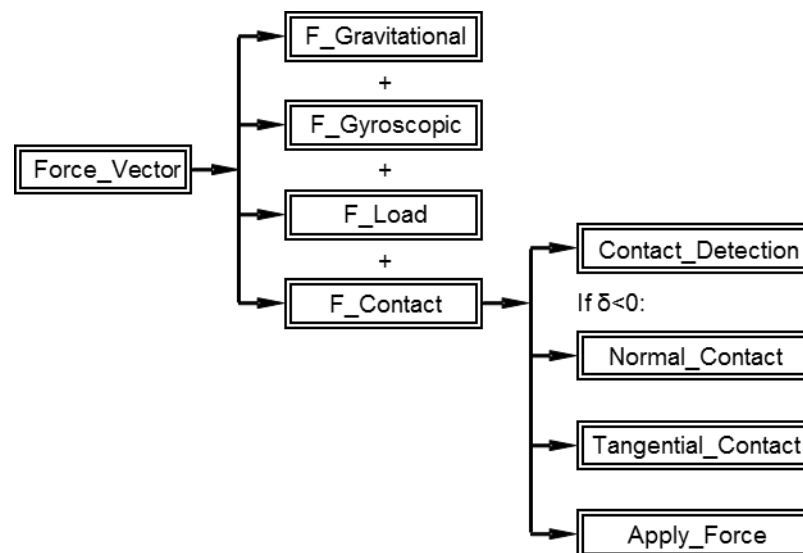
Figure 47: *Force_Vector* function structure.

With reference to Figure 47, if effective contact is detected, the resulting normal and tangential forces are calculated and applied into the force vector.

6.1. Time integration method

The time integration method used to solve the equations of motions over time of the multibody system in `BearDyn` is selected among the ordinary differential equation solvers available in MATLAB®. The time integration method used from MATLAB® was an ordinary differential equation solver known as ODE45, which is recognized for self-adjusting the integration time-steps over time and realizing several integration searches to obtain successful results. This means that, even though the user can define the time-steps from which to select results, it does not mean that the integrator will exclusively calculate

results in those points. The integrator proceeds to calculate results for different time steps, first, and afterwards those are selected from which seem the most accurate, as having the smallest error compared to the previous result, for example. This results in having time steps which are calculated and so-called not successful, opposed to those which are selected from the integrator and called successful time steps.

6.2. Integration parameters

The integration method ODE45 was not modified in its coding, but controlled resorting to an optional integration argument called *options*. The *options* argument is created with the function *odeset*, which is a specific function that allows to adjust the integration parameters of ODE solvers. One of the most important adjustments made to allow the integrator to update the *Init* struct only when a successful time step existed. This is achieved by setting a solver output property with *odeset*, given as *OutputFcn*. This property controls the output that the solver generates, as a function handle which is called after every successful integration steps only. In this form, a handle function is created to retrieve the *Init* struct from *Funceval* when the integration step is successful and ignores its update when the contrary occurs.

One of the most struggling problems that was taken into account when coding the program was the time each simulation took to be performed. So, since the beginning, methods to achieve computational efficiency were preferred, which included reducing the time the integration itself consumed, without losing its accuracy. Understanding the methodology of an integrator with a variable time step, it is known that the time step adjusts itself to the frequency contents of the system time response. This means that, if the integrator finds successive similar results for a certain time span, it will increase its time step accordingly until a variation is found. In this problem, since forces are proportional to the penetration between two bodies, it can happen that the difference between two time steps is large enough to detect a penetration at a time where it is extremely high. This situation causes the integrator to try a higher number of time steps in order to find the solution, sometimes leading to excessively high total integration times. This situation can be avoided by defining a maximum permitted time step, so contact is detected at its early phase, allowing only for small penetrations. This value is also set in ODE45's *options*, usually with the value of 10^{-5}s.

6.3. *Init* struct

When detecting contact, an iterative process is used to solve the nonlinear equations needed to find the values of certain variables which define the position of the closest points between bodies. The iterative processes used are both the Newton-Raphson's method and *fsolve*, a method from MATLAB®, as mentioned in Section 4.7. Both methods require initial values to be used as start values to the iteration. The closest these are to the final result, the faster the search method is and the smaller is the number of iterations needed. In `BearDyn,` these initial values are all introduced in a single struct and organized according to the type of contact of a particular pair. In each time step all the proximity points are calculated and new variables are found. The initializations struct to be used in the next time step includes

as initial values the values obtained in the previous time step. Note, however, that the update only occurs when a time step succeeds. Otherwise, the update of the initial values for contact detection does not occur.

6.4. Verification methods

When creating a computational tool like `BearDyn`, there are very few ways to verify if the results are correct, since there are no other available similar enough programs or studies which can be used to compare results and experimental procedures are not possible. Several methods were, then, used in this case to validate results during the construction of the computational code.

The most helpful and adequate method encountered to help verify the veracity of results was a dynamic visualization tool named SAGA, which stands for System Animation for Graphical Analysis [51]. SAGA is a tool which uses *.str* files with information on position and orientation of each body of a system over several steps of time for the display of geometric models created in SolidWorks®, or in an equivalent program. For this purpose, both spherical and tapered roller bearing models were modelled in SolidWorks® using their real geometric properties, presented in Appendix A - Input Data for Bearing Model. The spherical and tapered models created for SAGA are shown in Figure 48 by exploded views of the complete roller bearings.

The program SAGA uses the geometric files to display each body in its respective position and orientation, being also possible to visualize an animation of a simulation when the results are given for more than one time step. The corresponding visualizations with SAGA, for each model, are shown in Figure 49, where it should be noticed that the axial position of each body does not correspond to reality, but is used for better show of each body, and for this purpose only. Also in Figure 49, two rollers are represented with red and blue colours in the spherical bearing and one blue roller in the tapered bearing, which is merely a representation necessary for posterior analysis in Chapter 7.
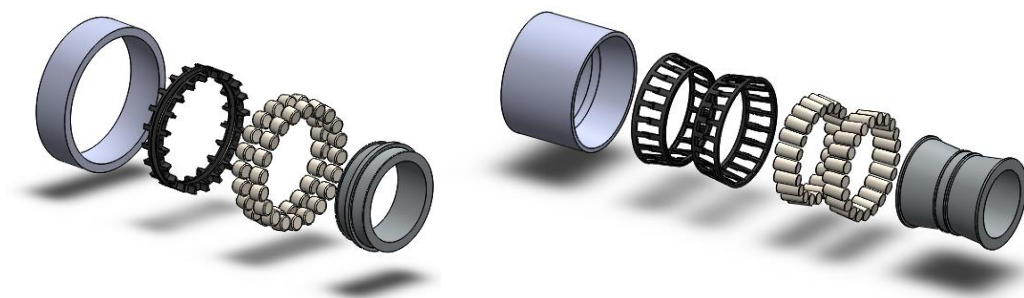
Figure 48: SolidWorks® models of Spherical (left) and Tapered (right) bearings.
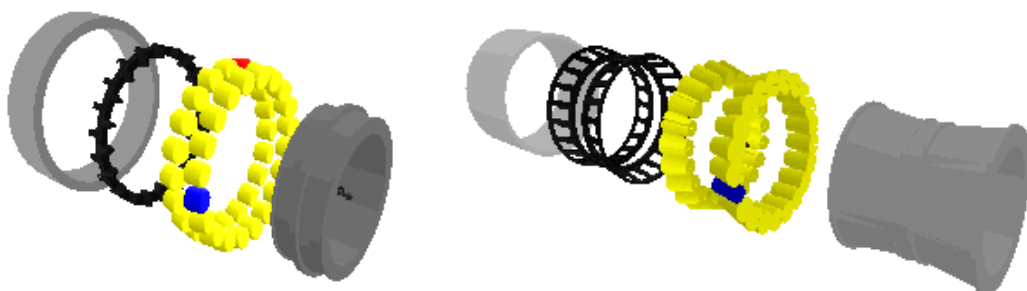
Figure 49: Spherical (left) and Tapered (right) models as visualized with SAGA.

A display example of the tapered bearing model obtained with SAGA at a specific time is shown in Figure 50, with the bodies in their correct position. SAGA is a helpful tool to verify the results qualitatively, since it is possible to see if the bodies shift according to what is expected from reality and if contacts occur at the expected areas where these are detected. With this method, a solid understanding of the bearing behaviour and of the conditions applied to the system is obtained, as well as a good critical capacity to interpret results, identify problems and to make decisions about corrections and modifications.
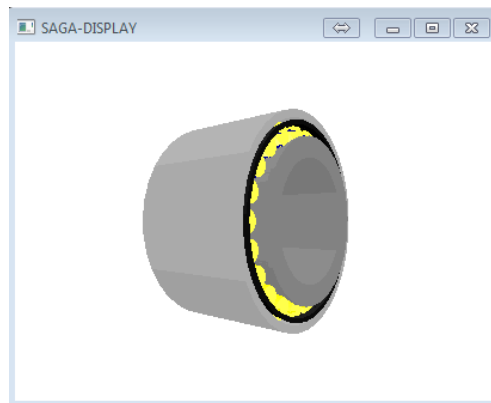
Figure 50: Tapered bearing displayed by SAGA.

Complementary, an approach used to verify the different implementation steps is by interpreting results over different time steps directly with the MATLAB® interface. When constructing the program, the code was regularly ran and evaluated critically step by step, using debugging methods, where it was possible to analyse different values resulting from calculations or numerical methods. These values were studied and compared to expected results, since usually their gross values are possible to predict. The coordinates obtained in the $\mathbf{y}$ vector resulting from each integration step are possible to verify qualitatively for each body, since the initial conditions are known and events such as occurring contacts are detectable, so it is possible, to a certain degree, to predict the trajectory of each body, and thus its location.

7. RESULTS AND DISCUSSION

The `BearDyn` program results from the implementation of the methodology proposed and developed in this work. Although all methods are implemented and it is able to perform a dynamic analysis, its results are not reliable to allow for a realistic evaluation of the roller bearing dynamics. The main obstacle consists in the extremely long time for each analysis resulting from poor computational effectiveness of `BearDyn` and on limited computational resources. Future work must give priority to ensure a reliable performance by `BearDyn` and, consequently, allow developing the remaining tasks for project MAXBE.

Even though program `BearDyn` is not fully functional at this time, it is still possible to obtain results for different cases and with the results to illustrate problems which ultimately help understanding the difficulties. For this purpose the dynamic analysis of a spherical and a tapered bearing are carried here with `BearDyn`, being results discussed.

7.1.   Railway operation scenario and considerations

When running simulations in `BearDyn`, in the real working conditions of a roller bearing, it is important to understand the operating scenario in which it is included. This allows to adjust parameters and understand the program shortcomings. As introduced in Chapter 1, axleboxes are the linking element between the rotating wheelset and the quasi-static frame of the boggie of a railway vehicle. In a railway operation scenario, the primary function of an axlebox is to transfer loads from the inner raceway of the roller bearing, fixed to the wheel shaft, to the outer raceway fixed to the axlebox. The loads acting on a bearing can be calculated if the external forces, such as axleload, weight of the wheelset and payload are known or can be calculated. In the development of this project, information on loads applied on the bearings is not available thus far. However, in a first approximation, the loads from wheel-rail contact, evaluated with a railway dynamics multibody code, can be transported to the inner raceway and allow for the roller bearing loading.

The load resulting from forces external to the roller bearing considered here is caused by the weight of the train car, since other loading cases are not available. Knowing that each carriage is supported mainly by two boggie, which distribute the carriage weight over its components, the resulting load is considered as being applied equally and directly over the axles. The inner raceways of the roller bearings are rigidly fixed to the shaft of the wheelsets, so in this project it is assumed that the proper fraction of load resulting from the weight of the train is applied directly to the center of mass of the roller bearing inner raceway. Considering a common passenger train car, weighing approximately 40 tons, and that each car holds 8 axle bearings, 2 per each axle, a corresponding force of 50 kN is continuously applied downwards in the vertical direction, Z, in the inner raceway of the bearing.

At a later stage of development of the project, it is planned to include in the code the possibility to model and study the dynamic behaviour of the complete boggie, including wheel-rail contact forces. At the present stage, these forces are possible to be introduced as a result of external calculations, being

delivered to the program in the form of an entry table, with information on load value, direction and point of application at different time steps, detailed in Appendix E – BearDyn User Manual. No wheel-rail contact forces were, however, introduced for the simulations shown in this chapter.

Since in railway applications the inner raceway of the roller bearing is fixed to the wheel shaft, while the outer raceway to the axlebox, a constant angular velocity is applied to the inner raceway and the outer raceway is fixed to the inertia frame. As the main purpose of MAXBE project is to monitor roller bearings in actual operating conditions of the railway vehicle, a travel velocity of approximately 50 km/h of a passenger train is considered as the operating condition. As the wheel shaft is part of the wheelset and considering this as a rigid body where the wheel has a mean radius of 0.45 meters, the inner raceway angular velocity is initialized with an angular speed of 30 rad/s.

In `BearDyn`, besides introducing the geometrical features of the models in an entry text file, as well as forces resulting from wheel-rail contact forces, other parameters are required to perform simulations. These include the initial velocities of the inner and outer raceways and the material and lubricant properties. The material properties are given for a regular steel for every component of the bearing, except for the cage, which are for a polyamide. These parameters are presented in Appendix E – BearDyn User Manual, where the structure of each entry file is detailed.

7.2. Simulations with spherical roller bearings

`BearDyn` is prepared to perform a dynamic analysis of either tapered or spherical roller bearings. In this version not all cases of contact are implemented in the case of a spherical roller bearing, particularly contacts with the cage are still missing in the computer code implementation. The only situations for which contact detection is implemented and tested in the program are between raceways and rollers. When simulating the behaviour of a spherical roller bearing while only considering contacts with raceways, it is expected for the rollers to travel in the space between the raceways.

A simulation of 0.05 seconds is performed with the geometry of the spherical bearing presented in Chapter 3.1 and Appendix A - Input Data for Bearing Model with two rows of rollers, using integrator ODE45 to check for the correct contact detection and application of the contact forces. The simulation does not progress any further, since at the end of 0.05 seconds of simulation the rollers are already in contact with each other at the bottom of the bearing which is not only not representative of a realistic situation but can also lead to numerical errors caused by the overlap of contacting points from different rollers. In this simulation, the load of the train is not considered, since some contacts are still not implemented to allow the necessary equilibrium of the system. Two rollers are selected to obtain the dynamic response. Their initial positions in coordinates of the global reference frame are presented in Table 5. The total forces and moments applied over time are presented in Figure 51 for a roller located in the top part of the bearing, referred here to index Body 12. Figure 52 presents the forces and moments applied on a roller located near the bottom of the bearing, which is index Body 25.

Body index	X coordinate (m)	Y coordinate (m)	Z coordinate (m)
12	-0.0125	0.0000	0.0667
25	0.0125	-0.0594	-0.0303

Table 5: Initial positions of bodies 12 and 25 of the spherical bearing
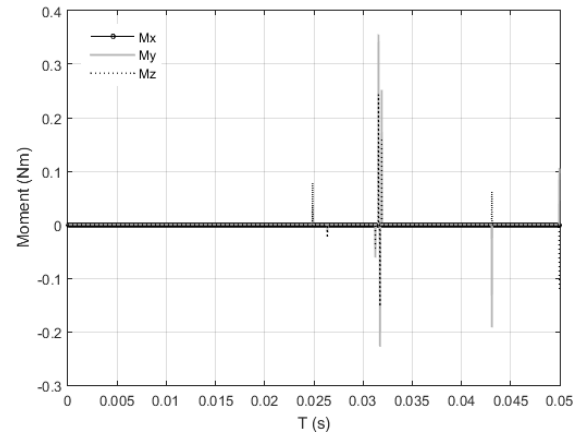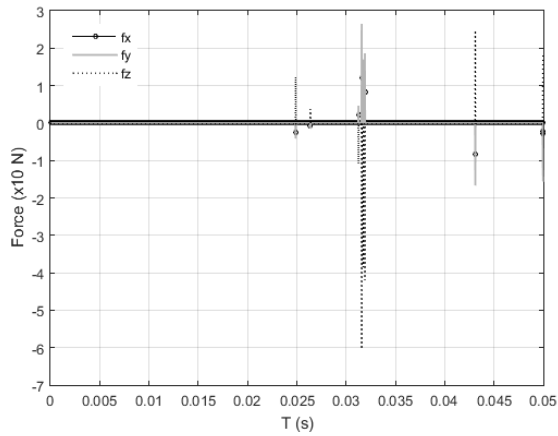
Figure 51: Forces and moments applied on the roller referred to as Body 12 resulting from simulation of a spherical roller bearing.
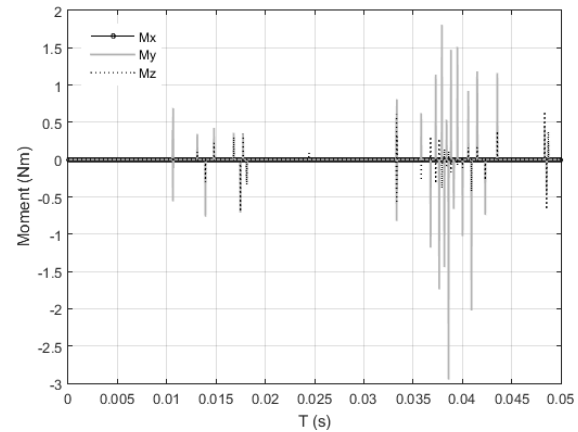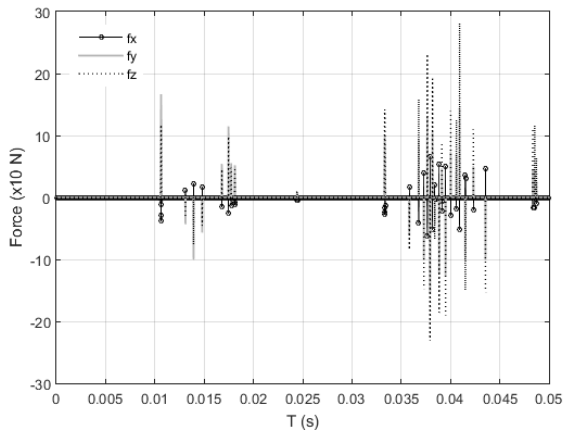
Figure 52: Forces and moments applied on the roller referred to as Body 25 resulting from simulation of a spherical roller bearing.

The contact forces applied on rollers presented in Figure 51 and Figure 52 are not suitable to draw any conclusions regarding the roller bearing dynamics since these are not representative of working conditions of the roller bearing. However, the forces are helpful to understand if contact is being properly detected, which can be positively validated. When running the simulation results with the computer animation program SAGA, it is possible to confirm that the contacts are applied as expected, with the rollers remaining in between the raceways through the whole simulation time. Figure 53 shows three frames from the simulation animation, to help visualize this statement. In this figure, roller identified as Body 12 is shown as a red roller, while Body 25 is identified with the colour blue.
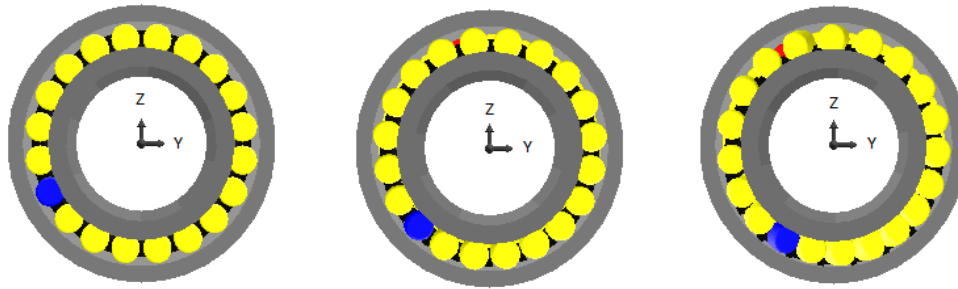
Figure 53: Frames from simulation of a spherical roller bearing with SAGA.

The current limitations of the implemented procedures are: the lack of contact with raceway flanges and with cages. Furthermore, the implementation of the contact models must be further revised to eliminate potential implementation errors.

7.3. Simulations with tapered roller bearings

Tapered roller bearings are modelled in `BearDyn` and all types of contact described in Chapter 4 are implemented and tested. The integration solver ODE45 is used for the dynamic analysis of a two row tapered bearing with the geometry presented in Appendix A - Input Data for Bearing Model.

In order to show some results from each simulation, a roller was selected to extract all interaction forces and kinematic quantities. This roller has the index Body 27 and is located in the lower part of the bearing. Its initial position, using coordinates of the global reference frame, is presented in Table 6 and it is represented as a roller with the colour blue in Figure 54.

Body index	X coordinate (m)	Y coordinate (m)	Z coordinate (m)
27	0.0471	-0.0744	-0.0507

Table 6: Initial position of Body 27 of the tapered bearing
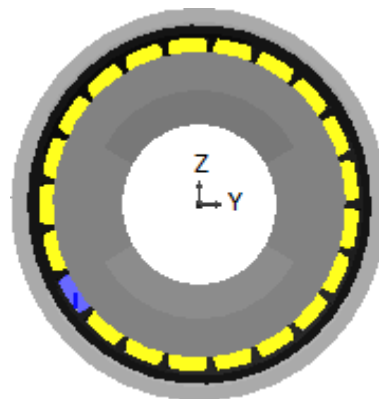
Figure 54: Representation of the tapered bearing with SAGA, with the reference roller shown in blue.

It should be noted that as all rollers have the same geometry, the selected roller is representative of the behaviour of any other roller. In this sense no other roller is single sided in this work.

7.3.1. Analysis of reliability of the contact detection

As a first approach, a simulation of the tapered bearing, without the application of the external load or tangential forces, is shown. This simulation helps to recognize that the full detection of each type of

60

contact is successfully implemented. The analysis is performed for a total integration time of 0.05 seconds, in which the roller progressed about 1/10 of the complete pitch circle, requiring 70 hours of computational time. The position of the reference roller over the time for which the simulation is performed is represented in Figure 55, where the dotted line represents the pitch radius of the bearing, while the full line shows the coordinates of the different locations of the center of the roller during the analysis period.

Figure 55: Trajectory of Body 27 over time of the simulation of a tapered roller bearing with complete contact detection. Line ⋯⋯ refers to the pitch circle while line — refers to the actual roller trajectory.

The total forces and moments acting on the reference roller, Body 27, are shown in Figure 56, where it is possible to observe that punctual forces are mostly applied due to contact in the vertical direction. This statement is sustained by the location of the body in study, since the peak values of force are expected to result from contact with the inner and outer raceways, resulting in forces with larger values than those in the Y and Z directions. The normal contact forces in the X direction result from the raceways and cage angles and from contact with cage tops and flanges.
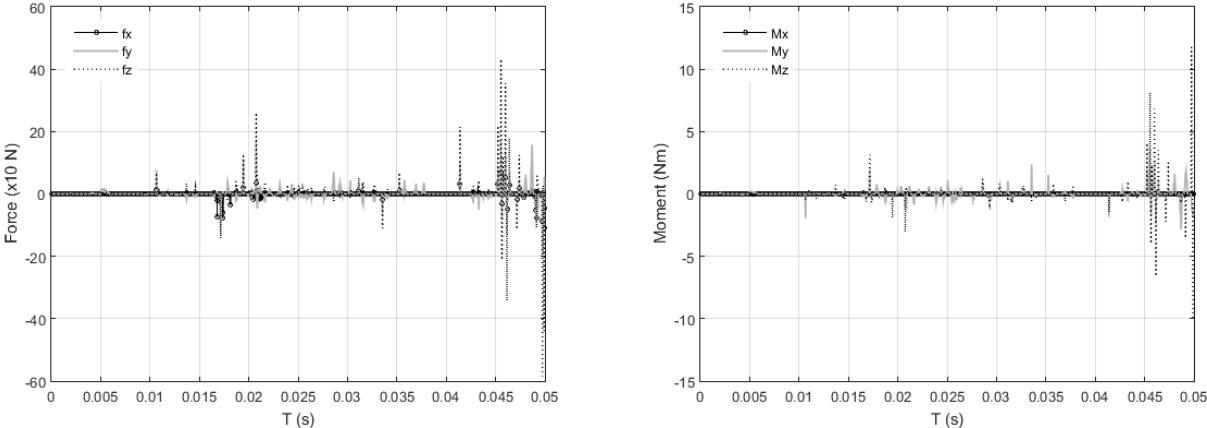
Figure 56: Forces and moments applied on Body 27 resulting from the simulation of a tapered roller bearing with complete contact detection.

The total forces and moments acting on the inner raceway are shown in Figure 57, where it is possible to observe that the action of gravity causes bodies to travel in the negative Z direction, besides

rolling, resulting in a loss of symmetry of the bearing. This effect causes the inner raceway to contact mostly with the rollers located underneath it, resulting in higher magnitudes for the force applied in the Z direction. The response to these forces causes contact with rollers on the opposite side, which justifies the negative values of force applied on the inner raceway in the Z direction.

Figure 57: Forces and moments applied on the inner raceway resulting from the simulation of a tapered roller bearing with complete contact detection.

Still with reference to Figure 57, the fact that there are no relevant moments around the X axis of the inner raceway means that most forces resulting from contact between the rollers and the inner raceway are vectors which intersect the X axis. This is in agreement with the fact that contact between these bodies occurs at a point located with an angle approximately equal to the pitch angle of each roller and in the direction of the raceway surface's normal vector. So, moments caused by contact forces are applied mostly in the Y and Z directions.

7.3.2. Simulation with complete contact detection and train load applied

When testing the application of the load of the train on the inner raceway of the roller bearing model over time, it was perceived that the integration process required extremely high computational resources. This is seen as a consequence of the existence of high frequency contents in the interaction of the contacting bodies, which causes the integration process to reduce the time step and, thus, requiring a much higher number of time steps to obtain successful results. The fact that a variable time step solver is used to perform the integration, results in the need for time steps lower than 10^{-7} seconds, causing the total time necessary to perform the simulation to increase drastically. Here are presented results from a simulation with the tapered bearing while applying the high load on its inner raceway center of mass. The dynamic analysis is performed for 72 hours only to obtain results for a total integration time of 0.014 seconds. Figure 58 shows the resulting trajectory of the center of Body 27 over this period. Figure 59 shows the total forces and moments applied on Body 27 over time, where it is visible that the corresponding magnitude achieves values approximately 100 times higher than those of a case where no external load is applied on the inner raceway, as seen in Figure 56.
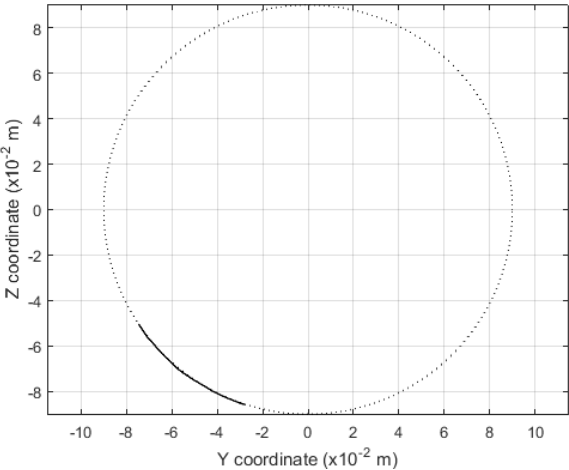
Figure 58: Trajectory of Body 27 over time of the simulation of a tapered roller bearing with complete contact detection and train load applied. Line ⋯⋯ refers to the pitch circle while line — refers to the actual roller trajectory.
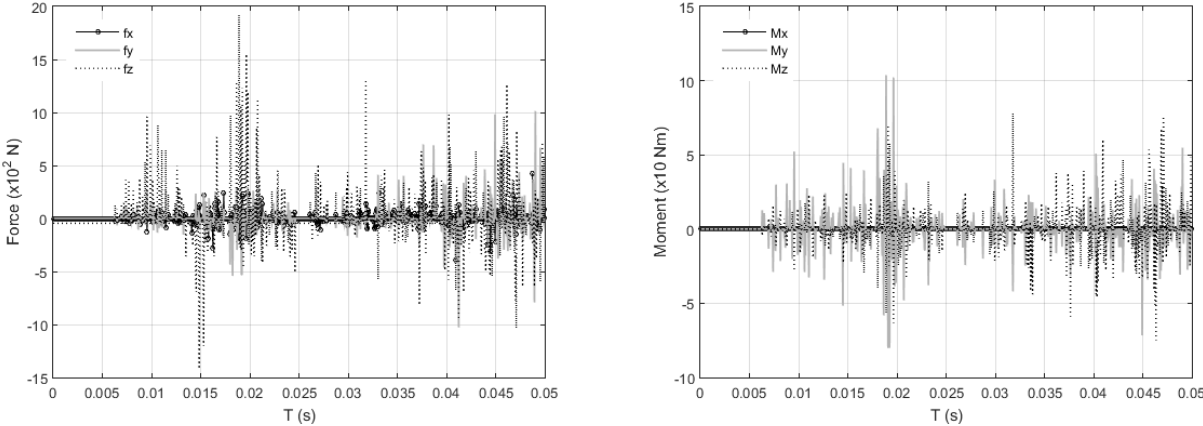

Figure 59: Forces and moments applied on Body 27 resulting from the simulation of a tapered roller bearing with complete contact detection and train load applied.

The problems that appear in the situation presented can be interpreted as resulting from the fact that no energy is dissipated from the system, since no tangential forces are considered.

7.3.3. Simulation with complete contact detection, train load and tangential forces applied

The problems that appear in the previous simulation, in Section 7.3.2, can result from the fact that tangential forces are not considered. Here, a simulation where both train load and tangential forces are applied is performed. In this case, the time steps required by the solver are even smaller and the consequences are visible as the total integration time achieved after 44 hours of computational effort is of merely 4.2×10^{-4} seconds. The trajectory of the center of the roller after this short simulation time is shown in Figure 60, where it is evident that its position does not change much from its initial state.
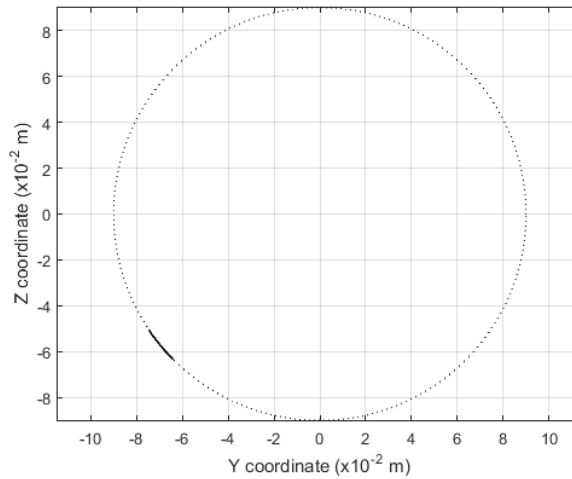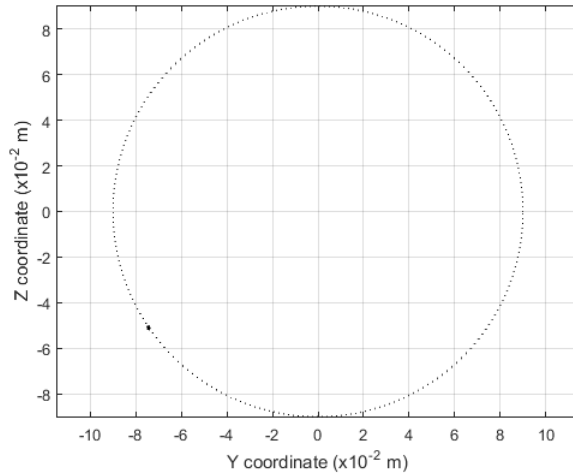
Figure 60: Trajectory of Body 27 over time of the simulation of a tapered roller bearing with complete contact detection, train load applied and tangential forces. Line ⋯⋯ refers to the pitch circle while line — refers to the actual roller trajectory.

The resulting total forces and moments applied on Body 27 and the inner raceway are shown in Figure 61 and Figure 62, respectively. The analysis of these figures does not allow any conclusions to be drawn, due to the short time span of the integration. However, the effect of the increase in the number of time steps calculated by the integrator after a certain period is visible after approximately 2×10^{-4} seconds, where the number of points plotted becomes higher. This difference is justified by the use of a variable time-step solver to perform the integration, which adjusts the steps to be calculated according to the results obtained for different periods of time. It is important to notice that the points plotted in the figures correspond to the results obtained for each successful time step calculated by the solver. The fact that this simulation was not able to be performed successfully, can be caused by the inappropriate use of the solver and its parameters or by a flawed implementation of the contact force models, so the use of a different solver can be the solution.
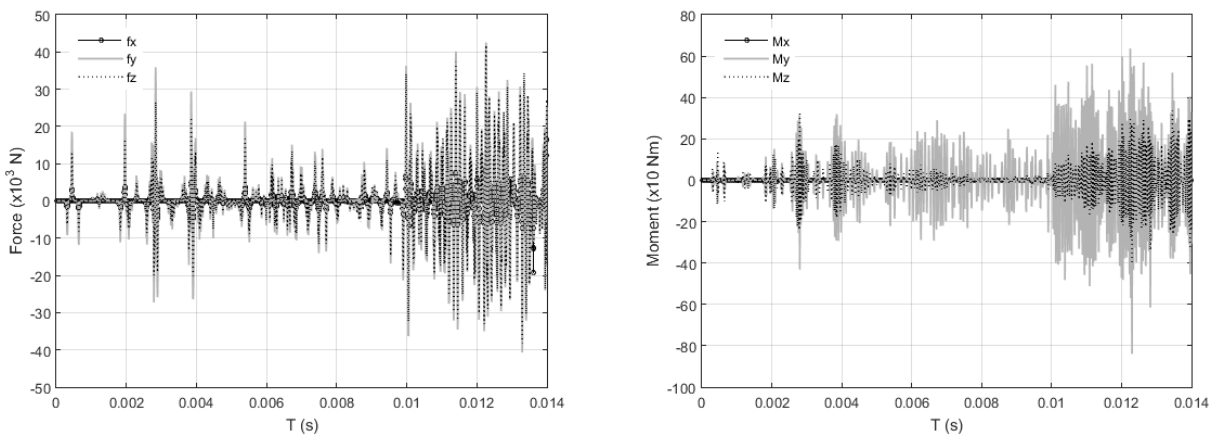

Figure 61: Forces and moments applied on Body 27 resulting from the simulation of a tapered roller bearing with complete contact detection, train load and tangential forces applied.

64

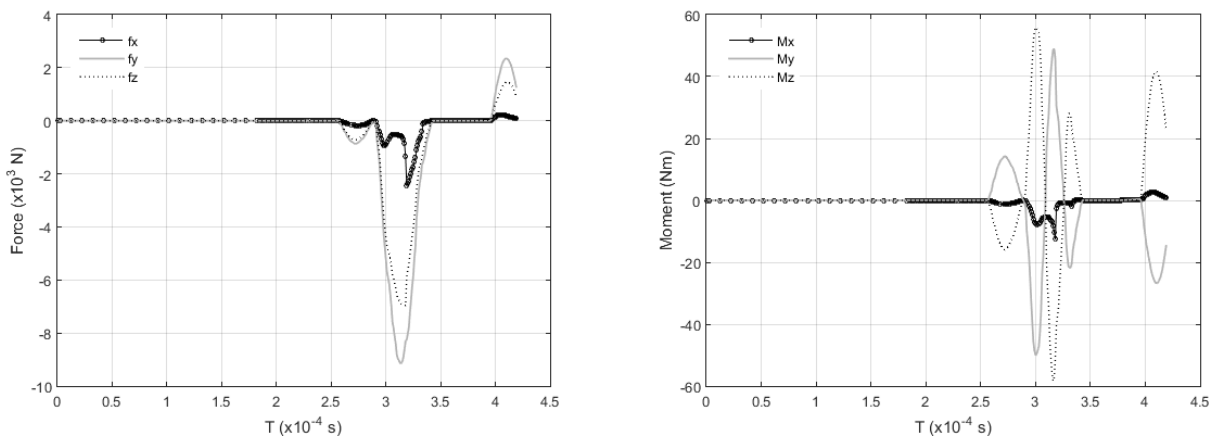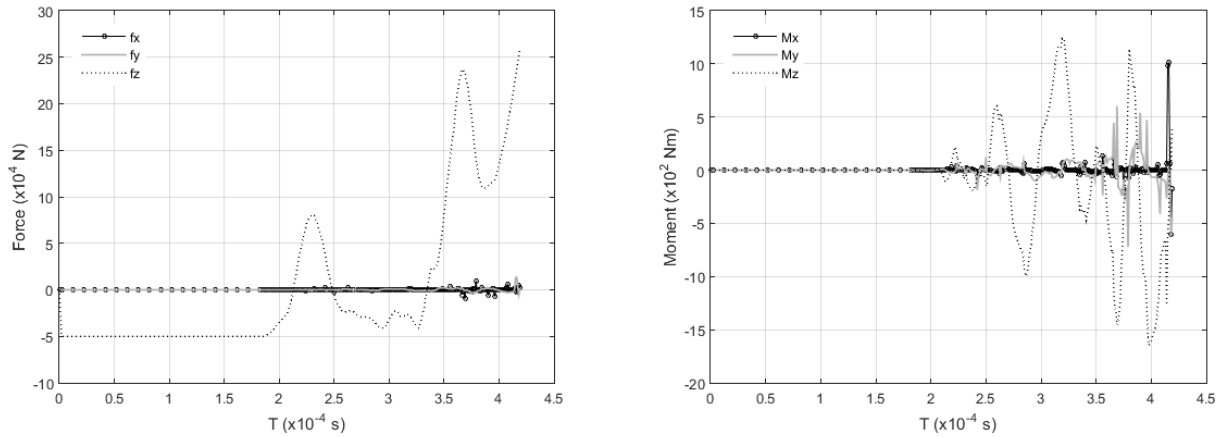Figure 62: Forces and moments applied on the inner raceway resulting from the simulation of a tapered roller bearing with complete contact detection, train load and tangential forces applied.

7.3.4. Possible solutions for errors found

In order to solve the problems found when performing analysis of a tapered bearing in different conditions, some alternatives are studied. As a first approach, the possibility of the problem being stiff is considered. A stiff problem is hard to define precisely; however an ordinary differential equation problem can be defined as stiff if the solution being sought is varying slowly, but there are nearby solutions that vary rapidly, causing the numerical method to take small steps to obtain satisfactory results [52]. From the analysis done to Figure 61 and Figure 62 in Section 7.3.3, it is perceptible that this is a possibility. MATLAB® offers specific integrators to deal with stiff problems, such as ODE15s and ODE23s. In order to test if the problem could be solved more efficiently with a stiff solver, these solvers were tested for the same conditions as ODE45. When running both simulations, the stiff solvers resulted in being much slower than ODE45, with simulation times more than double as ODE45, as supported by Table 7. In this table is presented a comparison of the necessary computational effort for different ordinary differential equation solvers used to perform a simulation in same conditions as the analysis presented in Section 7.3.3, by showing the necessary analysis time, in hours, for each solver to achieve a certain period of time of the integration. ODE15s is a solver used for stiff problems, with low to medium order of accuracy. ODE23s is also a solver for stiff problems, with low accuracy. ODE23t is used to solve moderately stiff problems, with low order of accuracy.

Solver	ODE45	ODE15s	ODE23s	ODE23t
Time consumed (hours)	Integration time (s)	Integration time (s)	Integration time (s)	Integration time (s)
0.5	2.5×10^{-4}	1.8×10^{-4}	1.0×10^{-6}	1.8×10^{-4}
1	3.0×10^{-4}	1.9×10^{-4}	1.6×10^{-6}	1.8×10^{-4}
10	4.0×10^{-4}	3.7×10^{-4}	1.6×10^{-5}	1.8×10^{-4}
24	4.1×10^{-4}	3.9×10^{-4}	2.8×10^{-5}	1.8×10^{-4}
48	4.2×10^{-4}	3.9×10^{-4}	5.9×10^{-5}	1.8×10^{-4}

Table 7: Computational effort compared for 4 different ordinary differential equation solvers, to evaluate the need for a stiff solver.

The cases where extremely small time steps are calculated by the computational solver, could be avoided by fixing a minimum time step to be used. Unfortunately, it is not possible to define a minimum time step for the ordinary differential equation solvers currently available in MATLAB® such as ODE45, since that compromises the purpose of a variable time-step solver. There are only indirect ways to do so, such as changing the tolerance values or the time span for the integration. However, there is no understanding about the direct relation that exists with the minimum time step used, so this approach is ignored. Another solution to avoid undesired time steps in an integration process is to use a fixed time step solver. A solver of this type is implemented, which solves differential equations with a non-adaptive method of order 3, the Bogacki-Shampine Runge-Kutta method [53], which is referred to from this point on as ODE30. With this integrator, a longer dynamic analysis is performed for a tapered bearing with the application of tangential forces and the external loads. Using ODE30, a simulation using the same conditions as in Section 7.3.3 delivered results after 40 minutes, opposed to the 44 hours with ODE45. This simulation was performed for a total integration time of 0.1 seconds, which required 7 days to conclude. The performance time of the simulation is not ideal, since it is not enough for the rollers to complete one revolution around the bearing center and is extremely expensive in computational terms. However, this simulation allows the broadest results possible to be obtained for the conditions enunciated. The analysis that follows shows some different results from this simulation.

Figure 63 shows the trajectory of the roller, Body 27, for 0.1 seconds of simulation. It actually shows that about 1/6 of the complete revolution is concluded. During this period Figure 64 shows the total forces acting in the reference roller.
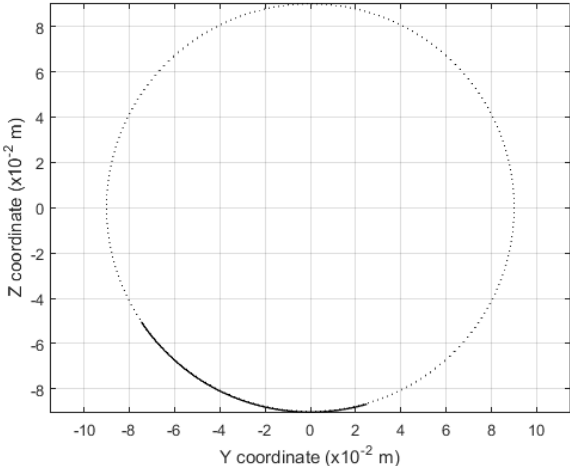
Figure 63: Trajectory of Body 27 over time of the simulation of a tapered roller bearing with complete contact detection, train load and tangential forces applied, using ODE30. Line ⋯⋯ refers to the pitch circle while line — refers to the roller trajectory.

Figure 64: Total forces and moments applied on Body 27 resulting from the simulation of a tapered roller bearing with complete contact detection, train load and tangential forces applied, using ODE30.

It is clear from Figure 64 that the first 0.01 seconds of the analysis correspond to the transient period in which the dynamics of the system has to be disregarded. During this period the system is achieving equilibrium being its response polluted by numeric artefacts.

The total forces and moments that act on the inner raceway over time are represented in Figure 65. In this figure are visible the initial high magnitudes of forces applied in the Z direction, which result from the application of the train load on its center. It is visible that, after approximately 0.01 seconds, these forces do not achieve such high values, which is consistent with the transient period that must be disregarded. The forces applied on the inner raceway after this time are shown in Figure 66, where it can be understood that a near state of equilibrium between the raceway and the rollers is obtained and the total forces are sustained by all bodies. It is important to notice that the forces in the Z direction include the load of the train, i.e., a value of -50kN is added to the Z component of the forces. From observation of both figures it is also visible that the moments resulting from these forces are predominantly applied around the X axis, which is a result of the existence of tangential forces.

Figure 65: Total forces and moments applied on the inner raceway resulting from simulation of a tapered roller bearing with complete contact detection, train load and tangential forces applied, using ODE30.
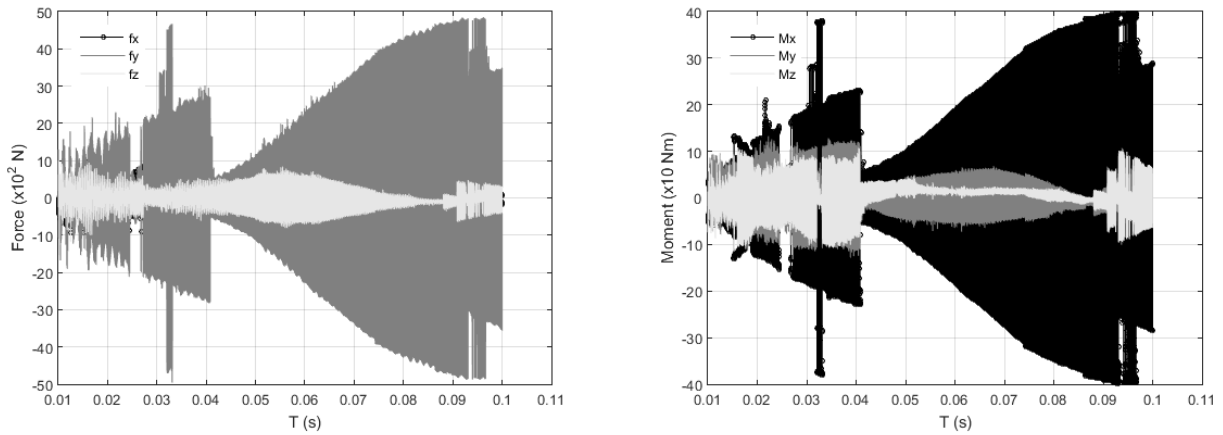
Figure 66: Total forces and moments applied on the inner raceway resulting from simulation of a tapered roller bearing with complete contact detection, train load and tangential forces applied, using ODE30, from t = 0.01s.

Figure 67 shows the total forces acting in the left cage, located in the negative side of the X global axis, while Figure 68 presents the total forces acting upon the right cage, located in the positive side of the X axis. By comparison of both, it is possible to detect a certain symmetricity in the application of forces, which is according to what is expected. It should be noted that the results relative to the first 0.01 seconds of the simulation are ignored and not represented in these figures.
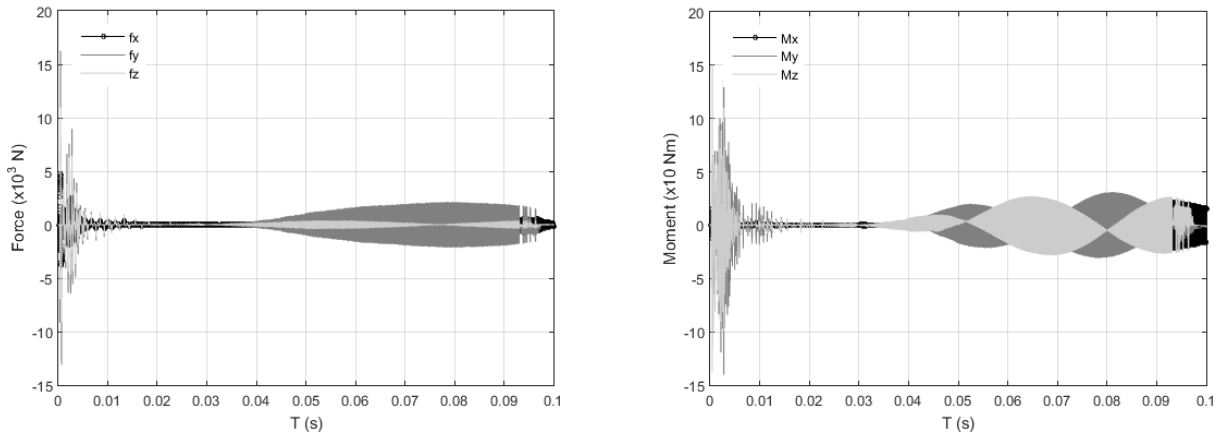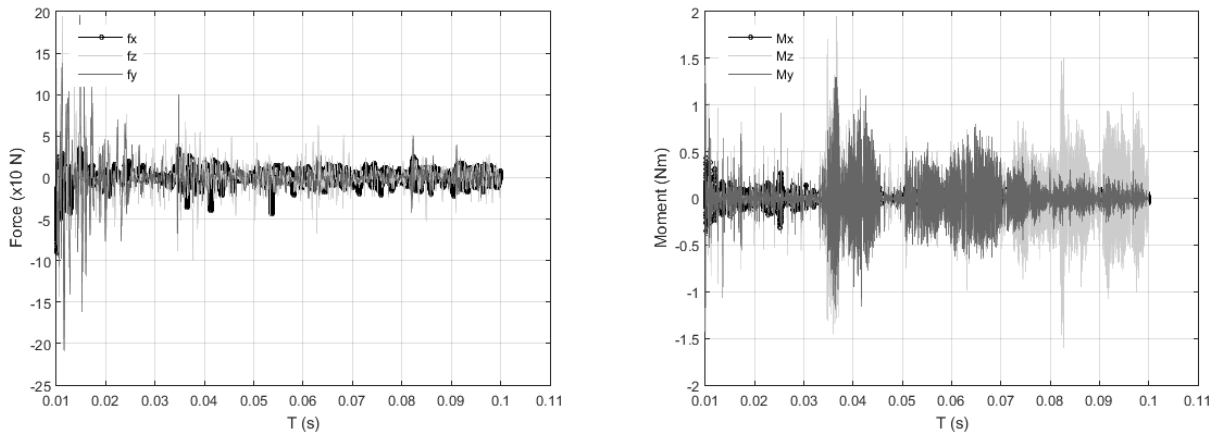

Figure 67: Total forces and moments applied on the left cage resulting from the simulation of a tapered roller bearing with complete contact detection, train load and tangential forces applied, using ODE30, from t = 0.01s.
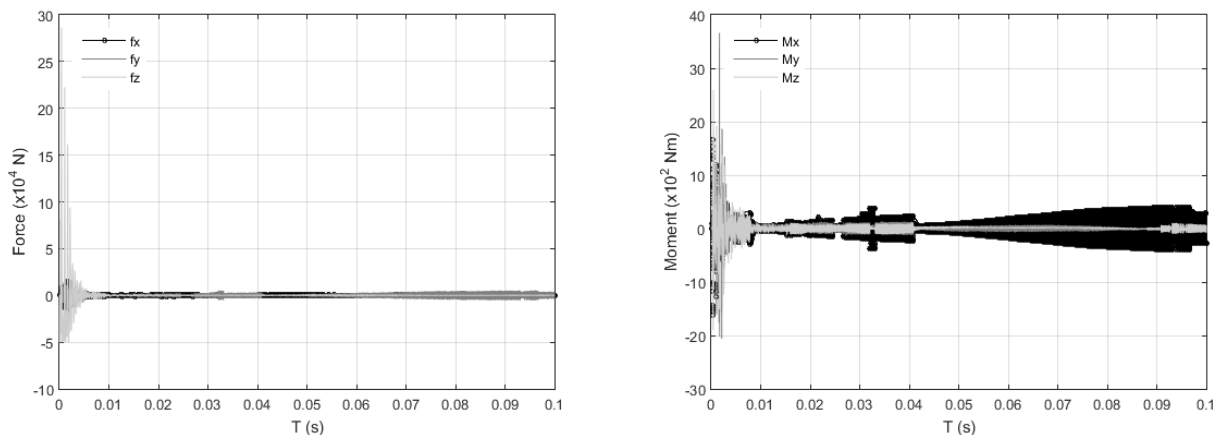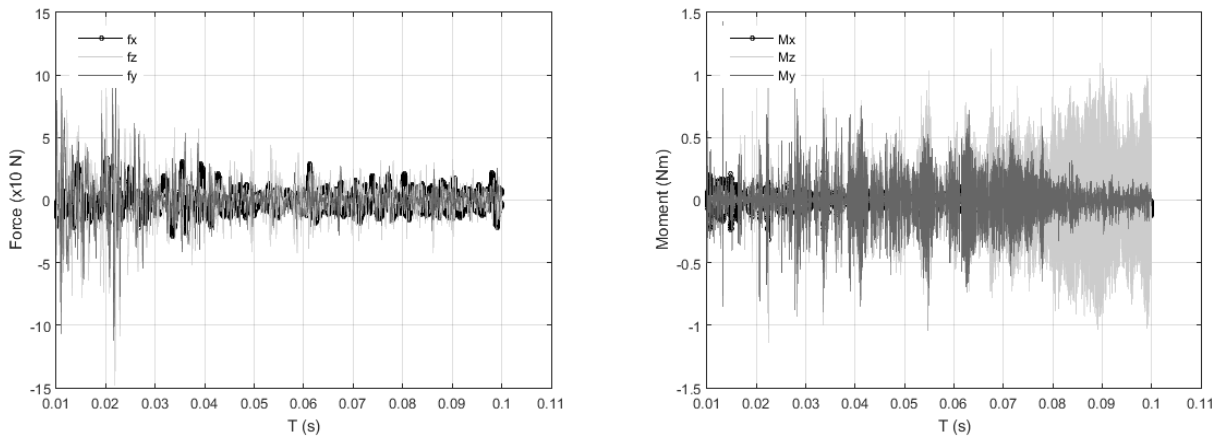

Figure 68: Total forces and moments applied on the right cage resulting from the simulation of a tapered roller bearing with complete contact detection, train load and tangential forces applied, using ODE30, from t = 0.01s.

The trajectory of each cage in the YZ geometric plane can be seen in Figure 69, where the coordinates of their center are shown for each instant in time. When studying these figures, it is possible to see that the cage shifts in the negative Z coordinate due to gravity and suffers some oscillations caused by contact with different rollers. These oscillations are justified by the fact that some clearances exist between the rollers and the cage pockets, being the effect magnified by the approximation of its geometry to lines when contact detection is considered. It is important to notice that these results are obtained for a period of the analysis when the system has not achieved a stable condition, existing several adjustments in the position of the bodies. The results shown are relative to the period after the first 0.01 seconds of the simulation.

(a)   (b)
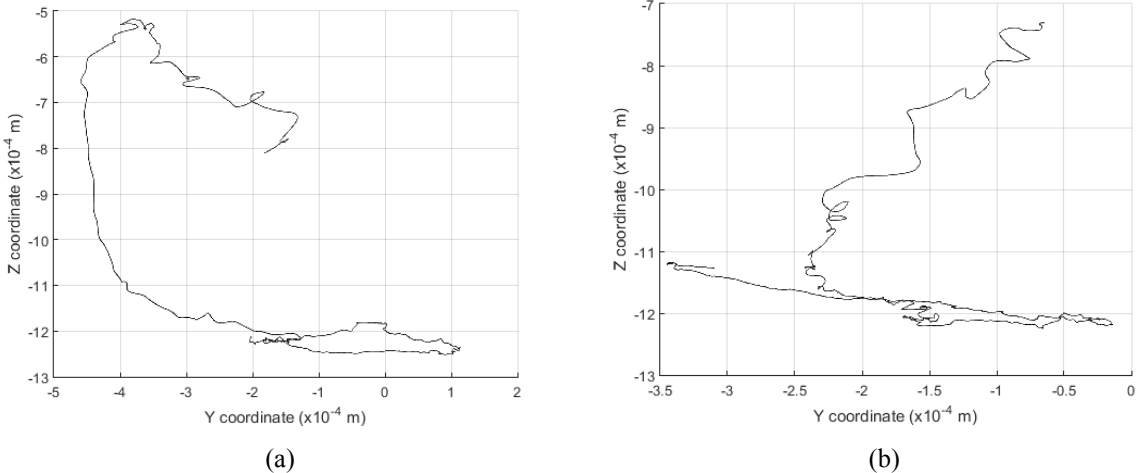
Figure 69: Trajectory of each cage of the tapered bearing resulting from the simulation with complete contact detection, train load and tangential forces applied, using ODE30, from t=0.01s. (a) Trajectory of left cage; (b) Trajectory of right cage.

In order to help the verification of results, the angular velocity of the reference roller is plotted in Figure 70, where the results relative to the first 0.01 seconds of the simulation are ignored and not represented. It is seen that it remains approximately constant after about 0.03 seconds thus showing that the basic dynamic behaviour seems to be obtained.
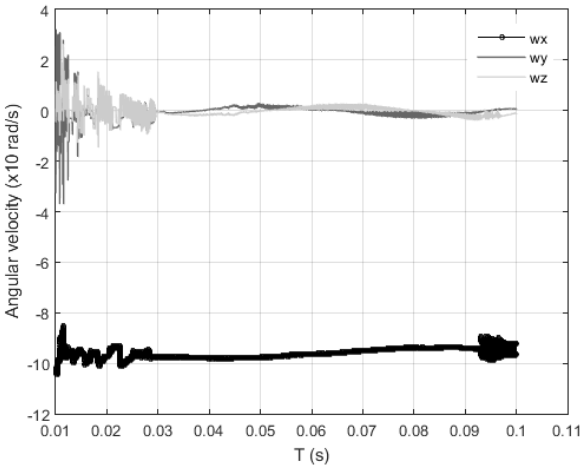
Figure 70: Angular velocity of Body 27 resulting from the simulation of a tapered roller bearing with complete contact detection, train load and tangential forces applied, using ODE30, from t=0.01s.

To obtain the frequency response of the system, the total forces actuating on the inner raceway over time are converted into a function of amplitude and frequency, using a Fast-Fourier Transform algorithm, where the results relative to the first 0.01 seconds of the simulation are ignored. The resulting graphic is presented in Figure 71. Since most frequencies of the results respective to the inner raceway have values below 50 kHz, an approximation to Figure 71 is shown in Figure 72.
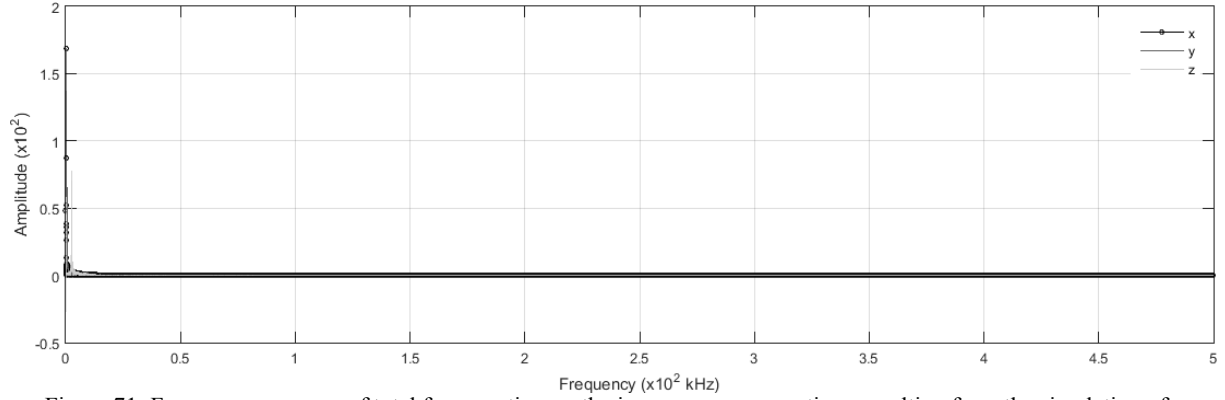
Figure 71: Frequency response of total forces acting on the inner raceway over time, resulting from the simulation of a tapered roller bearing with complete contact detection, train load and tangential forces applied, using ODE30, from t=0.01s.
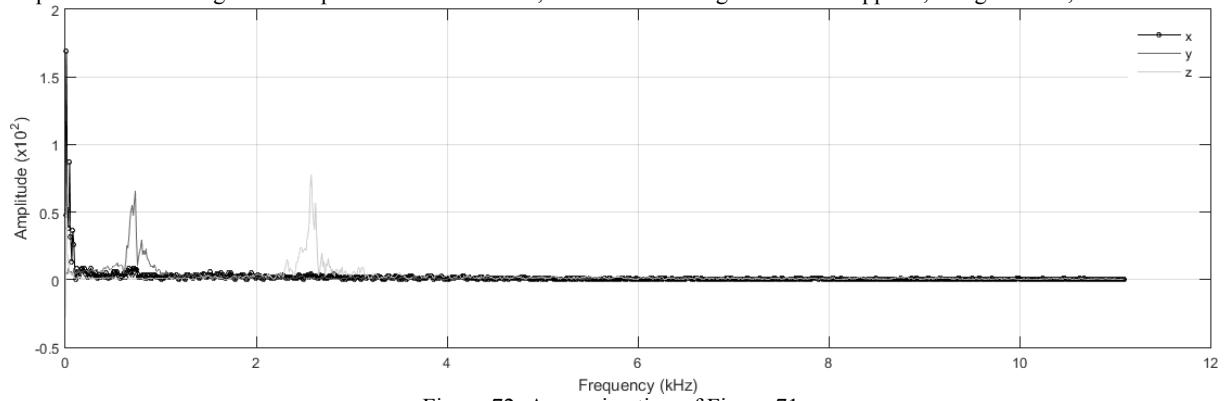
Figure 72: Approximation of Figure 71.

The expected frequencies for the tapered roller bearing studied are calculated according to the procedure reported in references [54] and [55]. The expected working frequencies of the inner raceway, BPFI, are calculated as,

$$\text{BPFI} = \frac{NR}{2} F_S \left(1 + \frac{D_b \cos \alpha_k}{d_m} \right) \tag{7.1}$$

where NR is the number of rollers in the system and F_s the inner raceway rotational frequency. For the conditions considered in the simulation shown in Figure 71, the working frequencies of the inner raceway are expected to have the value 112.96 Hz. According to Li [55], a bearing with no defects can have a response with this frequency value and its harmonics, with a small and even frequency, where no frequency stands out. This does not correspond to the case presented in Figure 71 and Figure 72, since it should be noted that only with the dynamic response obtained for several complete revolutions of the roller bearing are the FFT reliable for the frequency analysis. Due to the computational cost of the current implementation of the methodology, the data obtained is not sufficient for any reliable study.

8. CONCLUSION

The work presented here, part of the international project MAXBE, addresses the development of methods and implementation of an efficient bearing dynamic analysis tool. The computational tool allows the analysis of bearings with different geometries, provided that at this stage, they are either spherical or tapered. The methodologies implemented here solve the problem of defining the basic steps for the general purpose modelling of roller bearings, i.e., first a structure is defined for the data setup of spherical and tapered roller bearings; secondly, the initial position, orientation and velocities of each roller bearing components, i.e., rollers, cages, inner and outer raceways, are defined ensuring kinematic consistency; thirdly the contact of problems for a wide number of geometries are addressed to evaluate the normal and tangential forces caused by contact and lubrication; fourthly, a dynamic analysis procedure is devised and implemented. The formulation of contact between each body is structured as a two way process, the first being the contact detection, based on the kinematics and geometry of each body, while the second consists in the evaluation of the normal and tangential forces developed. In what the contact detection is concerned, the challenge in creating a generalized methodology to create the parametrization of the roller surface lies in the fact that rollers have very specific geometries, which can include crowned regions and corner radius. This is addressed by the use of a slice method, which considers contact between several circles on the roller, allowing these the possibility to have different radius. The development and implementation of contact detection methods revealed to be the most challenging, time-consuming and demanding problem. The contact detection problem requires the solution of a nonlinear system of equations for each potential contact point. It must be noted that the formulation of each one of these systems depends on the types of geometries of the contact pairs. All contact force models are developed and implemented successfully for each contact type. Due to the complex geometry of the cage of the spherical bearing, the necessary models to characterize contact between its rollers and the cage must be developed at a later stage. In any case, contact forces are detected and applied between the raceways and the rollers. All contacts between rollers and the raceways, flanges and cage of the tapered bearing were developed and validated, creating a full description of contact forces acting on each mechanical component of this type of bearing. The necessary models to calculate the tangential forces caused by lubrication have been explored, being the foundations of the methodologies to explore them developed. However, the calculation of the equivalent friction coefficient is not properly validated due to the numerical difficulties in validating the normal contact force models, which provide the background information for the tangent force models.

Based on geometrical measurements performed in real roller bearings with the support of FEUP, realistic bearing models were able to be obtained in order to be tested with `BearDyn`. When performing dynamic simulations of these models with `BearDyn` considering approximate railway conditions, some problems are identified relatively to the necessity of an extremely high computational effort. This difficulty clearly identifies the need for the development of robust and efficient computational

algorithms, eventually based on the use of parallel computation strategies. The second challenge is the identification of integration algorithms suitable to the solution of the type of dynamic problems. Initial alternatives to obtain models for which faster solutions can be obtained were developed in order to revise the computational implementations, such as considering a smaller number of rollers on the bearing or a bearing with a single row of rollers. However, when testing such reduced bearing, in railway operational conditions such as the load of the train, this resulted in a loss of stability of the system and, consequently, in errors during the calculation of contact, due to the insufficient number of rollers to sustain the forces applied. In order to allow results to be obtained with `BearDyn` for a tapered roller bearing in complete working conditions, a constant time-step solver was used to integrate the equations of motion of the system over time. With this solver, the models used in `BearDyn` are able to be verified, even for a short integration span, since the interactions between bodies are perceived as occurring as expected, by using verification methods based on the analysis of the dynamic response and visualization tools. In any case, the length of the time responses obtained are not enough to draw conclusions about the general dynamic performance of the roller bearing models, but are enough to verify the proper functioning of the dynamic analysis tool. With this, the development of the necessary models to perform a dynamic analysis of a roller bearing with a computational tool can be concluded as successfully achieved, serving as a consistent basis for the completion and validation of `BearDyn` with future research and development.

8.1. Future work

While working for project MAXBE, the final goal of creating a computational tool that allows obtaining the full dynamic performance of a spherical or tapered roller bearing in working railway conditions was partially achieved. As described in this work, all theoretical models necessary to conclude the program are available. In order to achieve the final state of the dynamic analysis computational tool, extra time and effort should be spent in its creation. To do so, the `BearDyn` program should be submitted to some more testing and development, as well as code optimization to reduce the computational effort and allow results to be obtained more effectively. Optimizing the code should first focus in computation efficiency, eventually using parallel computational strategies. The other aspect that needs to be explored is the search for numerical methods well adjusted to the type of mechanical system.

The first approach to code optimization should be on code parallelization. By allowing parallel computing, the MATLAB® code runs in parallel in several processors of the computer, which can improve the code performance by allowing executions to run faster. Notice that at each time step, for the type of roller bearings used in railway axleboxes, these are about 1000 contact detection problems to be solved simultaneously, and independently.

Another option that should be considered to improve the code is creating a numerical integrator in its entirety instead of using MATLAB®'s integrator ODE45 or the constant time step solver, called ODE30. By doing so, it is possible to control every aspect of the integrator and optimize its performance to avoid problems similar to those identified in this study related to the integrator.

72

In order to reduce the time spent in contact detection, also more accurate initial values can be calculated and delivered to the search method at each time step. While testing the implementation of contact detection in `BearDyn`, some cases were identified where the closest points were detected in opposite sides of the bearing, due to its symmetric geometry. This problem was solved by using the last correct results when this occurred, but it is not guaranteed to be the best solution. In order to avoid these problems, a more accurate way of predicting the location of two closest points at each time step can be developed. This can be done by, for example, predicting the location of the contact point on each time step by foreseeing the trajectory of each body instead of using the last successful values as initial guesses.

When the code performance is optimized, future developments of the dynamic analysis tool `BearDyn` are necessary in order to reach the main goals intended by project MAXBE. Firstly, the calculation of tangential forces should be reviewed and optimized in order to allow its correct numerical calculation throughout the analysis. When this is approached, it is relevant to know that the specific properties of the lubricant to be used in the case of project MAXBE should be relative to oil Total CARTER EP 220, which is used for lubricating the roller bearings in consideration. The user may have the need to test a model using a different oil. In this case, `BearDyn` has the advantage of allowing the introduction of other properties, as long as properly introduced, according to Appendix E – BearDyn User Manual.

To complete the code, also forces resulting from wheel-rail contact should be correctly introduced into the calculation of force vector, either by resorting to a known timely response and the external forces entry table introduced in Appendix E – BearDyn User Manual; or by full detection and calculation implemented in the dynamic analysis tool code.

When `BearDyn` is functioning properly with these modifications, its code should be adjusted to also allow simulations of spherical roller bearings. Some of the necessary implementations are already present in `BearDyn`'s code, except for the detection and application of contact between its rollers and cages and between its rollers and flanges. The necessary equations for contact detection between these bodies were not developed up until this stage and are also an important development of the code in the future.

When these full modifications are added, `BearDyn` should be prepared to run simulations for enough time to obtain realistic results, for a certain period of time after stabilization of the system. The system needs about 2 or 3 complete revolutions of the rollers around the center of the bearing to allow for its dynamic performance evaluation.

In order to allow the monitoring of the bearings performance in railway operating conditions, as the final goal desired for project MAXBE, the dynamic response of the bearing should be converted to a vibration response using post-processing tools in order to be used as a basis for comparison with the dynamic response of bearings with defects. A final approach requires typical defects on bearings to

be modelled in the code of the dynamic analysis tool. When this is achieved, the main goal of this project is reached, where the collection of vibration response data obtained with `BearDyn` for different bearings with or without defects can be used to infer the health of axle bearings, by comparison with the responses of bearings obtained via wayside or on-board monitoring systems.

REFERENCES

[1] V. B. Bhandari, Introduction to Machine Design, McGraw-Hill, 2001.

[2] T. H. Machado and K. I. Cavalca, "Modeling of hydrodynamic bearing wear in rotor-bearing systems," *Mechanics Research Communications,* vol. 60, pp. 15-23, 2014.

[3] NSK, "NSK Americas," 2008. [Online]. Available: http://www.nskamericas.com/cps/rde/xbcr/na_en/Types_and_Features_of_Rolling_Bearings.pdf. [Accessed 12 September 2015].

[4] Y. Wang, W. Wang, S. Zhang and Z. Zhao, "Investigation of skidding in angular contact ball bearings under high speed," *Tribology International,* vol. 92, pp. 404-417, 2015.

[5] F. Wardle, "Ball bearings," in *Ultra-Precision Bearings*, vol. 2, Woodhead Publishing, 2015, pp. 37-146.

[6] S. Technologies, "Schaeffler," Schaeffler AG, July 2010. [Online]. Available: http://www.schaeffler.com/remotemedien/media/_shared_media/08_media_library/01_publications/scha effler_2/tpi/downloads_8/tpi_158_de_en.pdf. [Accessed 10 September 2015].

[7] "Schaeffler Germany," Schaeffler, 2015. [Online]. Available: http://www.schaeffler.de/content.schaeffler.de/en/branches/industry/railway/products_railway/axlebox_b earings_passenger_wagons_locomotives/axlebox_bearings_passenger_wagons_locomotives.jsp. [Accessed 22 September 2015].

[8] C. Machado, M. Guessasma and E. Bellenger, "Electromechanical modeling by DEM for assessing internal ball bearing loading," *Mechanism and Machine Theory,* vol. 92, pp. 338-355, 2015.

[9] J. S. Zhao, W. Liu, Y. Zhang, Z. J. Feng, J. Ye and Q. B. Niu, "Effects of gyroscopic moment on the damage of a tapered roller bearing," *Mechanism and Machine Theory,* vol. 69, pp. 185-199, 2013.

[10] B. N. Dhameliya and D. K. Dave, "Causes and failure pattern of bearings in railway bogies and their remedies," *International Journal of Application or Innovation in Engineering and Management,* vol. 2, no. 12, pp. 160-163, 2013.

[11] A. Tauqir, I. Salam, A. Haq and A. Khan, "Causes of fatigue failure in the main bearing of an aero-engine," *Engineering Failure Analysis,* vol. 7, pp. 127-144, 2000.

[12] R. Schoen, T. Habetler, F. Kamran and R. Bartheld, "Motor Bearing Damage Detection Using Stator Current Monitoring," *IEEE Transactions on Industry Applications,* vol. 31, no. 6, pp. 1274-1279, 1995.

[13] U. e. a. Zerbst, "Safe life and damage tolerance aspects of railway axles - A review," *Engineering Fracture Mechanics,* vol. 98, pp. 214-271, 2013.

[14] M. Bayraktar, N. Tahrali and R. Guclu, "Reliability and fatigue life evaluation of railway axles," *Journal of Mechanical Science and Technology,* vol. 24 (3), pp. 671-679, 2010.

[15] L. Niu, H. Cao, Z. He and Y. Li, "A systematic study of ball passing frequencies based on dynamic modeling of rolling ball bearings with localized surface defects," *Journal of Sound and Vibration,* vol. 357, pp. 207-232, 2015.

[16] P. W. Tse, Y. H. Peng and R. Yam, "Wavelet Analysis and Envelope Detection for Rolling Element Bearing Fault Diagnosis - Their Effectiveness and Flexibilities," *Journal of Vibration and Acoustics,* vol. 123, pp. 303-310, 2001.

[17] U. A. Patel and S. H. Upadhyay, "Theoretical model to predict the effect of localized defect on dynamic behavior of cylindrical roller bearing at inner race and outer race," *Journal of Multibody Dynamics,* vol. 228(2), pp. 152-171, 2014.

[18] B. Ghalamchi, J. Sopanen and A. Mikkola, "Simple and Versatile Dynamic Model of Spherical Roller Bearing," *International Journal of Rotating Machinery,* pp. 1-13, 2013.

[19] W. Qian, "Dynamic Simulation of Cylindrical Roller Bearings," Von der Fakultät für Maschinenwesen der Rheinisch-Westfälischen, Aachen, 2013.

[20] X. Li-xin, Y. Yu-hu, L. Yong-gang, L. Chong-ning and W. Shi-yu, "Modeling and analysis of planar multibody systems containing deep groove ball bearing with clearance," *Mechanism and Machine Theory,* vol. 56, pp. 69-88, 2012.

[21] H. Aramaki, "Rolling Bearing Analysis Program Package "BRAIN"," *NSK Technical Journal Motion and Control,* vol. 3, pp. 15-24, 1997.

[22] P. Gupta, ADORE Advanced Dynamics of Rolling Elements, Report PKG-TR-C-200-12, Clifton Park, New York: PKG Inc., 2012.

[23] M. Sekiya, "Integrated Bearing Dynamic Analysis System (IBDAS)," *NTN Technical Review,* vol. 79, pp. 119-124, 2011.

[24] A. Siemers and D. Fritzson, "Visualization and data representation for large scale multibody simulations with detailed contact analysis: A case study," *Simulation Modelling Practice and Theory,* vol. 17, pp. 1130-1142, 2009.

[25] T. Sakaguchi and K. Ueno, "Dynamic analysis of cage behavior in a cylindrical roller bearing," *NTN Technical Review,* vol. 71, pp. 8-17, 2004.

[26] T. Sakaguchi and K. Harada, "Dynamic Analysis of a High-Load Capacity Tapered Roller Bearing," *NTN Technical Review,* vol. 73, pp. 20-29, 2005.

[27] H. Hertz, Uber die Beruhrung Fester Elasticher Korper, Journal f.d. reine u. angewandte Mathematik, 1881.

[28] P. Gupta, Advanced Dynamics of Rolling Elements, New York: Springer-Verlag, 1984.

[29] W. Changsen, Analysis of Rolling Elements, London, United Kingdom: Mechanical Engineering Publications Ltd, 1991.

[30] J. Ambrósio, *Deliverable D2.5 - Axle Bearing Modelling and Analysis, Document MAXBE-WP-2.5-IST-01-01,* Instituto Superior Técnico, University of Lisbon, 2014.

[31] P. Nikravesh, Computer-Aided Analysis of Mechanical Systems, Englewood Cliffs, New Jersey: Prentice-Hall, 1988.

[32] P. Nikravesh and I. Chung, Application of Euler parameters to the analysis of three-dimensional constrained mechanical systems, Journal of Mechanical Design, 1982, pp. 104, 785-791.

[33] C. Gear, Simultaneous Numerical Solution of Differential-Algebraic Equations, IEEE Transactions on Circuit Theory.

[34] A. Shabana, Dynamics of Multibody Systems, New York: John Wiley and Sons, 1989.

[35] H. Rahnejat and R. Gohar, "Design of profiled taper roller bearings," *Tribology International,* pp. 269-275, 1979.

[36] SKF, "SKF United States," [Online]. Available: http://www.skf.com/us/products/bearings-units-housings/roller-bearings/tapered-roller-bearings/index.html. [Accessed 3 July 2015].

[37] NSK, "NSK Motion and Control," [Online]. Available: http://www.nsk.com.br/upload/file/NSK_CAT_E1102m_A20-23.pdf. [Accessed 22 September 2015].

[38] K. Harada and T. Sakagushi, "Dynamic analysis of a high-capacity tapered roller bearing," *NTN Technical Review ,* vol. 73, pp. 20-29, 2005.

[39] A. R. Conn, N. I. M. Gould and P. L. Toint, Trust-Region Methods, Society for Industrial and Applied Mathematics, 2000.

[40] J. N. Nocedal and S. J. Wright, Numerical Optimization, Springer Series in Operations Research, Springer Verlag, 2006.

[41] B. Hamrock and D. Dowson, Ball Bearing Lubrication: The Elastohydrodynamics of Elliptical Contacts, New York: John Wiley and Sons, 1981.

[42] T. Harris, Rolling Bearing Analysis, New York: John Wiley and Sons, 2001.

[43] D. Brewe and B. Hamrock, Simplified solution for elliptical-contact deformation between two elastic solids, ASME Trans. J. Lub. Tech., 101 (2), 1977, pp. 231-239.

[44] T. Harris and M. Kotzalas, Essential Concepts of Bearing Technology, Boca Raton, Florida: CRC Press, 2007.

[45] ESDU 78035 Tribology Series, Contact Phenomena: I. stresses, deflections and contact dimensions for normally loaded unlubricated elastic components, London, England: Engineering Sciences Data Unit, 1978.

[46] Roark, W. Young and R. Budynas, Formulas for Stress & Strain, 6th ed., New York: McGraw-Hill, 1989.

[47] E. Radzimovsky, Stress distribution and strength conditions of two rolling cylinders pressed together, University of Illinois Engineering Experiment Station, Bulletin Series No. 408, 1953.

[48] W. Goldsmith, Impact: The Theory and Physical Behaviour of Colliding Solids, London, England: Edward Arnold Ltd, 1960.

[49] C. Pereira, A. Ramalho and J. Ambrósio, "A critical overview of internal and external cylinder contact force models," *Nonlinear Dynamics,* no. 63, pp. 681-697, 2011.

[50] A. Palmgren, Ball and Roller Bearing Engineering, 3rd ed., Burbank, Philadelphia, Pennsylvanya, 1959.

[51] J. Milho and J. Ambrósio, "System Animation for Graphical Analysis - SAGA User's Guide VS 1.0," Institute of Mechanical Engineering, Instituto Superior Técnico, Lisbon, Portugal, 1995.

[52] "Mathworks," [Online]. Available: http://www.mathworks.com/company/newsletters/articles/stiff-differential-equations.html. [Accessed 8 June 2015].

[53] P. Bogacki and L. F. Shampine, "A 3(2) Pair of Runge-Kutta Formulas," *Appl. Math. Lett.,* vol. 2, no. 4, pp. 321-325, 1989.

[54] D. Felten, "Understanding Bearing Vibration Frequencies," *EASA Currents,* pp. 1-3, September 2003.

[55] B. Li, M. Chow, Y. Tipsuwan and C. Hung, "Neural-Network-Based Motor Rolling Bearing Fault Diagnosis," *IEEE Transactions on Industrial Electronics,* vol. 47, no. 5, pp. 1060-1069, October 2000.

[56] P. Gold, A. Schmidt, H. Dicke, J. Loos and C. Assmann, "Viscosity-pressure-temperature behaviour of mineral and synthetic oils," *Journal of Synthetic Lubrication,* vol. 18, no. 1, pp. 51-79, April 2001.

[57] A. D. -. 09, *Standard practice for viscosity-temperature charts for liquid petroleum products (www.astm.org).*

[58] P. Pan and B. Hamrock, "Simple formula for performance parameters used in elastohydrodynamically line contacts," *Trans. ASME, J- Tribology,* vol. 111(2), pp. 246-251, 1989.

[59] J. Archard and E. Cowking, "Elastohydrodynamic lubrication at point contacts," *Proceedings of Symposium on EHL, Institution of Mechanical Engineers,* vol. 180(3B), pp. 47-56, 1965.

[60] H. Cheng, "A refined solution to the thermal-elastohydrodynamic lubrication of rolling and sliding cylinders," *Transactions of ASLE,* vol. 8, pp. 397-410, 1965.

[61] R. Chittenden, D. Dowson, J. Dunn and C. Taylor, "A theoretical analysis of the isothermal elastohydrodynamic lubrication of concentrated contacts I: direction of lubricant entrainment coincident with the major axis of the Hertzian contact ellipse," *Proceedings of the Royal Society, London, England,* vol. A397, pp. 245-269, 1985.

[62] P. Gupta, H. Cheng, D. Zhu, N. Forster and J. Schrand, "Viscoelastic effects in MIL-L-7808-Type lubricant, Part I: analytical formulation," *Tribology Transactions,* vol. 35(2), pp. 269-274, 1992.

[63] W. Wilson and S. Sheu, "Effect on inlet shear heating due to sliding on elastohydrodynamic film thickness," *Trans, ASME, J. of Lubrication Technology,* vol. 105, pp. 187-188, 1983.

[64] P. Wolveridge, K. Baglin and J. Archard, "The starved lubrication of cylinders in line contact," *Proceedings of the Institution of Mechanical Engineers,* vol. 185, pp. 1159-1169, 1970.

[65] I. Kragelskii, Friction and Wear, London, England: Butterworths, 1965.

[66] R. Smith, J. Walowit and J. McGrew, "Elastohydrodynamic traction characteristics of 5P4E polyphenyl ether," *Trans. ASME, J. of Lubrication Technology,* vol. 97, pp. 353-360, 1973.

[67] A. Grubin, "Fundamentals of the Hydrodynamic Theory of Lubrication of Heavily Loaded Cylindrical Surfaces.," *Investigation of the contact Machine Components,* vol. 30, pp. 115-166, 1949.

APPENDIX A - INPUT DATA FOR BEARING MODEL

The present appendix presents the geometric data to be delivered to `BearDyn` by the user, in the format of a text file with a defined number of records. The structure to be followed is described for the necessary data for each type of roller bearing, defined by the properties detailed in the figures.

A.1. General bearing data

			Spherical	Tapered	Units
Bearing.Type		BType	1	2	
Bearing.NumberRollers		BNumbRoller	40	42	
Bearing.OuterDiameter	d_o	BOuterDiameter	0.1700	0.2300	[m]
Bearing.InnerDiameter	d_i	BInnerDiameter	0.0950	0.1300	[m]
Bearing.PitchDiameter	d_m	BPitchDiameter	0.1333	0.1800	[m]
Bearing.Width	L	BWidth	0.0430	0.1600	[m]
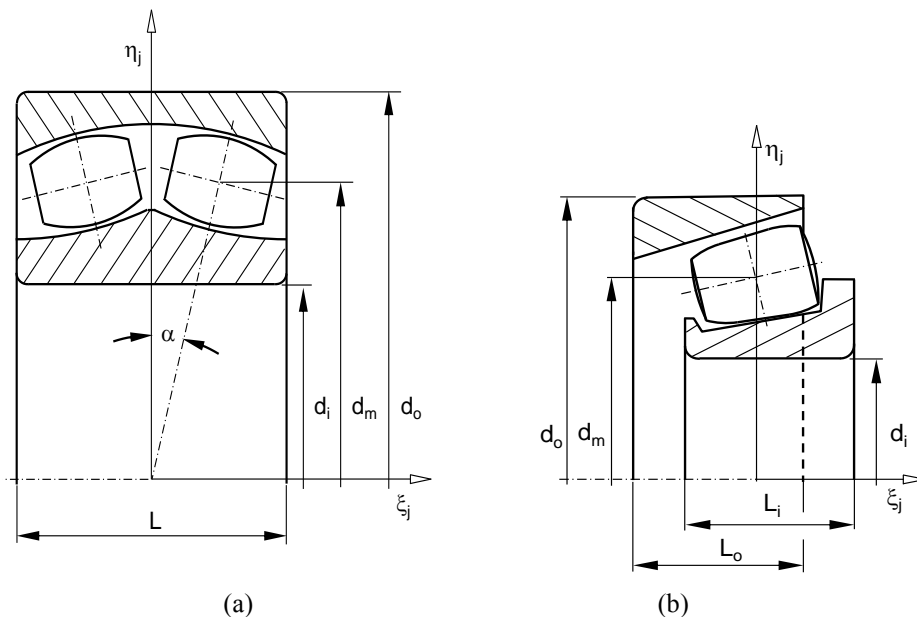
(a)   (b)
Figure 73: Bearing general dimensions: (a) Spherical; (b) Tapered.

Record 1 of the input deck:

Type; NumberRollers; OuterDiameter; InnerDiameter; PitchDiameter; Width

A.2. Spherical bearing geometry, surface and mass data

			Units
Spherical.RollerDiameter	D_d	0.0185	[m]
Spherical.RollerLenght	L_b	0.0155	[m]
Spherical.RollerCrownRadius	R_{cr}	0.0840	[m]
Spherical.RollerCornerRadiusLeft	R_{coL}	0.0014	[m]
Spherical.RollerCornerRadiusRight	R_{coR}	0.0014	[m]
Spherical.InnerRaceRadius	R_{ir}	0.0760	[m]
Spherical.OuterRaceRadius	R_{or}	0.0780	[m]
Spherical.RaceClearance	t_c	0.0005	[m]
Spherical.InnerRaceLenght	L_{il}	0.0430	[m]
Spherical.Tilt	α	0.1852	[m]
Spherical.RollerMass	m_b	0.0311	[kg]
Spherical.RollerInertia	$I_{b\xi\xi}, I_{b\eta\eta}, I_{b\zeta\zeta}$	[1.7000E-7; 1.6000E-7; 1.6000E-7]	[kg m^2]
Spherical.RollerSurfaceRoughness	s_b	0.2100	[μm]
Spherical.InnerRaceMass	m_i	1.1915	[kg]

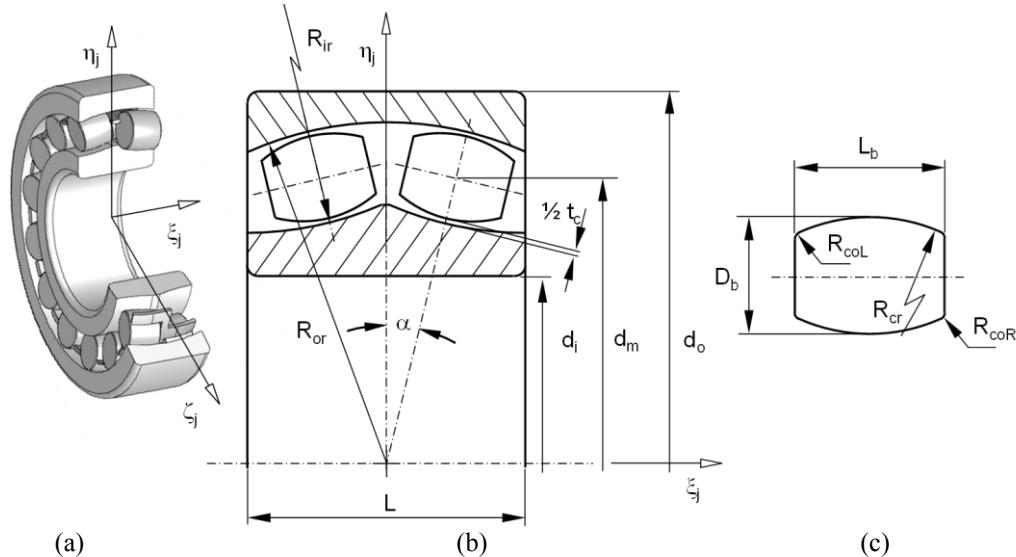|			Units
Spherical.InnerRaceInertia	$I_{i\xi\xi}, I_{i\eta\eta}, I_{i\zeta\zeta}$	[4.5000E-4; 2.5000E-4; 2.5000E-4]	[kg m^2]
Spherical.InnerRaceSurfaceRoughness	s_i	0.3200	[μm]
Spherical.OuterRaceMass	m_o	1.4331	[kg]
Spherical.OuterRaceInertia	$I_{o\xi\xi}, I_{o\eta\eta}, I_{o\zeta\zeta}$	[1.7700E-3; 9.3000E-4; 9.3000E-4]	[kg m^2]
Spherical.OuterRaceSurfaceRoughness	s_o	0.1900	[μm]

Figure 74: Spherical roller bearing: (a) Perspective view; (b) Bearing dimensions; (c) Roller dimensions.

Record 2a of the input deck:

RollerDiameter; RollerLenght; RollerCrownRadius; RollerCornerRadiusLeft; RollerCornerRadiusRight

Record 3a of the input deck:

InnerRaceRadius; OuterRaceRadius; RaceClearance; InnerRaceLenght; Tilt

Record 4a of the input deck:

RollerMass; RollerInertia; RollerSurfaceRoughness; InnerRaceMass; InnerRaceInertia;
InnerRaceSurfaceRoughness; OuterRaceMass; OuterRaceInertia; OuterRaceSurfaceRoughness

A.3. Tapered bearing geometry, surface and mass data

				Units
Tapered.RollerDiameterLargeEnd	D_l	0.0238		[m]
Tapered.RollerDiameterSmallEnd	D_s	0.0222		[m]
Tapered.RollerLenght	L_b	0.0456		[m]
Tapered.RollerLandLenght	L_c	0.0432		[m]
Tapered.RollerCrownRadius	R_{cr}	0.0024		[m]
Tapered.RollerEndRadiusLargeEnd	R_{erR}	1.4200		[m]
Tapered.RollerEndRadiusSmallEnd	R_{erL}	Inf		[m]
Tapered.OuterRaceSemiConeAngle	α_o	0.1541		[rad]
Tapered.InnerRaceSemiConeAngle	α_i	0.1192		[rad]
Tapered.OuterRaceLandLenght	l_o	0.0489		[m]
Tapered.InnerRaceLandLenght	l_i	0.0460		[m]
Tapered.OuterRaceWidth	L_o	0.0670		[m]
Tapered.InnerRaceWidth	L_i	0.0794		[m]
Tapered.InnerRaceLandStart	e_i	0.0112		[m]
Tapered.endplay	e_p	0	If e_p <0, preload is reported here	[m]
Tapered.NumberRows	N_{row}	2	If N$_{Row}$<0, face-to-face mounting	
Tapered.InterRaceSpacing	S_i	0.0179	If the bearing has two rows, S$_i$ is used	[m]
Tapered.RollerMass	m_b	0.1460		[kg]
Tapered.RollerInertia	$I_{b\xi\xi}, I_{b\eta\eta}, I_{b\zeta\zeta}$	[1.2630E-6; 4.0326E-6; 4.0326E-6]		[kg m^2]
Tapered.RollerSurfaceRoughness	s_b	0.0600		[μm]

Tapered.InnerRaceMass	m_i	9.7680	[kg]
Tapered.InnerRaceInertia	$I_{i\xi\xi}, I_{i\eta\eta}, I_{i\zeta\zeta}$	[6.3070E-3; 6.3070E-3; 5.7590E-3]	[kg m^2]
Tapered.InnerRaceSurfaceRoughness	s_i	0.2100	[µm]
Tapered.OuterRaceMass	m_o	10.499	[kg]
Tapered.OuterRaceInertia	$I_{o\xi\xi}, I_{o\eta\eta}, I_{o\zeta\zeta}$	[1.0617E-2; 1.0617E-2; 1.6764E-2]	[kg m^2]
Tapered.OuterRaceSurfaceRoughness	s_o	0.2200	[µm]

(a) (b) (c)
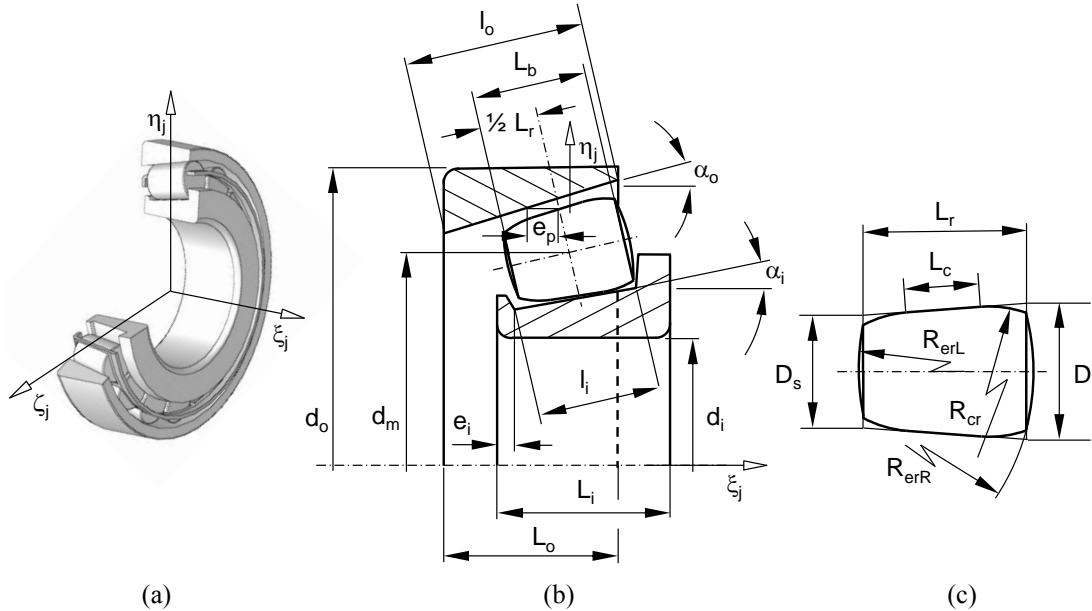
Figure 75: Tapered roller bearing: (a) Perspective view; (b) Bearing dimensions; (c) Roller dimensions.

Record 2b of the input deck:

RollerDiameterLargeEnd; RollerDiameterSmallEnd; RollerLenght; RollerLandLenght; RollerCrownRadius; RollerEndRadiusLargeEnd; RollerEndRadiusSmallEnd

Record 3b of the input deck:

OuterRaceSemiConeAngle; InnerRaceSemiConeAngle; OuterRaceLandLenght; InnerRaceLandLenght; OuterRaceWidth; InnerRaceWidth; InnerRaceLandStart; endplay; NumberRows; InterRaceSpacing

Record 4b of the input deck:

RollerMass; RollerInertia; RollerSurfaceRoughness; InnerRaceMass; InnerRaceInertia; InnerRaceSurfaceRoughness; OuterRaceMass; OuterRaceInertia; OuterRaceSurfaceRoughness

(a) (b) (c)

Figure 76: Tapered roller bearing mounting: (a) Back to back with endplay, $e_P>0$ and $N_{row}=+2$; (b) Back to back, $e_P\leq0$ and $N_{row}=+2$; (c) Face to face, $e_P\leq0$ and $N_{row}=-2$.

A.4. Race flange geometry

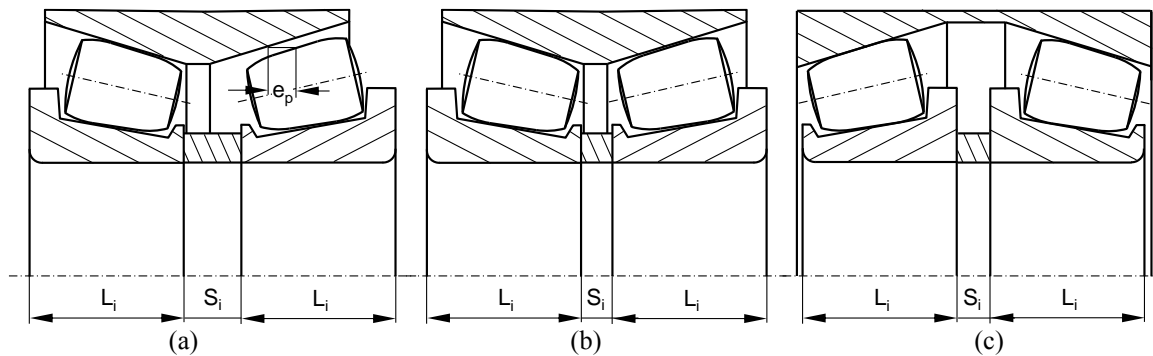|		Spherical	Tapered	Units
Flange.OuterLeftAngle	α_{oL}	Does not apply	Does not apply	[rad]
Flange.OuterRightAngle	α_{oR}	Does not apply	Does not apply	[rad]
Flange.InnerLeftAngle	α_{iL}	0.1705	0.4355	[rad]
Flange.InnerRightAngle	α_{iR}	0.2377	0.1192	[rad]
Flange.OuterLeftHeight	h_{oL}	Does not apply	Does not apply	[m]
Flange.OuterRightHeight	h_{oR}	Does not apply	Does not apply	[m]
Flange.InnerLeftHeight	h_{iL}	0.0040	0.0018	[m]
Flange.InnerRightHeight	h_{iR}	0.0032	0.0074	[m]

(a) (b) (c)
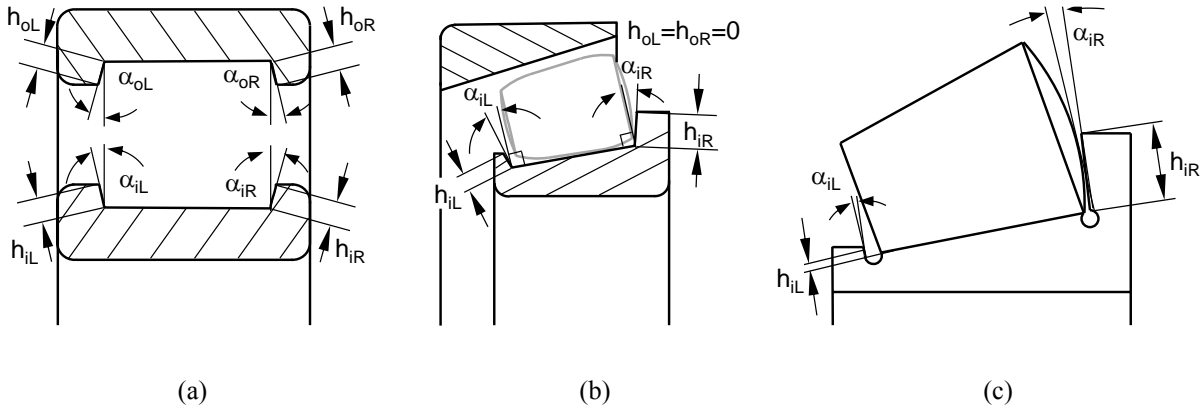
Figure 77: Flanges in roller bearings: (a) Angle and height definitions; (b) Tapered roller bearing; (c) Detail of the flanges in the tapered bearing.

Record 5 of the input deck:

OuterLeftAngle;OuterRightAngle; InnerLeftAngle;InnerRightAngle; OuterLeftHeight;OuterRightHeight; InnerLeftHeight; InnerRightHeight

A.5. Cage geometry, surface and mass data

It is important to notice that some of the data relative to the tapered cage geometry is only available when the bearing is fully mounted. This results in some of the data entries of the following table to not be available, since these were not measured. Also, the cage of the spherical bearing used has a geometry different to the one expected, which is not able to be described with the data predicted in the following table. This way, in future studies where the cage of the spherical bearing is considered, this table should suffer the appropriate modifications.

		Spherical	Tapered	Units
Cage.Guidance	$CGuide$	0	0	
Cage.OuterDiameter	R_{ou}	0.0072	0.0950	[m]
Cage.InnerDiameter	R_{in}	0.0063	0.0860	[m]
Cage.Width	W_l	0.0013	0.0465	[m]
Cage.OuterRaceClearance	C_{ou}	No info. available	No info. available	[m]
Cage.InnerRaceClearance	C_{in}	No info. available	No info. available	[m]
Cage.SemiConeAngle	α_c	No info. available	0.15	[rad]
Cage.GuideLandRadiusRight	R_{gR}	No info. available	0.0991	[m]
Cage.GuideLandWidthRight	W_{gR}	No info. available	0.0086	[m]
Cage.GuideLandPositionRight	L_{gR}	No info. available	No info. available	[m]
Cage.GuideLandClearanceRight	C_{gR}	No info. available	No info. available	[m]
Cage.GuideLandRadiusLeft	R_{gL}	No info. available	0.0860	[m]
Cage.GuideLandWidthLeft	W_{gL}	No info. available	0.0074	[m]
Cage.GuideLandPositionLeft	L_{gL}	No info. available	No info. available	[m]
Cage.GuideLandClearanceLeft	C_{gL}	No info. available	No info. available	[m]

Cage.PocketShape	$PType$	3	2	
Cage.PocketLenght	P_l	No info. available	0.0465	[m]
Cage.PocketWidth	P_w	No info. available	0.0230	[m]
Cage.PocketDimension1	P_1	No info. available	No info. available	[m]
Cage.PocketDimension2	P_2	No info. available	No info. available	[m]
Cage.PocketDimension3	P_3	No info. available	No info. available	[m]
Cage.PocketDimension3	P_4	No info. available	No info. available	[m]
Cage.Mass	m_c	0.1490	0.2000	[kg]
Cage.Inertia	$I_{c\xi\xi}, I_{c\eta\eta}, I_{c\zeta\zeta}$	[4.0700E-5; 8.0500E-5; 4.0700E-5]	[5.2172E-5; 9.4550E-5; 5.2172E-5]	[kg m^2]
Cage.PocketSurfaceRoughness	s_c	0.9000	2.5500	[µm]

Cage guidance:

0	No guidance
1	Outer race guidance
2	Inner race guidance

Cage pocket shape:

1	Cylindrical
2	Rectangular
3	Guided Surface

(a)   (b)
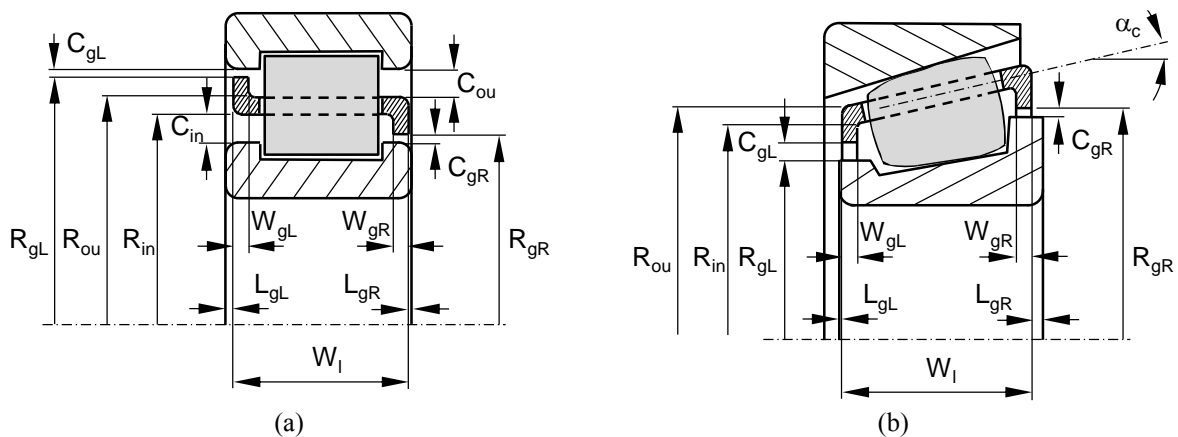
Figure 78: Cage for roller bearings: (a) Cylindrical, with null semicone angle; (b) Tapered. Note that a cage will not have both outer and inner guide lands.

(a)   (b)   (c)
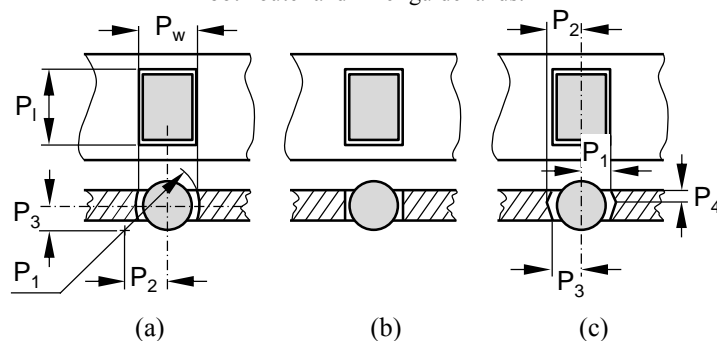
Figure 79: Cage pockets types: (a) Cylindrical; (b) Rectangular; (c) Guided surfaces.

Record 6 of the input deck:

Guidance;OuterDiameter;InnerDiameter;Width;OuterRaceClearance; InnerRaceClearance; SemiConeAngle

Record 7 of the input deck:

GuideLandRadiusRight; GuideLandWidthRight; GuideLandPositionRight; GuideLandClearanceRight; GuideLandRadiusLeft; GuideLandWidthLeft; GuideLandPositionLeft; GuideLandClearanceLeft

Record 8 of the input deck:

PocketLenght; PocketWidth; PocketDimension1; PocketDimension2; PocketDimension3; PocketDimension3

Record 9 of the input deck:

Mass; Inertia; PocketSurfaceRoughness

APPENDIX B – TWO ROW SPHERICAL BEARING INITIALIZATIONS

For spherical roller bearings with two rows, where $\alpha > 0$, the positioning and orientation of the rollers is more intricate than for one row, presented in chapter 3.1. First the position of the rollers in the pitch circle of each row is shifted along X. Second each roller must be rotated about a vector $\mathbf{u}_b$ in order to obtain the orientation shown in Figure 14(a).

<div align="center">(a)   (b)</div>
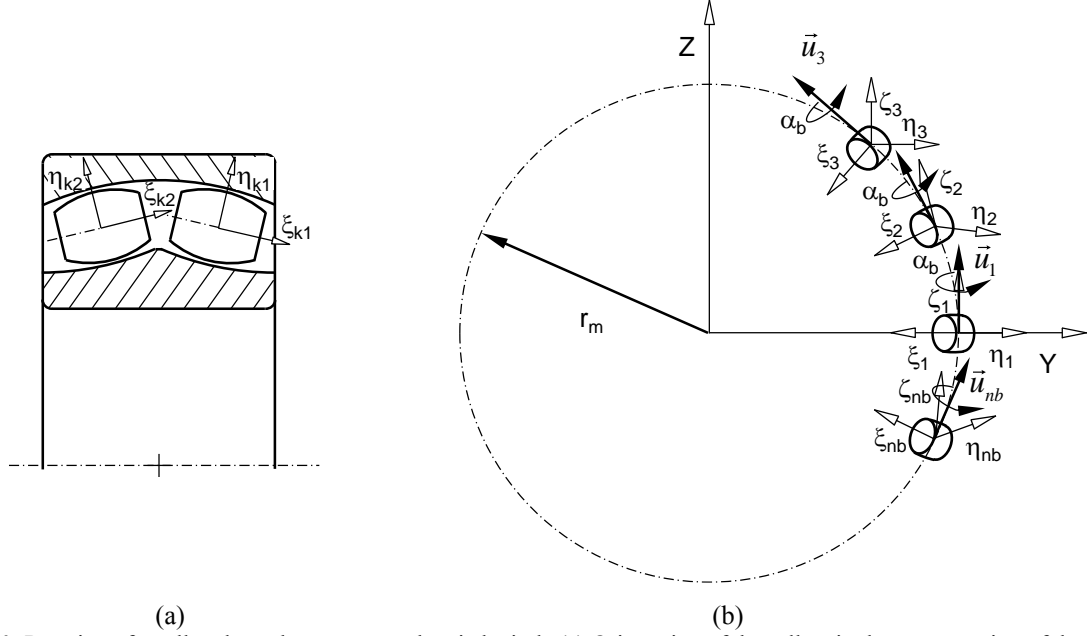
Figure 80: Rotation of a roller about the tangent to the pitch circle (a) Orientation of the rollers in the cross-section of the bearing; (b) Rotation of each roller by α_b about a vector $\mathbf{u}_b$.

The position of the rollers in the pitch circle is similar to that of the single row bearing, only shifted along X. Defining $k=1$ for the row of rollers in the negative side of X and $k=2$ for the rollers in the positive, the rollers position are,

$$\mathbf{r}_b^0 = r_m \begin{Bmatrix} (-1)^k tg\alpha \\ \cos\left[(b-1)\alpha_m\right] \\ \sin\left[(b-1)\alpha_m\right] \end{Bmatrix} \quad b=1,2,...,nb; \ k=1,2 \tag{B.1}$$

The orientation of the rollers in the bearings with two rows correspond to a rotation of each roller, equal to the tilt angle, about a vector tangent to the pitch circle, as depicted in Figure 80(b). Using the definition of the Euler parameters, which are used as rotation coordinates in this formulation, the initial orientation of the rollers in the two rows is,

$$\mathbf{p}_b^0 = \begin{Bmatrix} \cos\dfrac{\alpha}{2} \\ 0 \\ (-1)^k \sin\dfrac{\alpha}{2}\sin\left[(b-1)\alpha_m\right] \\ (-1)^{k+1} \sin\dfrac{\alpha}{2}\cos\left[(b-1)\alpha_m\right] \end{Bmatrix} \quad b=1,2,...,nb; \ k=1,2 \tag{B.2}$$

APPENDIX C – TWO ROW TAPERED BEARING INITIALIZATIONS

For double row tapered roller bearings the initial position and orientation of the raceways is coincident with the inertia frame, i.e.,

$$\mathbf{r}_{inner}^0 = \mathbf{r}_{outer}^0 = \begin{Bmatrix} 0 \\ 0 \\ 0 \end{Bmatrix} \tag{C.1}$$

$$\mathbf{p}_{inner}^0 = \mathbf{p}_{outer}^0 = \begin{Bmatrix} 1 \\ 0 \\ 0 \\ 0 \end{Bmatrix} \tag{C.2}$$

The cages and rollers positions are shifted along X with respect to those used for the single row tapered roller bearing, depending on the size of the spacer and endplay. The orientation of these rolling elements in the double row assemblies are similar to that of the single row bearing, exposed in Section 3.2, but adjusting the sign of the semi-cone angle.

In the back to back mounting, the position and orientation of the cages is,

$$\mathbf{r}_{cage}^0 = \begin{Bmatrix} (-1)^k \tfrac{1}{2}\left(L_i + S_i - e_p - 2x_{in}\right) \\ 0 \\ 0 \end{Bmatrix} \quad k = 1,2 \tag{C.3}$$

$$\mathbf{p}_{cage}^0 = \begin{Bmatrix} \cos\dfrac{k\pi}{2} \\ 0 \\ \sin\dfrac{k\pi}{2} \\ 0 \end{Bmatrix} \quad k = 1,2 \tag{C.4}$$

in which $k=1$ refers to the left side, or negative X cage, while $k=2$ is the right side, or positive X, cage. The position and orientation of the rollers follows the same logic of the cages, being,

$$\mathbf{r}_b^0 = \begin{Bmatrix} (-1)^k \tfrac{1}{2}\left(L_i + S_i - e_p - 2x_{in}\right) \\ r_m \cos\left[(b-1)\alpha_m\right] \\ r_m \sin\left[(b-1)\alpha_m\right] \end{Bmatrix} \quad b = 1,2,\dots,nb \;\; ; \;\; k = 1,2 \tag{C.5}$$

$$\mathbf{p}_b^0 = \begin{Bmatrix} \sin\dfrac{\alpha_k}{2} \\ 0 \\ -\cos\dfrac{\alpha_k}{2}\sin\left[(b-1)\alpha_m\right] \\ \cos\dfrac{\alpha_k}{2}\cos\left[(b-1)\alpha_m\right] \end{Bmatrix} \quad b = 1,3,\dots,nb-1 \;\; ; \;\; k = 1 \tag{C.6}$$

$$\mathbf{p}_b^0 = \left\{ \begin{array}{c} \cos\dfrac{\alpha_k}{2} \\ 0 \\ -\sin\dfrac{\alpha_k}{2}\sin\left[(b-1)\alpha_m\right] \\ \sin\dfrac{\alpha_k}{2}\cos\left[(b-1)\alpha_m\right] \end{array} \right\} \qquad b = 2,4,...,nb \quad ; \quad k = 2 \tag{C.7}$$

In the front to front mounting, the position and orientation of the cages are,

$$\mathbf{r}_{cage}^0 = \left\{ \begin{array}{c} (-1)^k \tfrac{1}{2}\left(L_i + S_i - e_p - 2x_{in}\right) \\ 0 \\ 0 \end{array} \right\} \qquad k = 1,2 \tag{C.8}$$

$$\mathbf{p}_{cage}^0 = \left\{ \begin{array}{c} \cos\dfrac{(k-1)\pi}{2} \\ 0 \\ \sin\dfrac{(k-1)\pi}{2} \\ 0 \end{array} \right\} \qquad k = 1,2 \tag{C.9}$$

in which $k=1$ refers to the left side, or negative X, cage, while $k=2$ is the right side, or positive X, cage, as before. The position and orientation of the rollers follows the same logic of the cages, being defined as,

$$\mathbf{r}_b^0 = \left\{ \begin{array}{c} (-1)^k \tfrac{1}{2}\left(L_i + S_i - e_p - 2x_{in}\right) \\ r_m \cos\left[(b-1)\alpha_m\right] \\ r_m \sin\left[(b-1)\alpha_m\right] \end{array} \right\} \qquad b = 1,2,...,nb \quad ; \quad k = 1,2 \tag{C.10}$$

$$\mathbf{p}_b^0 = \left\{ \begin{array}{c} \cos\dfrac{\alpha_k}{2} \\ 0 \\ -\sin\dfrac{\alpha_k}{2}\sin\left[(b-1)\alpha_m\right] \\ \sin\dfrac{\alpha_k}{2}\cos\left[(b-1)\alpha_m\right] \end{array} \right\} \qquad b = 1,3,...,nb-1 \quad ; \quad k = 1 \tag{C.11}$$

$$\mathbf{p}_b^0 = \left\{ \begin{array}{c} \sin\dfrac{\alpha_k}{2} \\ 0 \\ -\cos\dfrac{\alpha_k}{2}\sin\left[(b-1)\alpha_m\right] \\ \cos\dfrac{\alpha_k}{2}\cos\left[(b-1)\alpha_m\right] \end{array} \right\} \qquad b = 2,4,...,nb \quad ; \quad k = 2 \tag{C.12}$$

APPENDIX D – EQUIVALENT FRICTION COEFFICIENT CALCULATION

D.1. Lubricant film thickness

Being the contacting surface roughness know, either from direct measurement of the rolling elements or by published data, the calculation of the lubricant fluid film thickness plays the central role in the decision on the lubrication mode experienced by the rolling elements. The lubricant film thickness varies along the contact region, being generally of importance its calculation in the center, designated by h_c, or/and close to the exit of the contact region where it is minimum, h_{min}, according to the elastohydrodynamic lubrication theory (EHL). Figure 81 shows the profile of the lubricant film thickness and contact pressure in a general contact.
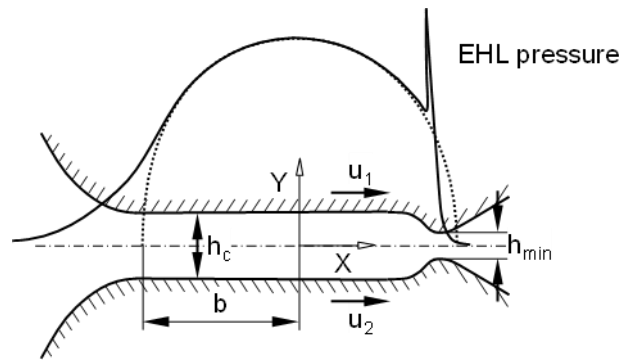
Figure 81: Lubricant film thickness and pressure profiles for a typical rolling contact case.

Depending on the temperature and on the supply of lubricant fluid the lubricant film thickness may vary. Therefore, the computation of the lubricant film thickness is done by,

$$h_c = h_{iso}\,\phi_T\,\phi_S \tag{D.1}$$

where h_{iso} is the isothermal central lubricant fluid thickness for fully flooded lubrication, ϕ_T is the thermal reduction factor and ϕ_S is the starvation factor, that need to be evaluated independently.

D.1.1. Adimensional parameters

Before calculating any of the quantities appearing in Eq. (D.1) let the following dimensionless quantities be defined,

Film Thickness parameter	$H = \dfrac{h_c}{R}$	(D.2)
Speed parameter	$U = \dfrac{\eta_0\,\hat{u}}{E'R}$	(D.3)
Load parameter	$W = \dfrac{q}{E'R}$	(D.4)
Material parameter	$G = \alpha_1 E'$	(D.5)

where the quantities used to define the dimensionless parameters are the effective radius in the rolling direction defined as,

$$R = \frac{r_{ax} r_{bx}}{r_{ax} + r_{bx}} \tag{D.6}$$

the equivalent modulus of elasticity is E' and q is the normal compressive load, for point or elliptic contact, or the normal load per unit of length, for line contact.

The average velocity of the contacting surfaces, depicted in Figure 81, is,

$$u = \frac{1}{2}(u_1 + u_2)$$ (D.7)

where u_1 and u_2 are the velocities of each contacting surface in the rolling plane, given by the projection of the linear velocity of each contacting point on the rolling plane.

The lubricant viscosity at reference temperature T_0 and reference pressure is denoted by η_0 and the viscosity-pressure coefficient α_l provide a rheological description of the lubricant fluid viscosity described by,

$$\eta = \eta_0\, e^{\left[\alpha_1 p - \delta_t (T - T_0)\right]}$$ (D.8)

being p the pressure in operating conditions, T the temperature and δ_t the viscosity temperature index.

The viscosity-pressure coefficient, α_l, can be found from Gold et. Al [56] as,

$$\alpha = s\nu^t$$ (D.9)

where ν is the kinematic viscosity of the oil and s and t are experimental constants which are tabulated for different oils.

The viscosity temperature index can be found by several different ways, being the most common method known as ASTM D341 [57]. This method is based on the knowledge of two characteristic values of temperature and the respective kinematic viscosity for the oil in consideration. Using the relation given by norm ASTM D341,

$$\log\log(\nu + a) = n - m\log(T)$$ (D.10)

a linear regression is formed with $a = 0.7$ and the two given points, in order to obtain the correspondent values of n and m to be used in,

$$\delta_t = \frac{m}{T}\frac{(\nu + a)\ln(\nu + a)}{\nu}$$ (D.11)

where ν is the kinematic viscosity and T is the temperature, in operating conditions.

D.1.2. Isothermal central lubricant fluid thickness

Based on experimental work results, Pan and Hamrock [58] obtained a relation by curve fitting the data to the film thickness measurements obtained from performing a large number of variations on the performance parameters. Pan and Hamrock estimation of the central film thickness for line contact is [58],

$$H_c = 2.022W^{-0.166}U^{0.692}G^{0.470}$$ (D.12)

The isothermal central lubricant film thickness for line contact is given by,

$$h_{iso} = H_c R$$ (D.13)

In the framework of rolling bearing dynamics, point contacts are observed, for instance, in the presence of ball bearings or in contacts of the tapered rollers ends with the raceway flanges or with the cage pocket tops. For point, or elliptical, contact, several expressions have been proposed to describe the lubricant film thickness. For instance, Archard and Cowking [59] suggest that the central lubricant film thickness for point contact is given by,

$$H = 2.04 \left(\chi GU \right)^{0.74} W^{-0.074} \tag{D.14}$$

where χ is the modified factor for side-leakage given as,

$$\chi = \left(1 + \frac{2}{3\alpha_R} \right)^{-1} \tag{D.15}$$

in which $\alpha_R = R_y / R_x$, being R_x simply the equivalent curvature radius calculated using Eq.(D.6) and R_y the equivalent curvature radius in the Y direction, i.e., $R_y = {r_{ay} r_{by}} / {r_{ay} + r_{by}}$, while X the rolling direction and Y the perpendicular direction.

Also Cheng [60] proposes a different expression for the central film thickness parameter as,

$$H = C \left(GU \right)^{n_1} \left(\frac{\sigma_{max}}{E'} \right)^{n_2} \tag{D.16}$$

where the constants C, n_1 and n_2 are constants listed in Table 8 [29] and a, b and σ_{max} are the major and minor semi-axis and the maximum pressure for the case of ellipsoidal, or point, contact in the Hertz elastic contact theory.

a/b	C	n_1	n_2
5	1.625	0.740	-0.220
2	1.560	0.736	-0.209
1	1.415	0.725	-0.174
0.5	1.145	0.688	-0.066

Table 8: Constants for the Cheng expression for the central film thickness parameter [60]

Based on a numerical solution for the elastohydrodynamic lubrication for a point contact, Hamrock and Dowson suggest that the central film thickness parameter for point contact is written as,

$$H = 2.69 U^{0.67} G^{0.53} W^{-0.067} (1 - 0.61 e^{-0.73k}) \tag{D.17}$$

in which $k=a/b$. For convenience, the ratio between the major and minor semi-axis of the contact ellipse may be written as [29],

$$k = \frac{a}{b} = 1.0339 \, \alpha_R^{0.636} \tag{D.18}$$

Under the assumption of the elastohydrodynamic lubrication theory, Chittenden et al. propose that the central lubricant film thickness parameter, for point contact, is evaluated as [61],

$$H_c = 4.31 U^{0.68} G^{0.49} W^{-0.073} (1 - e^{-1.23k^{2/3}}) \tag{D.19}$$

Equation (D.19) is the one used for calculating the central lubricant film thickness parameter in this work, as it shows to be accurate for most of the cases. Certainly, depending on the operation mode

of the roller bearings and on the materials involved, other authors may suggest alternative expressions for the evaluation of this parameter. Regardless of their exact nature, the procedure described here can still be applied, provided that the parameters involved in the Eqs. are properly adjusted.

D.1.3. Thermal reduction factor

The thermal reduction of the film thickness is important at high rolling speeds and/or high slip velocities [62]. Based on the works by Cheng [60] and by Wilson and Sheu [63], Gupta et al. [62] propose a thermal reduction factor for line contact given by,

$$\phi_T = \frac{1 - 13.2 \frac{\sigma_{max}}{E'} L_T^{0.42}}{1 + 0.213 \left(1 + 2.23 \, s^{0.83}\right) L_T^{0.64}}$$

(D.20)

where the thermal loading parameter L_T and the slip ratio s are given by,

$$L_T = \frac{\eta_0 \, \delta_t \, \hat{u}^2}{K_f}$$

(D.21)

$$s = \left| \frac{u_1 - u_2}{\hat{u}} \right|$$

(D.22)

being the average velocity of the contacting surfaces, $\hat{u}$, evaluated by Eq.(D.7), K_f the thermal conductivity, η_0 the lubricant viscosity at reference temperature T_0 and reference pressure and δ_t the viscosity temperature index as used in the rheological Eq. of the lubricant given by Eq.(D.8).

The thermal reduction factor, given by Eq.(D.20), can be used for elliptical contact also if *a/b>5* [28]. However, for non-elongated contact ellipses different expressions for this factor are available in the literature. For elongated contacts, i.e., for a/b>5, the elliptical contact and the line contact share the same thermal factors. For non-elongated contacts Eq.(D.20) can still be used. Although in some recent research work some alternative Eqs. are being proposed for point contact, the expression for line contact is still used for other types of contact as it does not lead to unreasonable errors.

D.1.4. Starvation factor

All the calculations of the lubricant film thickness done before assumed that the supply of fluid is enough to provide a fully flooded contact and the situation is defined as starvation. As indicated in Figure 82, the meniscus of the lubricant film approaches the contact area, ultimately leading to the reduction of the film thickness.

The influence of the starvation on the film thickness has been studied by a large number of researchers, among which Wolveridge et al. [64] propose a starvation factor for line contact as,

$$\phi_S = 1 - e^{\left(-1.68005\Phi^{0.8315} + 0.260137\Phi^{1.558} - 0.016146\Phi^{2.296}\right)}$$

(D.23)

in which,

$$\Phi = \frac{x_0}{b} \left(\frac{b^2}{2h_\infty R} \right)^{\frac{2}{3}}$$

(D.24)

being x_0 the distance from the edge of the Hertzian contact zone to the film meniscus, depicted in Figure 82 or termination, $h_\infty = h_{iso}\phi_T$ the fully flooded film thickness, b the Hertzian contact half-width and R the equivalent radius of contact in the rolling direction, as defined in Eq.(D.6).

For elliptical contact Hamrock and Dowson [41] propose an expression for the starvation factor identified experimentally as,

$$\phi_S = \left[\frac{\tilde{m}-1}{m^*-1} \right]^{0.29} \tag{D.25}$$

in which,

$$m^* = 1 + 3.06 \left[\left(\frac{R}{b} \right)^2 h_\infty \right]^{0.58} \tag{D.26}$$

and $\tilde{m}$ is the adimensionalized distance from the center of the contact zone to the film termination, as represented in Figure 83. Note that all quantities defined in Figure 83(a) are adimensionalized as $\tilde{x}=x/b$, $\tilde{y}=y/a$ and $\tilde{m}=m/b$, leading to the adimensionalized space depicted in Figure 83(b). Note also that $m=x_0+b$, defined in Figure 82.
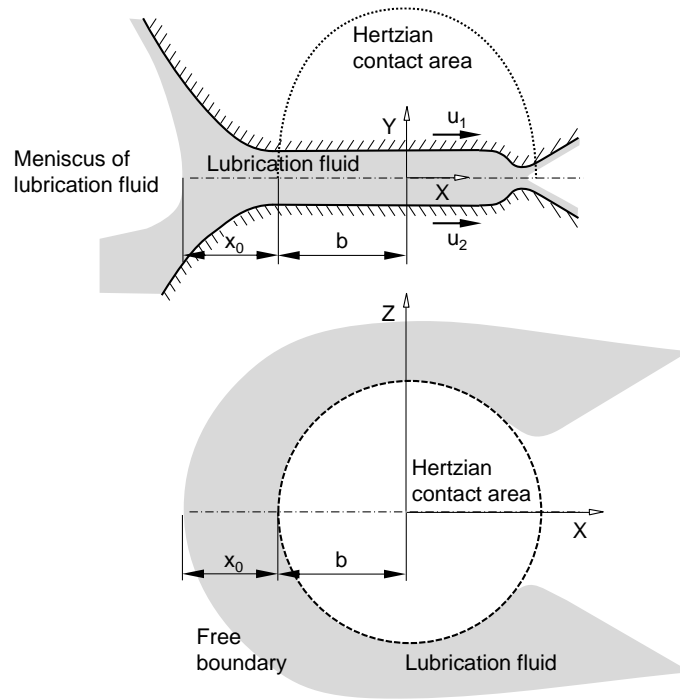

Figure 82: Starved lubrication with the identification of the dimensions required for the definition of the starvation factor.

Note that the starvation factor proposed by Hamrock and Dowson [41], for point contact, and by Wolveridge et al [64], for line contact, are being continuously the focus of new research leading to relations for the starvation factors that better fit specific lubricants. In any case, their computational implementation follow basically the procedures described here.

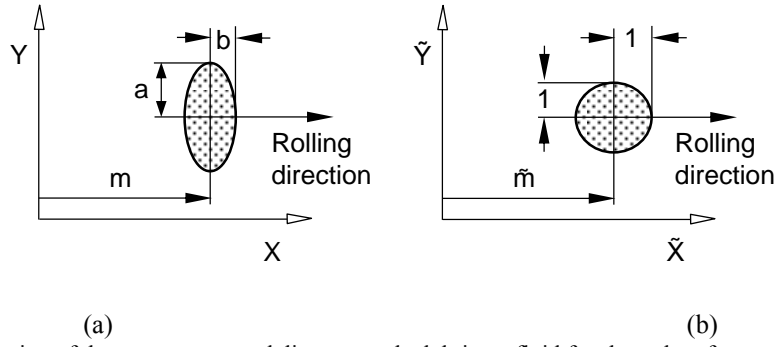(a)   (b)

Figure 83: Representation of the contact area and distance to the lubricant fluid free boundary for starved lubrication of point contact.

The equations described in this topic involve geometries that are difficult to be measured in the context of this work. Also, in the case in study, starvation is not an important aspect to consider since the starvation factor usually results in values of approximately 0.98-1.00 for roller bearings. In this case, the starvation factor is used with a value of 1.00, so the bearings are considered to have full lubricating conditions during operation.

D.2. Equivalent friction coefficients

The evaluation of the tangential forces at contact, using Eq.(5.30), requires the evaluation of the equivalent friction coefficient using Eq.(5.32). In order to evaluate the equivalent friction coefficient for the specific type of contact it is necessary to evaluate the equivalent friction coefficient for boundary lubrication mode, μ_{bd}, if the lubricant film parameter is $\Lambda < \Lambda_{fm}$ and the equivalent friction coefficient for full film mode, μ_{fm}, if the lubricant film parameter is $\Lambda > \Lambda_{bd}$.

D.2.1. Boundary mode equivalent friction coefficient

In the lubrication boundary mode the equivalent friction coefficient, μ_{bd}, relation with the slip ratio is proposed by Kragelskii [65] as,

$$\mu_{bd} = 0.1 - \left(0.1 - 22.28\,s\right)e^{-181.46s} \tag{D.27}$$

Note that for a slip ratio $s=0$ the equivalent friction coefficient is $\mu_{bd}=0$ while for very large slip ratios it tends to $\mu_{bd}\rightarrow 0.1$.

D.2.2. Full film mode equivalent friction coefficient

The evaluation of the full film equivalent friction mode the Muraki formula, reported by Harada and Sakaguchi [38] is used, i.e.,

$$\mu_{fm} = \tau_0 \frac{\overline{S}}{\sigma_{avg}} \tag{D.28}$$

where τ_0 is the lubricant characteristic stress, σ_{avg} is the mean normal stress in the contact area for Hertzian elastic contact and $\overline{s}$ is the mean dimensionless shear stress that needs to be calculated. In order to calculate the mean dimensionless shear stress let the following parameters be defined: the dimensionless shear velocity of the lubricant is,

92

$$\Sigma_{iso} = \frac{\eta_0 \, s \, e^{\alpha_1 \sigma_{avg}}}{\tau_0 \, h_c} \tag{D.29}$$

the Debroah number is,

$$D_{iso} = \frac{\eta_0 \, \hat{u} \, e^{\alpha_1 \sigma_{avg}}}{G b} \tag{D.30}$$

and the dimensionless length of the EHL contact area is,

$$x_c = \frac{D_{iso}}{4\Sigma_{iso}} \sinh^{-1} \Sigma_{iso} \tag{D.31}$$

Finally, the mean dimensionless shear parameter is written as a dependency of the dimensionless length of the EHL contact area as,

$$\overline{S} = \begin{cases} \sinh^{-1} \Sigma_{iso} \left[1 - \left(D_{iso}/4\Sigma_{iso} \right) \sinh^{-1} \Sigma_{iso} \right] & x_c < 2 \\ \Sigma_{iso}/D_{iso} & x_c \geq 2 \end{cases} \tag{D.32}$$

Alternatively, Smith et al. [66], based on measured tractions in an elastohydrodynamic rolling disk test rig, proposed a relation for the traction coefficient, or full film equivalent friction coefficient. Also Gupta [62] based on experimental identification of different lubricant rheological behaviour proposed a traction model that is adopted here.

Consider that the lubricant rheological model relating the viscosity to the pressure and temperature is given by,

$$\mu^* = \mu_0^* e^{\left[\alpha^* p + \beta^* T_0 (1-T) \right]} \tag{D.33}$$

where μ^* is the viscosity and μ_0^*, α^* and β^* are constants to be identified experimentally for the lubricant used. By calculating and integrating the shear stress on the contact area leads to the traction coefficient written as [28],

$$\mu_{fm} = \frac{3}{\alpha^* \sigma_{\max}^2 h \psi} \sqrt{\frac{8 K_f \mu_0^*}{\beta^*}} \left\{ \left[\sinh^{-1} \left(\psi e^{\alpha^* \sigma_{\max}/2} \right) \right]^2 - \frac{2}{\alpha^* \sigma_{\max}} \left[\Phi \left(\psi e^{\alpha^* \sigma_{\max}/2} \right) - \Phi(\psi) \right] \right\} \tag{D.34}$$

where the dimensionless parameter ψ is given by,

$$\psi = s \sqrt{\frac{\mu_0^* \beta^*}{8 K_f}} \tag{D.35}$$

and function $\Phi(\gamma)$ is defined as,

$$\Phi(\gamma) = \int_0^{\gamma} \frac{\left[\sinh^{-1} \psi' \right]^2}{\psi'} \, d\psi' \tag{D.36}$$

In the computer applications the integral in Eq.(D.36) can be tabulated and being that table interpolated during the dynamic analysis.

Gupta found the values for the lubricant rheological constitutive Eq., given in Eq.(D.34) as [28],

$$\mu_0^* = V_1 \, e^{V_2(313-T)} \, e^{V_3(25-u)} \tag{D.37}$$

$$\beta^* = B_1 \left(\frac{T}{313} \right)^{B_2} \left(\frac{u}{25} \right)^{B_3} \tag{D.38}$$

where T is the temperature, in Kelvin, and u is the rolling velocity, in m/s. The values for the constants involved in Eqs.(D.37) and (D.38) are depicted in Table 9.

Lubricant	α^* 1/Pa $\times 10^9$	V_1 Pa s $\times 10$	V_2 1/K $\times 10^2$	V_3 s/m $\times 10^2$	B_1 1/K $\times 10$	B_2	B_3 $\times 10$
MIL-L-23699	5.8015	2.6529	3.6358	1.7054	3.3398	1.3075	-3.9353
MIL-L-27502	5.8015	2.1655	3.9221	0.6441	3.2577	1.0723	-2.7538
MIL-L-7808	5.2214	1.1431	3.3723	2.4079	4.1745	0.6087	-4.7828
Santotrac 30	9.4275	4.0063	5.0459	1.5590	3.4104	1.0930	-2.5647
Mobil DTE	7.2519	2.8407	2.3743	4.5016	2.8939	2.1402	-5.2909

Table 9: Regression coefficients for Gupta Type I traction model [28]

94

APPENDIX E – BEARDYN USER MANUAL

The computational tool `BearDyn` was developed in MATLAB® language, with the use of text files to introduce certain distinct parameters to be used in the calculations. The user should introduce 4 different text files in a folder named "Data" among the MATLAB® files which constitute the program, with the names:

- *Entries.txt*. This file introduces different specific data to be used throughout the integration process. The structure and values used for every simulation presented in Chapter 7 are presented in E.1. *Entries.txt* structure and values, except for the values in the 4th record, since they depended on the simulation performed.

- *Geometry.txt*. The values to introduce in this file are relative to the geometric data of the roller bearing. The structure of this file should follow the structure presented in Appendix A - Input Data for Bearing Model.

- *Lubricant.txt*. In this file should be introduced the rheological characteristic values of the lubricant which are required to calculate the tangential contact forces between the bodies. The structure of this file is shown in E.2. *Lubricant.txt* structure and values.

- *External_Forces.txt*. This file is required to provide information on load value resulting from external wheel-rail contact forces, as well as its direction and point of application at different time steps. The structure to be followed to complete the file is shown in E.3. *External_Forces.txt* structure, where the number of rows of the file can be variable. Since at this point of the project no wheel-rail contact forces are considered, this file is simply used to introduce the load of the train upon the inner raceway. It is important to notice then that the values introduced in Table 12 are the ones used in the project for this purpose. When wheel-rail contact forces are introduced, proper modifications of these values are required.

E.1. *Entries.txt* structure and values

Name	Symbol	Value	Description/Application	Units
winner	ω'^0_{inner}	30	Inner raceway initial angular velocity	[rad/s]
wouter	ω'^0_{outer}	0	Outer raceway initial angular velocity	[rad/s]
Nsl	N_{sl}	6	Number of roller slices	
Young1	E_1	2.0E11	Material 1 Young modulus	[Pa]
Poisson1	ν_1	0.3	Material 1 Poisson ratio	
Young2	E_2	1.4E9	Material 2 Young modulus	[Pa]
Poisson2	ν_2	0.3	Material 2 Poisson ratio	
t0	t_0	0	Starting integration time	[s]
tstep	t_{step}	1E-3	Integration time step	[s]
tend	t_{end}	0.1	Final integration time	[s]
tol	*tol*	1E-5	Tolerance for Newton-Raphson method	
itermax	*itermax*	20	Maximum iterations for Newton-Raphson method	
err	*err*	1E5	Initial error value for Newton-Raphson method	

Table 10: Values in *Entries.txt* file

Structure of *Entries.txt* file:

Record 1 of the input deck:

winner; wouter

Record 2 of the input deck:

Nsl

Record 3 of the input deck:

Young1; Poisson1; Young2; Poisson2

Record 4 of the input deck:

t0; tstep; tend

Record 5 of the input deck:

tol; itermax; err

E.2. *Lubricant.txt* structure and values

Name	Symbol	Value	Description/Application	Units
Lubricant.alpha	$\alpha*$	9.4275E-9		[1/Pa]
Lubricant.V1	V_1	4.0063E-1		[Pa s]
Lubricant.V2	V_2	5.0459E-2	Regression coefficients for Gupta Type I traction model [28]	[1/K]
Lubricant.V3	V_3	1.5590E-2		[s/m]
Lubricant.B1	B_1	3.4104E-1		[1/K]
Lubricant.B2	B_2	1.0930		
Lubricant.B3	B_3	2.5647E-1		
Lubricant.T	T	3.7315E2	Temperature in operating conditions	[K]
Lubricant.T0	$T0$	3.5315E2	Reference temperature	[K]
Lubricant.Kf1	$Kf1$	1.4870	Thermal conductivity of material 1	[W/(m K)]
Lubricant.Kf2	$Kf2$	14870	Thermal conductivity of material 2	[W/(m K)]
Lubricant.P	P	1.0000E9	Pressure in operating conditions	[Pa]
Lubricant.P0	$P0$	2.0000E8	Reference pressure	[Pa]
Lubricant.Visco	ν	44.2300	Viscosity in operating conditions	[cSt]
Lubricant.s	s	0.9904	Experimental constants for Gold et. Al [56] expression	
Lubricant.t	t	0.1390		
Lubricant.Visco1	ν_1	319.2200	2 points of known temperature and kinematic viscosity for the use of norm ASTM D341 [57].	[cSt]
Lubricant.T1	$T1$	313.0000		[K]
Lubricant.Visco2	ν_2	65.2800		[cSt]
Lubricant.T2	$T2$	343.0000		[K]

Table 11: Values in *Lubricant.txt* file

Structure of *Lubricant.txt* file:

Record 1 of the input deck:

Lubricant.alpha; Lubricant.V1; Lubricant.V2; Lubricant.V3; Lubricant.B1; Lubricant.B2; Lubricant.B3

Record 2 of the input deck:

Lubricant.T; Lubricant.T0; Lubricant.Kf1; Lubricant.Kf2

Record 3 of the input deck:

Lubricant.P; Lubricant.P0; Lubricant.Visco; Lubricant.s; Lubricant.t

Record 4 of the input deck:

Lubricant.Visco1; Lubricant.T1; Lubricant.Visco2; Lubricant.T2

E.3. *External_Forces.txt* structure

Time [s]	Force vector applied [N]			Local coordinates of point of application [m]			Inner raceway Euler parameters			
t	fx	fy	fz	ξ	η	ζ	e0	e1	e2	e3
0	0	0	-50000	0	0	0	1	0	0	0
1	0	0	-50000	0	0	0	1	0	0	0
…										

Table 12: Values and structure of *External_Forces.txt* file